

# **Numerical modelling of infragravity waves in coastal regions**

Dirk Pieter Rijnsdorp  
Delft, the Netherlands  
October 2011



*MSc. Thesis Delft University of Technology*

**Title** : Numerical modelling of infragravity waves in coastal regions

**Author** : D.P. Rijnsdorp

**Date** : October 2011

**Graduation committee**

Prof.dr.ir. G.S. Stelling	Delft University of Technology
Dr.Ir. L.H. Holthuijsen	Delft University of Technology
Dr. M. Christou	Shell International Exploration and Production
Prof.Dr. J.D. Pietrzak	Delft University of Technology
Dr.ir. M. Zijlema	Delft University of Technology
Ir. M.A. de Schipper	Delft University of Technology
Prof.dr.ir. A.J.H.M. Reniers	University of Miami (U.S.A.)

This research was carried out at:

Delft University of Technology  
Stevinweg 1  
2628 CN Delft  
The Netherlands

and

Shell International Exploration and Production  
Kessler Park 1  
2288 GS Rijswijk  
The Netherlands



## Abstract

---

Infragravity waves are a common feature in the nearshore wave field and have a significant impact on numerous coastal processes. It is therefore important to accurately predict infragravity wave conditions at a given location. However, analytical relations do not exist with which to make such predictions and one has to rely on numerical models.

In this study infragravity waves are simulated with a linear 1D surf beat model (IDSB) and a non-hydrostatic model (SWASH). The aim of this study is to perform a detailed numerical investigation into the nearshore behaviour of infragravity waves. Specific attention is paid to the generation, propagation and reflection of IG-waves.

The influence of wave conditions and bathymetry on the infragravity wave height is studied. In a number of cases the influence of the bottom slope, significant wave height, peak period, directional spreading and mean incident angle on the predicted wave heights are investigated. The model predictions are found to be qualitatively consistent with both field measurements and theory.

A high resolution flume data set is used to analyse the simulated nearshore infragravity wave behaviour. The propagation and reflection of the infragravity waves is visualised using the cross-correlation function. A signal decomposition technique is used to quantify the magnitude of the incoming and reflected infragravity waves. The results of the cross-correlation function show that both IDSB and SWASH correctly simulate the propagation of the incoming and reflected infragravity waves. The signal decomposition technique shows that in the offshore region (seaward of the surf zone) the IDSB predictions of the incoming and reflected infragravity waves are of a similar magnitude to those measured. In contrast, inside the surf zone IDSB over predicts the incoming and reflected infragravity wave height. This over prediction is associated with an incorrect modelling of the dissipation and/or infragravity wave forcing inside the surf zone. The SWASH results show that the incoming infragravity wave height is under predicted in the offshore region, which is associated with the absence of an incoming bound infragravity wave at the offshore boundary. Additionally the results show that SWASH under predicts the magnitude of the reflected infragravity wave throughout the domain due to the under prediction of the shoreline reflection.

The accuracy of nearshore infragravity wave height predictions by IDSB has been assessed using measurements obtained at the Field Research Facility in Duck, North Carolina (USA). This field data set consists of measurements at several nearshore locations seaward of the surf zone (3m – 14m water depths). Comparison of the predicted and the measured infragravity wave heights at all gauge locations shows an average skill of 0.78, which is in agreement with skill levels found in previous studies.

This study shows that the cross-correlation function and signal decomposition technique are powerful tools to both visualize the propagation of infragravity waves and to quantify their magnitude. By applying both methods a detailed understanding of the infragravity wave properties can easily be derived.

IDSB can be used to obtain estimations of the infragravity wave height outside the surf zone, provided that free IG-waves generated by the release of bound IG-waves dominate and most IG-waves significantly reflect at the shoreline. SWASH is shown to be capable of simulating the nearshore generation and propagation of infragravity waves. However, further development of SWASH is required since the model does not yet include an incoming bound IG-wave at the offshore boundary. Furthermore, additional laboratory experiments are recommended in order to gain more insight into the under prediction of the shoreline reflection.

## **Acknowledgements**

---

This Thesis concludes the Master of Science program at the Faculty of Civil Engineering and Geosciences, Delft University of Technology. This study was conducted over a period of 10 months at the Shell offices in Rijswijk and at the section for Environmental Fluid Mechanics.

First and foremost, I would like to thank the members of my graduation committee for their supervision and feedback during all aspects of the project. Special thanks to Leo Holthuijsen, Marios Christou and Julie Pietrzak for their input and guidance throughout the project.

I want to thank Shell for the opportunity to conduct this study at their premises and I would also like to thank the Metocean team for the great atmosphere during my stay. Furthermore, I thank Ap van Dongeren for providing the code of the signal decomposition method.

Finally, I want to thank my family and friends for their support during the past 10 months.

Delft, October 2011

Dirk Pieter Rijnsdorp



# Contents

---

<b>Abstract</b>	<b>I</b>
<b>Acknowledgements</b>	<b>III</b>
<b>Contents</b>	<b>V</b>
<b>1 Introduction</b>	<b>1</b>
<b>2 Infragravity wave fundamentals</b>	<b>5</b>
2.1 Introduction	5
2.2 Waves	5
2.3 Infragravity waves	6
2.4 Field measurements	10
2.5 Nearshore behaviour	11
<b>3 Methodology</b>	<b>15</b>
3.1 IDSB	15
3.2 SWASH	24
<b>4 Sensitivity study</b>	<b>29</b>
4.1 Introduction	29
4.2 Model setup	31
4.3 Results	32
<b>5 Flume case, Boers</b>	<b>41</b>
5.1 Introduction	41
5.2 Flume setup	41
5.3 Model setup	43
5.4 Results	47
5.5 Further analysis	58
<b>6 Field case, FRF</b>	<b>72</b>
6.1 Introduction	72
6.2 Data description	73
6.3 Model setup	76
6.4 Results	77
<b>7 Conclusions &amp; Recommendations</b>	<b>86</b>
<b>Bibliography</b>	<b>88</b>
<b>List of main symbols</b>	<b>91</b>
<b>Appendices</b>	<b>93</b>
A. Signal decomposition	93
B. Cross-correlation	99
C. Wave envelope	101
D. Sensitivity study – SWASH set up, additional information	103
E. Flume case – Signal decomposition, additional information	109
F. Field case – influence sample length	111



# 1 Introduction

---

Munk (1949) and Tucker (1950) were the first to observe low-frequency motions in coastal regions (*Longuet-Higgins and Stewart, 1962*). These low-frequency surface gravity waves typically have frequencies of 0.005Hz - 0.05Hz and are commonly referred to as infragravity waves (IG-waves). They have a significant impact on a wide variety of coastal processes. *Van Thiel de Vries et al. (2008)* and *Roelvink et al. (2009)* showed the importance of IG-waves with respect to dune erosion during storm conditions. *Bromirski et al. (2010)* found a significant impact of IG-waves on Antarctic ice shelves, they analysed seismic observations and proposed that IG-waves triggered the collapse of the Wilkins ice field in 2008. These IG-waves were generated thousands of kilometres away along the Pacific coast of North America. *Naciri et al. (2004)* showed the importance of incorporating IG-waves in the calculation of moored vessel motions. Furthermore IG-waves may excite harbour seiches, for example, *Chen et al. (2004)*. Subsequently, these seiches can have a big impact on moored vessels motions (*Van Der Molen et al., 2006*).

Munk (1949) and Tucker (1950) linked the generation of IG-waves to the group structure of the incident short waves. This has since been confirmed by many others, for example, *Elgar et al. (1992)*; *Okiihiro et al. (1992)*; *Herbers et al. (1994)*. Two generation mechanisms were identified, nonlinear interactions of the incident short waves and the time-varying breakpoint mechanism. Both mechanisms are associated with the modulation of the wave height on the scale of the wave group. Considering the first mechanism, *Longuet-Higgins and Stewart (1962)* used the concept of radiation stress to show the generation of bound infragravity waves by groups of short waves. These bound waves are phase locked and in anti-phase with the forcing wave groups. An alternative generation mechanism is presented by *Symonds et al. (1982)*, in which the variation of the breakpoint, due to the group structure of the incident short waves, results in the generation of free IG-waves. They showed that this time-varying breakpoint results in the generation of two free IG-wave components, one propagating in the shoreward direction and one propagating in the seaward direction.

After generation the shoreward propagating bound IG-waves reach the surf zone where the short waves start to break. Inside the surf zone these IG-waves persist and subsequently reflect at the shoreline. *Longuet-Higgins and Stewart (1962)* reasoned that bound IG-waves were released inside the surf zone as free IG-waves in the process of short-wave breaking and shoreline reflection. Similar to bound IG-waves, shoreward propagating free IG-waves persist in the surf zone and reflect at the shoreline. After reflection free IG-waves may either propagate towards deeper water or remain confined to the nearshore by refraction. Free IG-waves that reach deep water are known as leaky waves and free IG-waves trapped inside the nearshore are known as edge waves.

Bound IG-waves are locally forced by the incident short waves and their magnitude mainly depends on local conditions. In contrast, free IG-waves depend on the global surroundings. The shelf topography influences the propagation and the trapping of free IG-waves, while the shoreline morphology (e.g. rocky coasts or sandy beaches) affects the reflection of IG-waves (*Herbers et al., 1995b*). Numerous field measurements showed that the nearshore IG-wave field was a mixture of bound and free IG-waves, for example, *Oltman-Shay and Guza (1987); Elgar et al. (1992); Okihiro et al. (1992); Herbers et al. (1994, 1995b)*.

The accurate prediction of the IG-wave height in a coastal region therefore requires a proper description of the generation and nearshore transformation of the IG-waves. No analytical relations exist with which to make such predictions and one has to rely on numerical models. Three types of numerical models are available that are capable of simulating IG-waves: Surf beat models; Boussinesq models and non-hydrostatic models. Surf beat models compute IG-waves by combining a wave driver model, which provides the forcing at the scale of the wave groups, and a shallow water model that accounts for the generation and nearshore transformation of the IG-waves. Boussinesq and non-hydrostatic models are phase resolving and account for all relevant nearshore processes (e.g. shoaling, refraction, reflection and triad interactions) and therefore provide a potentially accurate but computationally expensive approach. Surf-beat models have been widely used to simulate IG-waves in coastal regions and studies by *Madsen et al. (1997)* for example, showed the capabilities of Boussinesq models in simulating IG-waves, In contrast, non-hydrostatic models have not been used to model this phenomenon.

In this study IG-waves are simulated in a coastal region with a linear 1D surf beat model (IDSB) and a non-hydrostatic model (SWASH). IDSB (*Reniers et al., 2002*) estimates the IG-wave response of directionally spread short waves incident on an uniform alongshore coast. IDSB does not include the time-varying breakpoint mechanism; it only considers the generation of free IG-waves due to the release of bound IG-waves inside the surf zone. The IG-wave response is estimated using linear shallow water equations that include the effect of bottom friction, rollers and the set-up of the mean water level. SWASH has recently been developed at Delft University of Technology (*Zijlema et al., 2011*) and is intended to be used for simulating the transformation of surface gravity waves and shallow water flows in coastal regions. In theory SWASH is capable of simulating all nearshore processes relevant for IG-waves.

Previous studies have shown that IDSB is capable of predicting the IG-wave height in a coastal region (*Reniers et al., 2002, 2010, Bijl et al., 2009*). In contrast to IDSB, SWASH has not been validated for IG-waves. Nevertheless, it has been shown that SWASH is capable of simulating the nearshore processes relevant for IG-waves (*Zijlema et al., 2011*). Therefore, SWASH is in theory capable of correctly simulating IG-waves.

The aim of this study is to perform a detailed investigation in the nearshore behaviour of IG-waves, simulated by IDSB and SWASH. Specific attention is paid to the generation, propagation and reflection of IG-waves.

First the governing processes relevant for the nearshore behaviour of IG-waves are described in Chapter 2. This provides the background physics needed for the later interpretation of the model results. In order to assess the capabilities and limitations of the numerical models, a thorough understanding of the governing equations is required. A detailed description of IDSB and SWASH is therefore given in Chapter 3.

The sensitivity of the models to varying wave conditions and changing bathymetry is assessed in Chapter 4. This provides insight into the influence of a specific physical parameter (e.g. the bottom slope) on the predicted IG-wave height. Together with the knowledge from Chapters 2 and 3 a qualitative assessment of the model results is presented here.

Two data sets are available with which to assess the predictive capabilities of both models. First the laboratory data set of *Boers (1996)* is used for a detailed assessment of the model results. In this flume experiment irregular waves propagating over a barred beach were simulated. This data set allows for a detailed quantitative analysis of the nearshore IG-wave behaviour simulated by IDSB and SWASH (Chapter 5). The new application of the cross-correlation technique for model analysis allowed visualization of the propagation and reflection of the IG-waves. A signal decomposition technique is used to quantify the magnitude of the incoming and outgoing IG-waves.

The second data set concerns field measurements obtained at the Field Research Facility in Duck, North Carolina, USA. Wave measurements were obtained by several gauges located at intermediate water depths (ranging 3m - 14m). The aim of Chapter 6 is to examine the accuracy of the predicted significant wave height at all available gauge locations. Due to time constraints only IDSB is assessed.

In Chapter 7 the results are summarised and some recommendations for further studies are presented.



## 2 Infragravity wave fundamentals

### 2.1 Introduction

This study focuses on the description of infragravity (IG) waves<sup>1</sup> in coastal regions. Coastal waters are complex regions influenced by various hydrodynamic and morphological processes. Knowledge of the processes relevant for IG-waves is essential for the correct understanding of the phenomenon. The aim of this Chapter is to provide insight in the processes relevant for IG-waves.

### 2.2 Waves

Various types of surface gravity waves can be distinguished in oceans and coastal waters. Sorting the various waves by their frequencies gives an overview of the various wave types that can be encountered in oceanic and coastal waters (Figure 2.1). The wave period can vary from seconds (capillary waves) up to 24 hours (trans-tidal waves). In this study the focus is on the description of the IG-waves in coastal waters and therefore only the motions at relative high frequencies are of interest: the short waves (swell and wind waves) and the phenomena itself.

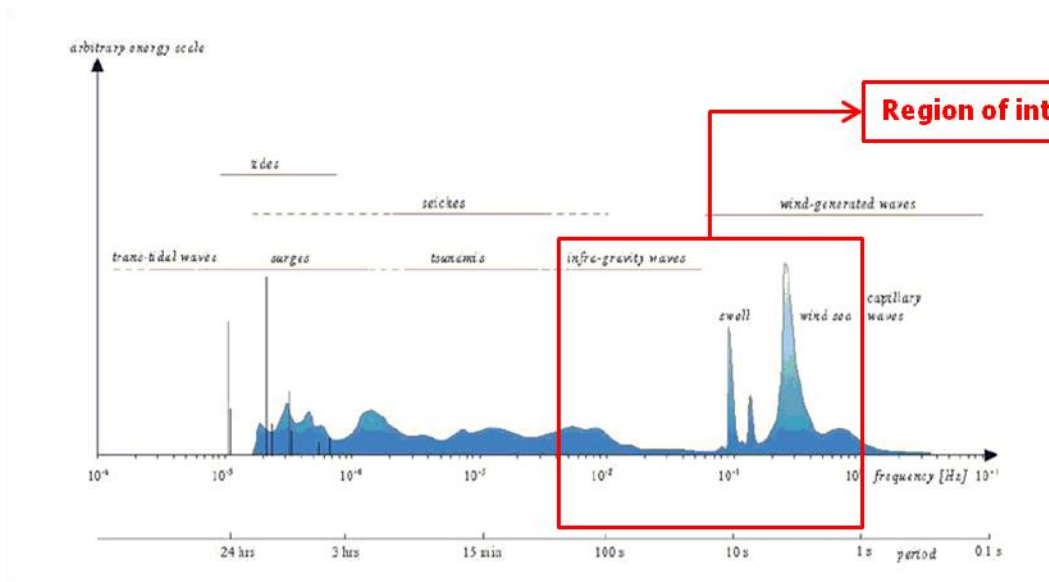


Figure 2.1: Frequencies and periods of the vertical motions encountered at the ocean surface, after Holthuijsen (2007)

<sup>1</sup> In the literature low-frequency motions were first referred to as 'surf-beat' and later with synonyms like 'infragravity waves', 'low-frequency waves' and 'subharmonics'. As a matter of preference the synonym infragravity wave is chosen in this research.

Short waves, which are generated by the wind, have typical frequencies of  $0.05\text{Hz} - 1\text{Hz}$  and are well known to travel in groups. These groups of short waves are associated with the generation of waves at lower frequencies, the IG-waves. As introduced in the introduction, IG-waves are surface gravity waves with typical frequencies of  $0.005\text{Hz} - 0.05\text{Hz}$  and relative small amplitudes (compared to the short waves).

## 2.3 Infragravity waves

### 2.3.1 Bound infragravity waves

Munk (1949) and Tucker (1950) were the first to report IG-waves in coastal waters and associated their existence with the group structure of the short waves (*Longuet-Higgins and Stewart, 1962*). After these initial observations numerous studies showed a strong correlation between the wave groups and the IG-waves, confirming that the IG-waves are locally generated by the short waves (*Elgar et al., 1992, Okihira et al., 1992, Herbers et al., 1994*).

Following the initial observations, *Longuet-Higgins and Stewart (1962)* showed the generation of a wave at the wave group scale due to the group structure of the incident short waves, using the concept of radiation stress. Figure 2.2 shows a bichromatic wave signal, which is a superposition of two sinusoidal wave signals. The modulation of the short wave height on wave group scale results in a gradient in the radiation stress on similar scale. This radiation stress gradient is balanced by a force that expels the fluid under regions of high waves, creating a local depression. The resulting pattern of the surface elevation is in anti-phase with and phase-locked to the wave groups (the pattern travels with the group velocity). This pattern is recognized as an IG-wave bound to the wave groups and referred to as a bound IG-wave.

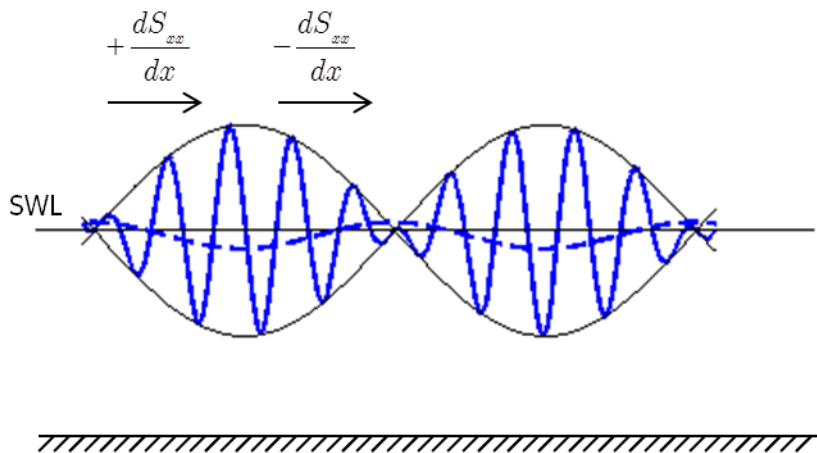


Figure 2.2: A visualization of a bichromatic short-wave signal (thick blue line), the wave group (black line), and a bound IG-wave (thick dashed blue line). SWL indicates the Still Water Level.

### **2.3.2 Free infragravity waves**

In the literature two generation mechanisms of free IG-waves are recognized. The first mechanism is the release of bound IG-waves in the surf zone. As the short waves propagate in shoreward direction, they start to break in the surf zone. IG-waves will not fully dissipate as they reach the shoreline and get reflected at the shoreline. *Longuet-Higgins and Stewart (1962)* argued that a bound IG-wave will be released in the surf zone as a free IG-wave in the process of short-wave breaking and shoreline reflection. Although numerous field measurements confirm this hypothesis, the actual release mechanism is unknown.

Another generation mechanism of free IG-waves is presented by *Symonds et al. (1982)*, who treated the variation of the breakpoint location in time due to the group structure of the incident waves. As the waves break, a strong gradient in the radiation stress develops due to the dissipation of wave energy. This radiation stress gradient results in a set-up at the shoreline, whereby higher waves result in a greater set-up than relative low waves. Due to the group structure of the incident waves and the resulting time-varying breakpoint, the resulting set-up is not constant but varies on the wave group time scale. This time varying set-up is recognized as a shoreward propagating free IG-wave, which is in phase with the wave groups. In addition to this shoreward propagating free IG-wave, this mechanism results in a seaward propagating free IG-wave which is out of phase with the wave groups.

Analysis of field measurements and flume experiments showed the relative importance of the two free IG-wave generation mechanisms. For relative mild slopes (ranging from 1:40 up to 1:200) both field (*Herbers et al., 1995a, Ruessink, 1998*) and flume (*Janssen et al., 2003*) observations showed the dominance of free IG-waves generated by the release of bound IG-waves. In contrast, flume experiments with a steep slope (1:10) showed a dominance of free IG-waves generated by the time-varying breakpoint (*Baldock et al., 2000*).

#### **Leaky and edge waves**

The above showed the generation of free IG-waves inside the surf zone by either the release of bound IG-waves or the time-varying breakpoint. Next the nearshore behaviour of the IG-waves generated by the above two mechanisms is considered.

Free IG-waves, generated by the release of bound IG-waves inside the surf-zone and the subsequent reflection at the shoreline, may escape the nearshore region and travel towards deeper waters (Figure 2.3, left panel). These free IG-waves are known as leaky waves. Alternatively, refraction may trap the reflected free IG-waves in the nearshore region. These trapped IG-waves are known as edge waves.

The above is also valid for free IG-waves generated by the time-varying breakpoint mechanism (Figure 2.3, right panel) as the seaward propagating IG-waves may be trapped in the nearshore as edge waves or may propagate towards deeper water as leaky waves.

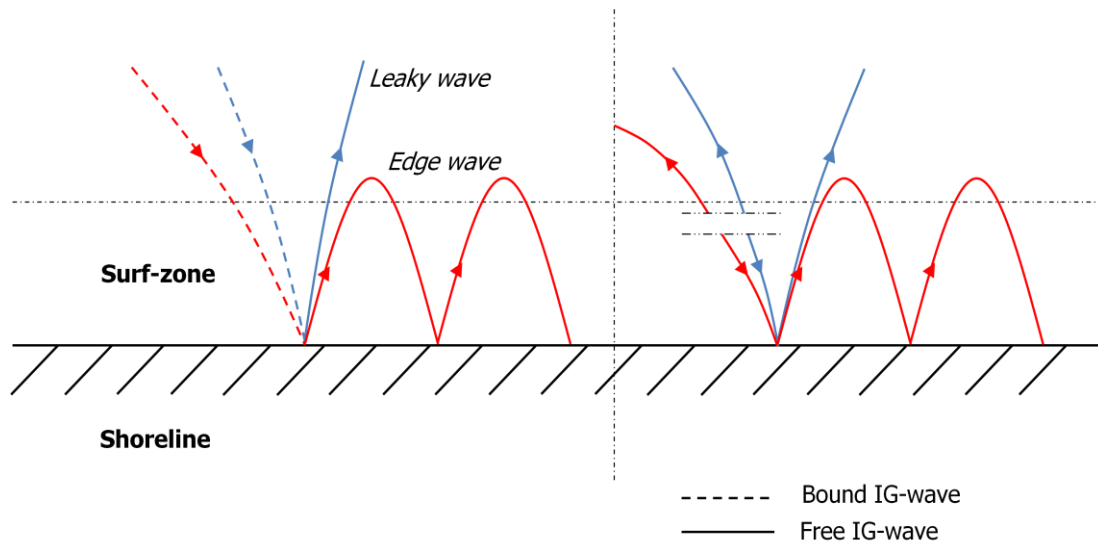


Figure 2.3: Visualization of the nearshore propagation of bound and free (leaky and edge) IG-waves. The left panel shows free IG-waves generated by the release of bound IG-waves and the right panel shows the generation of free IG-waves due to the time-varying breakpoint.

The above gives a visualization of the excitation of edge waves in near-shore regions. Edge waves are characterized by a complex nearshore surface elevation that is characterized by a sinusoidal variation in alongshore direction and an exponential variation in cross-shore direction. These edge waves were found as a solution at discrete mode numbers of the governing equations, for example, [Schäffer and Jonsson \(1992\)](#). The exponential form in cross-shore direction differs for various mode numbers: the mode number corresponds to the number of amplitude crossings with zero amplitude in cross-shore direction (Figure 2.4). A visualization of the edge wave surface elevation in alongshore and cross-shore direction is given in Figure 2.5.

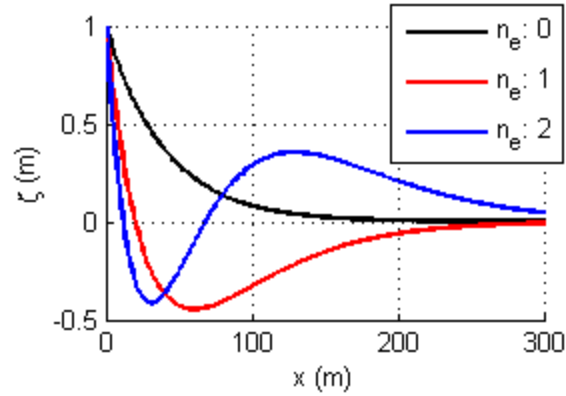


Figure 2.4: Visualization of the cross-shore structure of edge waves for three discrete mode numbers ( $n_e=0$ ,  $n_e=1$  and  $n_e=2$ ).

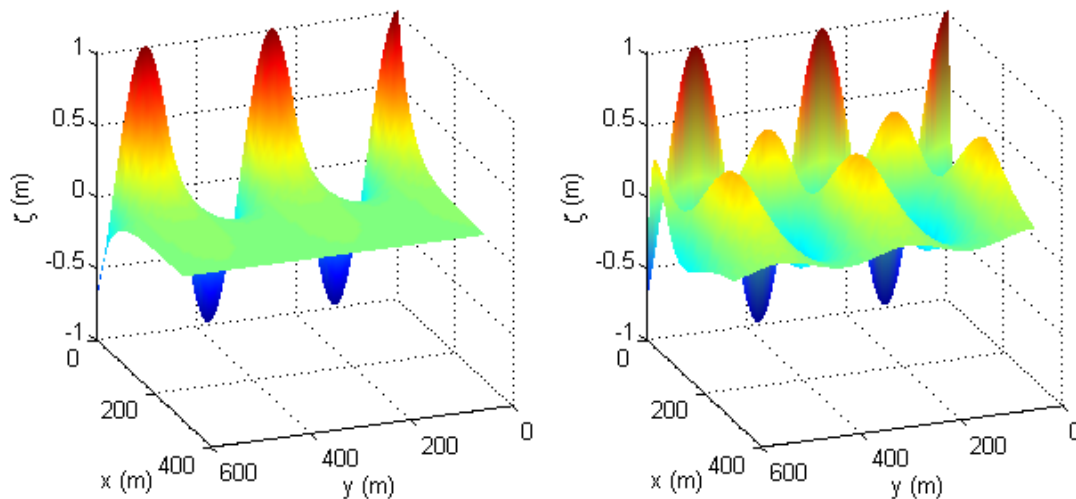


Figure 2.5, Visualization of the edge wave structure for  $n_e=0$  (left panel) and  $n_e=2$  (right panel).  $x$ : cross-shore direction and  $y$ : alongshore direction.

Schäffer and Jonsson (1992) gave a more comprehensive description of edge waves excited by the reflection of incoming IG-waves. The pattern of the surface elevation is associated with an interference pattern of the incoming and reflected IG-wave. Figure 2.6 shows a near-shore confined wave that propagates in shoreward direction and is reflected at the shoreline. If at the turning point the reflected IG-wave is out of phase with the incoming IG-wave, the amplitude of the interference pattern will be zero and the surface elevation pattern corresponds to a zero mode edge wave. If the IG-waves have smaller alongshore wave lengths (Figure 2.7), without going into further detail, one can imagine that the interference pattern will become more complex for decreasing alongshore wave numbers, with a surface elevation pattern similar to, for example, a second mode edge wave (Figure 2.5).

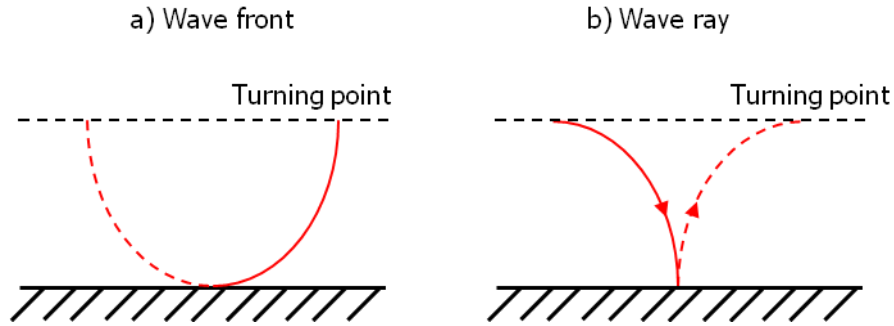


Figure 2.6: Incoming (solid red line) and reflected (dashed red line) IG-wave visualized as a wave front (a) and as a wave ray (b).

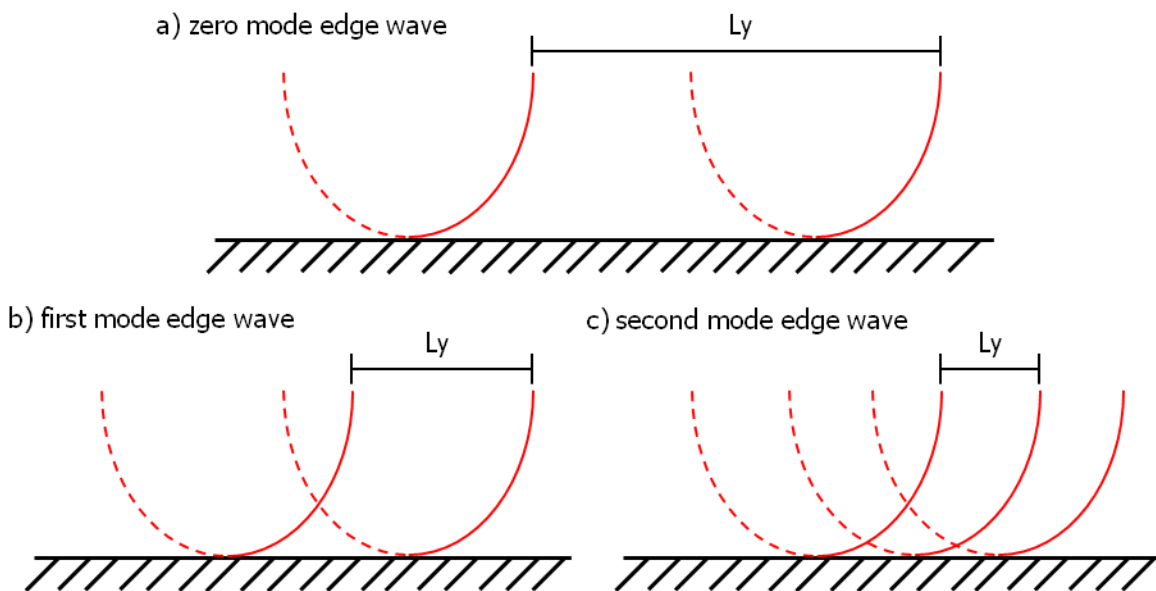


Figure 2.7: Wave front schematization for an incoming (full red line) and reflected (dashed red line) wave front. The wave fronts are shown for various alongshore wave lengths  $L_y$ .

## 2.4 Field measurements

Numerous field experiments have been conducted to gain insight in the nearshore IG-wave field. Measurements in intermediate water depths (ranging from 8 - 13m), which were located outside the surf zone, showed that IG-energies increase for more energetic short-wave conditions (*Elgar et al., 1992, Okihiro et al., 1992, Herbers et al., 1994*). Additionally a stronger infragravity response was found for more regular swell waves ( $0.04 < f < 0.14 \text{ Hz}$ ) compared to irregular wind waves ( $0.14 < f < 0.3 \text{ Hz}$ ), which is consistent with the theory of *Longuet-Higgins and Stewart (1962)*.

The studies showed that the IG-wave field is indeed a mixture of bound and free IG-waves. Both the bound and the free IG-energy levels increase for more energetic swell conditions, although the actual

dependency differs. Free IG-waves generally dominate the IG-wave field, but for more energetic swell conditions the bound IG-wave contribution increases. This increasing dominance of bound IG-waves is illustrated by the proportionality between swell energies  $E_{swell}$ , the bound IG-energies  $E_{bound}$  and the free IG-energies  $E_{free}$  (Herbers et al., 1995b):

$$E_{bound} \propto E_{swell}^2, \quad E_{free} \propto E_{swell} \quad (2.1)$$

Measurements in the nearshore and surf zone show that most free IG-waves could be trapped in the nearshore as edge waves, for example, *Oltman-Shay and Guza (1987); Okihiro et al. (1992)*. The actual occurrence and trapping of the reflected free IG-waves mainly depends on the global conditions. The shoreline morphology (rocky coasts or sandy beaches) is important for the reflection of the IG-waves, while the bathymetry controls the refraction of the free IG-waves (Herbers et al., 1995b).

Although measurements indicate that most free IG-waves could be trapped in the nearshore, this does not preclude free IG-waves to propagate to deeper water. Observations in the deep ocean showed the occurrence of leaky IG-waves originating from coastlines across the ocean basin (Webb et al., 1991). Additionally, Herbers et al. (1995a) observed shoreward propagating directionally narrow IG-waves in the nearshore that are not correlated to the local short waves and they reasoned that these IG-waves originate from remote locations.

## 2.5 Nearshore behaviour

The above gives a relative broad context of the occurrence of IG-waves in coastal regions. This section provides a more comprehensive description of the nearshore behaviour of IG-waves.

Figure 2.8 gives a visualization of the magnitude of an incoming bound IG-wave and the reflected free IG-wave for a gentle sloping beach, which is associated with the dominance of free IG-waves released by bound IG-waves. The incoming bound IG-wave grows as it propagates through the shoaling region, while the growth rate decreases as it reaches the surf zone. This growth in the shoaling region is associated with the shoaling of the incoming bound IG-waves and a continuous energy transfer from the short waves to the IG-waves, which was confirmed by analysis of field measurements (Sheremet et al., 2002) and flume experiments (Battjes et al., 2004). Inside the surf zone they both reasoned that the energy transfer to the IG-waves decreases and that dissipation of IG-wave energy becomes of increasing importance.

After reflection of the incoming IG-wave at the shoreline, the reflected IG-wave decreases in magnitude as it propagates in seaward direction (Figure 2.8). Sheremet et al. (2002) associated this decreasing magnitude with dissipation, refractive trapping and inverse shoaling of the reflected IG-waves. In a flume experiment (treating unidirectional waves perpendicular to the shore) no refractive trapping can occur

and the decreasing magnitude is only associated with inverse shoaling of seaward propagating IG-waves (Battjes et al., 2004).

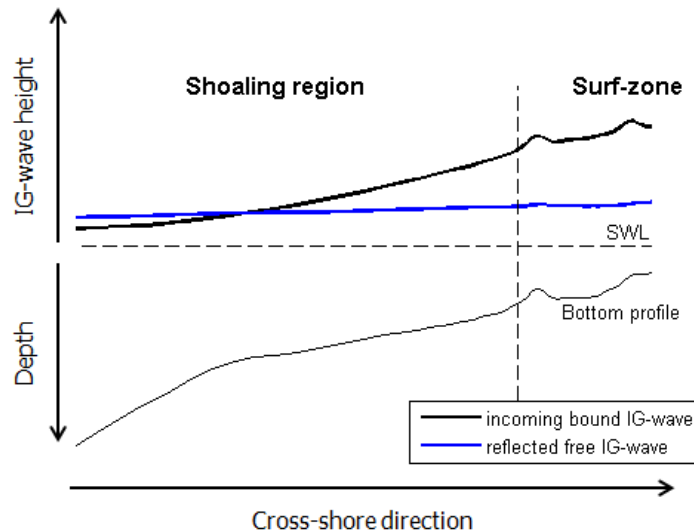


Figure 2.8: Visualization of the cross-shore variation of the incoming bound IG-wave height and reflected free IG-wave height over a barred beach profile (thin black line). The vertical dashed line indicates the location of initial wave breaking (the seaward edge of the surf zone) and the horizontal dashed line indicates the Still Water Level (SWL).

Although both the analysis of the field measurements and the flume experiments suggest a strong reflection of the IG-waves at the shoreline, IG-wave energy losses can be significant inside the surf zone, particularly at small water depths. Three sources of IG-wave energy loss are identified in the literature: (i) energy transfer from IG-waves to short waves; (ii) IG-wave breaking and (iii) bottom friction.

Thomson et al. (2006) and Henderson et al. (2006) attributed the energy loss of IG-waves in the surf zone to non-linear interactions between IG-waves and incident wave groups. This results in an energy transfer from the IG-waves to the short waves, and this energy is eventually dissipated by short-wave breaking. Van Dongeren et al. (2007) observed that IG-waves steepen and eventually break in the surf zone and linked this to self-self interactions between IG-waves. They further observed that IG-energy losses in the surf zone are partly due to an energy transfer to short waves, confirming (Thomson et al., 2006, Henderson et al., 2006), but that this IG-wave breaking becomes increasingly dominant in decreasing water depths. It is further found that bottom friction is a non dominant contribution to the energy decay of IG-waves (Thomson et al., 2006, Henderson et al., 2006, Van Dongeren et al., 2007).

### Frequency dependence

Battjes et al. (2004) further investigated the variation of the incoming and outgoing IG-wave height for various frequency bands, making a distinction between relative long and relative short IG-waves. The results of the study indicate that both the growth rate of the incoming bound IG-wave and the IG-wave

energy losses in the surf zone (controlling the shoreline reflection) are frequency dependent. This frequency dependence is captured in the normalized bed slope  $\beta_n$  (2.2) (*Battjes et al., 2004*), which expresses the relative depth change per wavelength as a function of the bed slope  $\beta$ , the gravitational acceleration  $g$ , the angular frequency of the IG-waves  $\omega$  and a representative water depth  $h_r$ . The normalized bed slope indicates how a given bed slope is relatively steep for long waves, while the same bed slope is relatively mild for a short wave.

$$\beta_n = \frac{\beta}{\omega} \sqrt{\frac{g}{h_r}} \quad (2.2)$$

The results of *Battjes et al. (2004)* showed that for relative mild slope regimes (roughly  $\beta_n < 0.1$ ) the growth rate of incoming bound IG-waves was larger, while the shoreline reflection was marginal (associated with greater IG-wave energy losses in the surf zone). In contrast, for relative steep slope regimes (roughly  $\beta_n \gg 0.1$ ) the growth rate of incoming bound IG-waves was small while incoming IG-waves were fully reflected at the shoreline, which has been associated with small IG-wave energy losses.



## 3 Methodology

---

It is essential to have a general understanding of the equations and the underlying assumptions of a numerical model to be able to interpret the model results. This chapter provides with a description of the fundamental equations of both numerical models used in this study, IDSB and SWASH.

### 3.1 IDSB

IDSB is a linear 1D surf-beat model that estimates the IG-wave response of directionally spread short waves incident on an alongshore uniform beach. The model only considers the generation of free IG-waves due to the release of bound IG-waves inside the surf zone and it does not include the time-varying breakpoint. In the following, first a description of the wave driver model is given (*Reniers and Battjes, 1997*), followed by the infragravity equations (*Reniers et al., 2002*). At last an overview of the model parameters is given, which are required to solve the governing equations.

#### 3.1.1 Wave driver model

The wave driver model provides the forcing of the infragravity waves; the group structure of the incident short waves. In IDSB the nearshore transformation of the short waves is modelled using a parametric spectral approach. In such an approach the short waves are expressed by a small number of characteristic parameters (e.g. the total wave energy, the peak period and the incident angle).

The nearshore transformation of the short waves is modelled with the concept of surface rollers (*Svendsen, 1984*). Waves propagating towards the shore start to break at a certain position and subsequently they transform into turbulent bores. Energy, released due the wave breaking is first transferred to a roller. This roller is defined as the rotating part resting on the wave front, which propagates with the phase velocity. A shear stress will develop due to the velocity difference between the roller and the underlying water particles and this stress dissipates the roller energy in the surf zone. This description of wave breaking with the concept of surface rollers results in a spatial lag between the wave breaking and the actual location of the dissipation: wave energy lost due to wave breaking is first transferred to the roller that will eventually dissipates the energy.

The set of equations describing the nearshore short-wave transformation is given by three differential equations: (i) the depth integrated short-wave averaged momentum equation; (ii) the wave energy balance and (iii) the roller energy balance.

#### **Depth integrated short-wave averaged momentum equations**

The first differential equation prescribes a balance between a gradient in the radiation stress and the mean surface elevation:

$$\frac{dS_{xx}}{dx} + \rho gh \frac{d\bar{\zeta}}{dx} = 0 \quad (3.1)$$

*Svendsen (1984)* derived a relation for the radiation stress including the roller concept (3.2), whereby the total radiation stress is expressed as a contribution of a wave  $S_{xx,w}$  and roller  $S_{xx,r}$  induced radiation stress. This radiation stress term is a function of the wave energy  $E_w$ , the roller energy  $E_r$ , the angle of incidence  $\theta$  and  $n$ , the ratio of the group velocity  $c_g$  over the phase velocity  $c$ .

$$S_{xx} = \underbrace{\left(n - \frac{1}{2} + n \cos^2 \theta\right) E_w}_{S_{xx,w}} + \underbrace{2E_r \cos^2 \theta}_{S_{xx,r}} \quad (3.2)$$

The angle of incidence, varying over the domain, is determined using Snell's law:

$$\frac{\sin \theta}{c} = \frac{\sin \theta_0}{c_0} \quad (3.3)$$

where the subscript 0 denotes the reference location, which is set at the offshore boundary.

To solve the first differential equation the roller and wave energy must be determined. These two terms result from the second and third differential equation: the wave energy balance and the roller energy balance, respectively.

### Wave energy balance

The wave energy balance (3.4) describes a balance between the wave energy, propagating with the group velocity under an angle of incidence, and a source term  $S$ , which describes the dissipation of wave energy.

$$\frac{d}{dx} (E_w c_g \cos \theta) = S \quad (3.4)$$

In the surf zone, the dissipation of wave energy is dominated by wave breaking. Several models exist to model the dissipation due to wave breaking. *Battjes and Janssen (1978)* proposed a widely accepted model valid for the dissipation of wave energy on the scale of several wave groups. This dissipation of wave energy (3.5) is a function of the dissipation of a single wave and the fraction of breaking waves  $Q_b$  (3.6). The dissipation of a single wave is modelled in analogy with a bore and is defined as a function of the maximum wave height  $H_{max}$ , the peak period and a coefficient  $\alpha$  of  $O(1)$ .

$$S = \frac{\rho g}{4T_p} \alpha H_{max}^2 Q_b \quad (3.5)$$

The fraction of breaking waves is calculated using an implicit relation that is a function of the root mean square wave height  $H_{rms}$  and the maximum wave height:

$$Q_b = \exp\left(-\frac{1 - Q_b}{\left(H_{rms}/H_{max}\right)^2}\right) \quad (3.6)$$

The maximum wave height is determined by (3.7), presented by *Battjes and Janssen (1978)*. This relation is an adaptation of Miche's criteria for the maximum wave height of a periodic wave of constant form. *Battjes and Janssen (1978)* altered the formula to be applied in shallow water and included a wave breaking parameter  $\gamma$  to account for the effect of the beach slope and for random waves.

$$H_{max} = \frac{0.88}{k} \tanh\left(\frac{\gamma kh}{0.88}\right) \quad (3.7)$$

### **Roller energy**

The third differential equation, the roller energy balance (*Stive and de Vriend, 1994*), prescribes a balance between the roller energy, propagating with the phase speed under an incident angle, the dissipation of wave energy and a shear stress  $\bar{\tau}_t$ . The dissipation of wave energy is a source term that transfers energy to the roller while the shear stress is a sink term that dissipates the roller energy.

$$S + \frac{d}{dx}(2E_r c \cos \theta) = c\bar{\tau}_t \quad (3.8)$$

The roller energy density is defined as a function of the roller area in the vertical plane ( $A_r$ ) and the length of the wave front ( $L_r$ ) (*Svendsen, 1984*):

$$E_r = \frac{1}{2} \frac{\rho A_r c^2}{L_r} \quad (3.9)$$

The shear stress, which dissipates the roller energy, balances the weight of the roller in the direction of the stress and is defined as (*Duncan, 1981*):

$$\bar{\tau}_t = \rho g A_r \frac{\sin \beta_r}{L_r} \quad (3.10)$$

where  $\beta_r$  stand for the slope of the wave front. Figure 3.1 gives a visualization of a surface roller and the roller dimensions ( $A_r, L_r, \beta_r$ ).

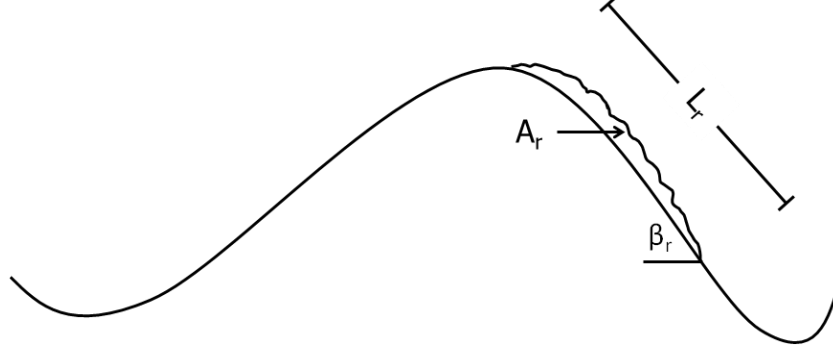


Figure 3.1: Visualization of a surface roller and the roller dimensions.

### 3.1.2 Infragravity equations

The equations describing the nearshore transformation of the infragravity waves are derived from the depth-integrated short-wave averaged equations (Svendsen, 2006). Combination of the continuity and momentum equations results in a single equation that describes the IG-surface elevation varying in time and space:

$$\frac{-1}{\rho g} \frac{\partial^2 \zeta_{IG}}{\partial t^2} + \frac{dh}{dx} \frac{\partial \zeta_{IG}}{\partial x} + h \frac{\partial^2 \zeta_{IG}}{\partial y^2} = \frac{-1}{\rho g} \left( \frac{\partial^2 S_{xx}}{\partial x^2} + \frac{2\partial^2 S_{yx}}{\partial x \partial y} + \frac{\partial^2 S_{yy}}{\partial y^2} \right) \quad (3.11)$$

Where  $\zeta_{IG}$  is the IG-wave surface elevation,  $h$  the total water depth including the mean setup ( $d + \bar{\zeta}$ ) and  $S_{ij}$  represents the radiation stress varying at wave group scale.

Consider a short-wave spectrum, a combination of two spectral components (spectral pair) can be interpreted as a wave group, forcing a bound IG-wave at the difference frequency of the spectral pair. Equation (3.11) is linear and this allows to consider each IG-component separately and to integrate all contributions to obtain the total IG-wave surface elevation. To obtain an equation that describes the IG-wave surface elevation of a single IG-component, all the terms in (3.11) must be defined as a term that corresponds to such a single IG-component.

The radiation stresses corresponding to a single spectral pair are defined as (3.12)-(3.14) (Schäffer, 1993). This term prescribes the variation of the radiation stress at wave group scale and is defined as the amplitude of the radiation stress varying in cross-shore direction ( $\hat{S}_{ij}$ ) times an exponent that represents the variation in time and in alongshore direction, as indicated by the comments in (3.14).

$$S_{xx}(x, y, t, f_1, f_2, k_{y,1}, k_{y,2}) = \frac{1}{2} \hat{S}_{xx}(x, f_1, f_2, k_{y,1}, k_{y,2}) \exp \left[ i(2\pi \Delta f t - \Delta k_y y) \right] + * \quad (3.12)$$

$$S_{xy}(x, y, t, f_1, f_2, k_{y,1}, k_{y,2}) = \frac{1}{2} \hat{S}_{xy}(x, f_1, f_2, k_{y,1}, k_{y,2}) \exp \left[ i(2\pi \Delta f t - \Delta k_y y) \right] + * \quad (3.13)$$

$$S_{yy}(x, y, t, f_1, f_2, k_{y,1}, k_{y,2}) = \underbrace{\frac{1}{2} \hat{S}_{yy}(x, f_1, f_2, k_{y,1}, k_{y,2})}_{\text{cross-shore varying radiation stress amplitude}} \overbrace{\exp\left[i(2\pi\Delta ft - \Delta k_y y)\right]}^{\text{variation in time and alongshore direction}} + * \quad (3.14)$$

In these equations \* denotes the complex conjugate,  $\Delta f$  the difference frequency (3.15),  $\Delta k_y$  the difference alongshore wave number (3.16) and  $\Delta k_x$  the difference cross-shore wave number (3.17). The wave numbers of each spectral component are obtained using the linear dispersion relation and the incidence angle of each spectral component is obtained using Snell's law.

$$\Delta f = f_1 - f_2 \quad (3.15)$$

$$\Delta k_y = k_{y,1} - k_{y,2} = k_1 \sin \theta_1 - k_2 \sin \theta_2 \quad (3.16)$$

$$\Delta k_x = k_{x,1} - k_{x,2} = k_1 \cos \theta_1 - k_2 \cos \theta_2 \quad (3.17)$$

The amplitudes of the cross-shore varying radiation stresses are defined as (3.18)-(3.20), in which the dependencies  $(x, f_1, f_2, k_{y,1}, k_{y,2})$  are dropped.

$$\hat{S}_{xx} = \left( \left( n(1 + \cos^2 \hat{\theta}) - \frac{1}{2} \right) \hat{E}_w + 2 \cos^2 \hat{\theta} \hat{E}_r \right) \exp \left[ -i \int \Delta k_x dx \right] \quad (3.18)$$

$$\hat{S}_{xy} = \left( \left( n \cos \hat{\theta} \sin \hat{\theta} \right) \hat{E}_w + 2 \cos \hat{\theta} \sin \hat{\theta} \hat{E}_r \right) \exp \left[ -i \int \Delta k_x dx \right] \quad (3.19)$$

$$\hat{S}_{yy} = \underbrace{\left( \left( n(1 + \sin^2 \hat{\theta}) - \frac{1}{2} \right) \hat{E}_w + 2 \sin^2 \hat{\theta} \hat{E}_r \right)}_{\text{Radiation stress amplitude}} \underbrace{\exp \left[ -i \int \Delta k_x dx \right]}_{\text{cross-shore variation}} \quad (3.20)$$

The exponent in the right hand side represents the variation in cross-shore direction at the wave group scale, which is the cross-shore wave length of the spectral pair, and the term between brackets is the radiation stress amplitude. The amplitude of the radiation stress is a function of the slowly modulating wave energy amplitude ( $\hat{E}_w$ ), the slowly modulating roller energy amplitude ( $\hat{E}_r$ ), the mean incidence angle of the spectral pair  $\hat{\theta}$  and the ratio of the group and phase velocity.  $\hat{E}_w$  and  $\hat{E}_r$  represent the amplitude of the wave energy and roller energy, respectively, varying at wave group scale and these terms correspond to a single spectral pair.

The mean angle of a spectral pair is defined as:

$$\hat{\theta} = \theta \tan\left(\frac{k_{y,1} + k_{y,2}}{k_{x,1} + k_{x,2}}\right) \quad (3.21)$$

The IG-wave surface elevation, which is of similar form as the radiation stresses (3.12)-(3.14) is defined as (3.22) (*Eckart, 1951*):

$$\zeta(x, y, t, f_1, f_2, k_{y,1}, k_{y,2}) = \frac{1}{2} \hat{\zeta}(x, f_1, f_2, k_{y,1}, k_{y,2}) \exp\left[i(2\pi\Delta ft - \Delta k_y y)\right] + * \quad (3.22)$$

By assuming alongshore uniform conditions and steady conditions, the exponent indicating the variation in time and alongshore direction is dropped in equations (3.12)-(3.14) and (3.22). Substituting these in (3.11) results in an equation describing the cross-shore variation of a single IG-wave component (3.23). A linear friction term is added to the equation to account for the dissipation due to, amongst others, the bottom friction (*Gallagher, 1971*). This friction term, a function of a resistance factor  $\mu$ , does not correctly represent the actual dissipation terms but provides a formulation to remove an equivalent amount of energy in the nearshore region (*Gallagher, 1971*).

$$\left(h \frac{d^2 \hat{\zeta}}{dx^2} + \frac{dh}{dx} \frac{d\hat{\zeta}}{dx} + \left(\frac{4\pi^2 \Delta f^2}{g} - \underbrace{\frac{i\mu 2\pi \Delta f}{g}}_{\text{linear friction term}} - h\Delta k_y^2\right) \hat{\zeta}\right) = \frac{1}{\rho g} \left(\frac{d^2 \hat{S}_{xx}}{dx^2} - 2i\Delta k_y \frac{d\hat{S}_{yx}}{dx} + \Delta k_y^2 \hat{S}_{yy}\right) \quad (3.23)$$

Gradients in the radiation stress provide the forcing mechanism of IG-waves and to obtain this forcing the amplitude of the wave ( $\hat{E}_w$ ) and roller ( $\hat{E}_r$ ) energy modulations on wave group scale must be computed throughout the domain.

The amplitude of the wave energy modulations results from a wave energy balance:

$$\frac{d\hat{E}_w(x, y, t, f_1, f_2, k_{y,1}, k_{y,2}) c_g \cos \hat{\theta}}{dx} = -\hat{D}_w(x, y, t, f_1, f_2, k_{y,1}, k_{y,2}) \quad (3.24)$$

The dissipation of the wave energy modulation  $\hat{D}_w$  is taken as a linear proportion of the total wave energy dissipation  $\bar{D}_w$  (3.25) (*Eldeberky and Battjes, 1996*). The total wave energy dissipation and the total wave energy are the equivalent of the wave energy dissipation and wave energy obtained from the wave driver model.

$$\hat{D}_w(x, y, t, f_1, f_2, k_{y,1}, k_{y,2}) = \frac{\hat{E}_w(x, y, t, f_1, f_2, k_{y,1}, k_{y,2})}{\bar{E}_w} \bar{D}_w \quad (3.25)$$

In a similar manner to the amplitude of the wave energy modulation, the amplitude of the roller energy modulation is obtained from a roller energy balance (Nairn et al., 1990, Stive and de Vriend, 1994):

$$\frac{d2\hat{E}_r(x, y, t, f_1, f_2, k_{y,1}, k_{y,2})c \cos \hat{\theta}}{dx} = \hat{D}_w(x, y, t, f_1, f_2, k_{y,1}, k_{y,2}) - \hat{D}_r(x, y, t, f_1, f_2, k_{y,1}, k_{y,2}) \quad (3.26)$$

The dissipation of the roller energy modulation  $\hat{D}_r$  is defined as a linear proportion of the total roller dissipation  $\bar{D}_r$  (3.27) and the total roller dissipation is the equivalent of the roller dissipation calculated in the wave driver model.

$$\hat{D}_r(x, y, t, f_1, f_2, k_{y,1}, k_{y,2}) = \frac{\hat{E}_w(x, y, t, f_1, f_2, k_{y,1}, k_{y,2})}{\bar{E}_w} \bar{D}_r \quad (3.27)$$

To obtain a solution for both energy balances, the amplitude of the slowly modulating wave and roller energy is defined at the cross-shore boundary. The slowly modulating roller energy is assumed zero, which is a fair assumption as the offshore boundary is located outside the surf zone. The amplitude of the slowly modulating wave energy is computed using the energy densities at the offshore boundary (denoted by subscript 0):

$$\hat{E}_{w,0} = \rho g \sqrt{E_0(f_1, \theta_1) E_0(f_2, \theta_2)} \delta f \delta \theta \quad (3.28)$$

The frequency resolution  $\delta f$  and directional  $\delta \theta$  resolution of the incident spectrum define the number of IG-components to be calculated, for a great (low) resolution more (less) individual IG-components are considered.

Two boundary conditions are specified to solve the equations. At the shoreline a zero flux (fully reflective) boundary condition is imposed and the offshore boundary includes an incoming bound wave and an (oblique) outgoing free wave (allowing reflected IG-waves to propagate out of the domain). The incoming bound wave is estimated from the frequency-directional short-wave spectrum, see Reniers et al. (2002) for details.

The resistance factor controlling the linear friction term is given by (3.29), in which  $c_f$  is the friction coefficient and  $|U|$  the mean velocity.

$$\mu = \frac{c_f |U|}{h} \quad (3.29)$$

The mean velocity is defined as a function of the short-wave near bed velocity  $U_{rms}$  and the alongshore current velocity  $V$ :

$$|U| = |U_{rms}^2 + V^2|^{1/2} \quad (3.30)$$

The short-wave near-bed velocity is defined as:

$$U_{rms} = \frac{\omega_p H_{rms}}{2 \sinh(k_p h)} \quad (3.31)$$

In which  $\omega_p$  and  $k_p$  is the radial frequency and wave number, respectively, corresponding to the peak frequency of the short-wave spectrum.  $H_{rms}$  is obtained from the wave driver model. The alongshore current velocity ( $V$ ) is not incorporated in the computations during this study.

### 3.1.3 Additional parameters

In the description of the model equations several parameters and coefficient were defined that requires specification. Here an overview of these parameters is given.

In the wave driver model the following parameters and coefficients are required: (i) coefficient  $\alpha$ ; (ii) wave breaking parameter and (iii) the steepness of the wave front. The infragravity equations only require the friction coefficient (iv).

- (i) The coefficient  $\alpha$  appears in the mean wave dissipation formulation and is a constant of order one.
- (ii) This wave breaking parameter controls the depth where the waves start to break. In this study the wave breaking parameter is estimated using an empirical formulation proposed by *Battjes and Stive (1985)*:

$$\gamma = 0.5 + 0.4 \tanh 33s_0 \quad (3.32)$$

In which  $s_0$  is the deep water wave steepness, which is the ratio of the deep water wave height  $H_0$  over the deep water wave length  $L_0$ .

- (iii) The wave front of the breaking wave is simulated as a bore of which  $\beta_r$  represents the slope. For laboratory experiments the angle varied between  $10^\circ$  and  $14.7^\circ$  (*Duncan, 1981*). The storage of wave energy in the roller depends on the angle of  $\beta_r$ ; large values result in small roller areas and thus very fast (up to instantaneous) dissipation.
- (iv) The dimensionless friction coefficient accounts for (amongst others) the bottom friction.

In the numerical implementation two additional parameters are defined that can be used to restrict the computational time: the spectrum threshold and the maximum number of computations. As the model computes each individual IG-wave this could amount to a great number of computations. The model starts with the energies near the peak of the spectrum and work's its way down. In this manner the

spectral pairs which have a significant contribution to the IG-surface elevation are computed first. The spectrum threshold and the maximum number of computations restrict the number of calculations thereby allowing the user to exclude spectral pairs that have a relative small contribution to the IG-surface elevation.

## 3.2 SWASH

SWASH (Simulating WAVes till SHore) is a hydrodynamic model for simulating non-hydrostatic, rotational free-surface flows. The model is based on the nonlinear shallow water equations including the non-hydrostatic pressure and is capable of describing the wave transformation in the surf- zone including non-linear interactions, wave-current interactions, wave breaking and run-up. In the following a description of the governing equations and the boundary conditions is given.

### 3.2.1 Governing equations

The governing equations are the non-linear shallow water equations including the non-hydrostatic pressure. SWASH considers both the depth-averaged version of these equations as the multi-layer case, by which the vertical domain is divided in several terrain following layers. In this section the purpose is to give insight in the equations and the underlying principles and they are therefore presented in depth-averaged form with Cartesian notation. Several papers provide a more detailed description of the governing equations (e.g. extension to 3D) and the numerical implementation (*Stelling and Zijlema, 2003, Zijlema and Stelling, 2005, 2008, Zijlema et al., 2011*).

The non-linear shallow water equations are derived from the incompressible Navier-Stokes equations that describe conservation of mass and momentum and are given by:

$$\frac{\partial \zeta}{\partial t} + \frac{\partial hu}{\partial x} + \frac{\partial hv}{\partial y} = 0 \quad (3.33)$$

$$\frac{\partial u}{\partial t} + u \frac{\partial u}{\partial x} + v \frac{\partial u}{\partial y} + g \frac{\partial \zeta}{\partial x} + \frac{1}{h} \int_{-d}^{\zeta} \frac{\partial q}{\partial x} dz + c_f \frac{u\sqrt{u^2 + v^2}}{h} = \frac{1}{h} \left( \frac{\partial h\tau_{xx}}{\partial x} + \frac{\partial h\tau_{xy}}{\partial y} \right) \quad (3.34)$$

$$\underbrace{\frac{\partial v}{\partial t}}_{\text{rate of change in time}} + \underbrace{u \frac{\partial v}{\partial x} + v \frac{\partial v}{\partial y}}_{\text{advection}} + \underbrace{g \frac{\partial \zeta}{\partial y}}_{\text{hydrostatic pressure}} + \underbrace{\frac{1}{h} \int_{-d}^{\zeta} \frac{\partial q}{\partial y} dz}_{\text{non-hydrostatic pressure}} + \underbrace{c_f \frac{v\sqrt{u^2 + v^2}}{h}}_{\text{bottom friction}} = \underbrace{\frac{1}{h} \left( \frac{\partial h\tau_{yx}}{\partial x} + \frac{\partial h\tau_{yy}}{\partial y} \right)}_{\text{turbulent stresses}} \quad (3.35)$$

The equations are solved in time  $t$  and in horizontal directions  $x$  and  $y$  (located at the still water depth  $d$  with the positive  $z$ -axis in upward direction),  $\zeta$  is the surface elevation measured from the still water depth ( $d$ ) so that the total depth is given by  $h = \zeta + d$ ,  $u$  and  $v$  are the depth averaged flow velocities in  $x$  and  $y$  direction, respectively, the non-hydrostatic pressure term is given by  $q$ ,  $c_f$  is the dimensionless bottom friction coefficient and  $\tau_{ij}$  represent the horizontal turbulent stresses.

The bottom friction coefficient is specified as a function based on the Manning's roughness coefficient  $n_m$  (3.36). With this formulation the friction coefficient is a function of the water depth and the bottom friction coefficient increases for a decreasing water depth.

$$c_f = \frac{n_m^2 g}{h^{1/3}} \quad (3.36)$$

The turbulent stresses are modelled as (3.37), in which  $\nu_t$  represents the eddy viscosity.

$$\tau_{xx} = 2\nu_t \frac{\partial u}{\partial x}, \quad \tau_{xy} = \nu_t \left( \frac{\partial v}{\partial x} + \frac{\partial u}{\partial y} \right), \quad \tau_{yy} = 2\nu_t \frac{\partial v}{\partial y} \quad (3.37)$$

### Wave breaking

In the formulations of the governing equations the free surface is tracked as a single value of the horizontal plane and due to these formulations the actual breaking is not considered as the actual breaking of the wave (e.g. spilling and overturning) is not included in such a representation. The dissipation of the breaking of the wave is therefore considered as a sub grid process. This approach does describe the evolution of a breaking wave, which is modelled in analogy with a bore (Figure 3.2), and *Zijlema and Stelling (2008)* have shown that with this approach the wave steepens up to an almost vertical front and that the location of wave breaking is predicted accurately.

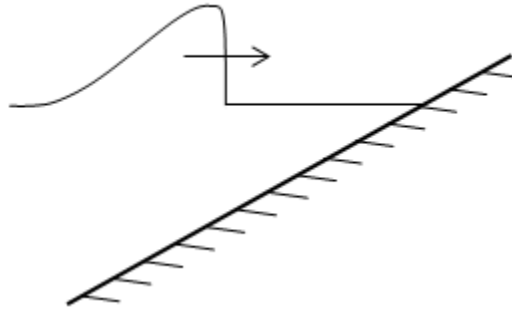


Figure 3.2: Bore representation of a breaking wave

As the location of wave breaking is accounted for in the equations, the sub grid turbulence due to the breaking of the wave must be accounted for by means of a turbulence model. For this purpose a turbulence model is applied and in this study the Prandtl mixing length hypothesis is used:

$$\nu_t = l_m^2 \sqrt{2 \left( \frac{\partial u}{\partial x} \right)^2 + \left( \frac{\partial v}{\partial y} \right)^2 + \left( \frac{\partial v}{\partial x} + \frac{\partial u}{\partial y} \right)^2} \quad (3.38)$$

where the mixing length  $l_m$  represents the length scale of the turbulent motion.

### 3.2.2 Boundary conditions

To solve the governing equations boundary conditions are required at the boundaries of the domain: the offshore boundary, the lateral boundaries and the shoreline. In this study the offshore boundary condition is prescribed by a weakly reflective condition that allows for incoming and outgoing waves. The lateral boundaries are chosen fully reflective and at the shoreline a wetting and drying algorithm is applied, which mimics the run-up at a beach.

The incoming waves at the offshore boundary are forced by a time signal of the surface elevation or an energy density spectrum. In case of directionally spread waves a two-dimensional spectrum is specified whereby the directional distribution (which is constant over the frequencies) is given by a  $\cos^m\theta$  distribution. The directional width of such a distribution is expressed by either the power  $m$  or with the standard deviation  $\sigma_\theta$  of the directional distribution.

#### Domain width

For the two dimensional simulations the domain width must be specified. The domain width must be chosen in such manner that the lateral boundaries do not influence the results in the region of interest. In this study the region of interest is a cross-shore array in the middle of the domain and due to the closed later boundaries the reflection of incident waves at the lateral boundary (Figure 3.3) may adversely influence the results inside the domain.

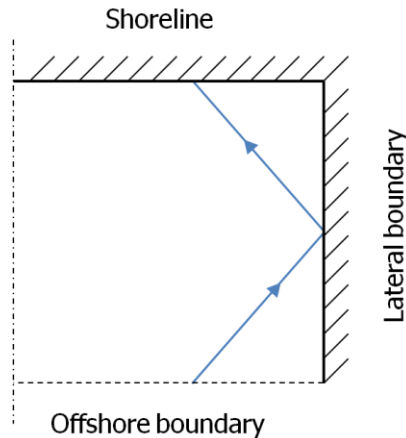


Figure 3.3: Visualization of the reflection of incident waves at the closed lateral boundaries

To prevent the lateral boundaries to influence the results inside the region of interest, the gauge array should be located outside the influence area of the lateral boundaries. The influence area of the lateral boundaries is estimated using the mean incident angle  $\theta$  and the directional width  $\sigma_\theta$  (Figure 3.4). The influence area is indicated by the thick and thin blue line, corresponding to the mean incident angle and the directional width, respectively. The width of the influence area is given by (3.39), in which  $L_x$  is the cross-shore domain length.

$$L_{min} = 2(L_{y,\sigma} + L_{y,\theta}) = 2 \tan(\sigma_\theta + \theta) L_x \quad (3.39)$$

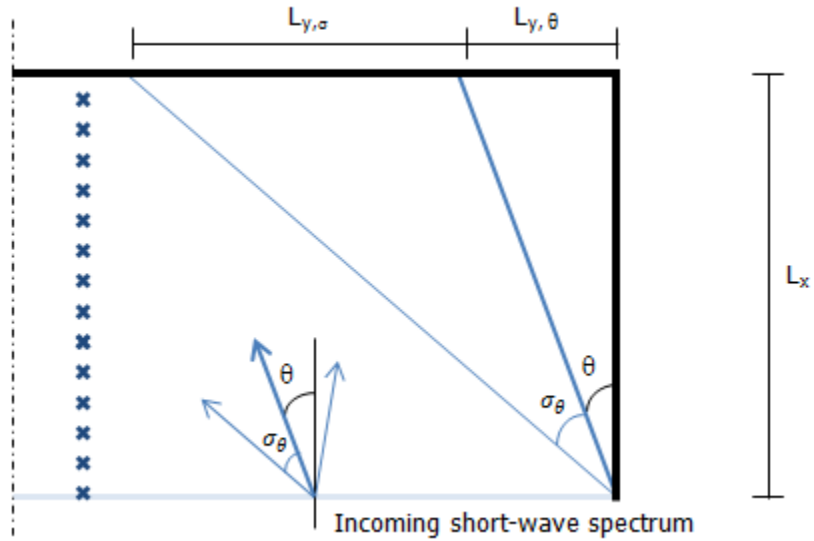


Figure 3.4: SWASH domain width, the gauges (location of interest) are indicated by the crosses and are located in the middle of the domain.

The domain width may influence the development of an alongshore current and edge waves, if for example the domain width is not sufficiently large the forming of both phenomena may be hampered. The influence of the domain width on these phenomena is not taken into account in the description of the minimal domain width. The minimal domain width is expected to give a lower limit of the actual required domain width. For increasing domain widths convergence is expected as the influence of the lateral boundary decreases in the centre of the domain.



## 4 Sensitivity study

---

### 4.1 Introduction

As the IG-wave conditions in coastal regions depend on the local wave climate and global bathymetry, it is valuable to gain insight in the model predictions for a range of conditions. In this Chapter the influence of several physical parameters on the IG-wave height predictions by IDSB and SWASH is investigated. Although no direct quantitative comparison can be made with measurements, the results will give insight in the dependency of the predicted IG-wave height on a physical parameter. As the dependency of the IG-wave conditions on wave conditions and bathymetry is known from theory, field measurements and laboratory studies, this knowledge can be used to assess the model predictions in a qualitative manner.

#### 4.1.1 Bathymetry and wave conditions

For the qualitative assessment a simple beach profile is considered that consists of a plane beach without any foreshore features, a constant slope and a maximum depth of 7.5m (Figure 4.1). The influence of the following parameters is investigated: (1) Bottom slope  $\beta$ ; (2) incident significant wave height  $H_{m0,0}$ ; (3) incident peak period  $T_{p,0}$ ; (4) directional spreading<sup>2</sup> and (5) incident mean wave direction  $\theta_0$ .

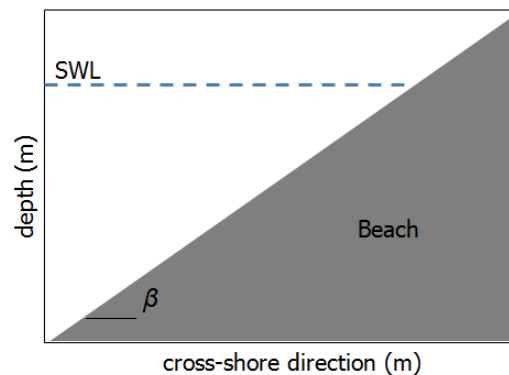


Figure 4.1: Schematic beach profile used in the sensitivity study, where the dashed line indicates the Still Water Level (SWL).

The influence of each physical parameter is investigated in a separate case (1 to 5), during which the remaining physical parameters are fixed (Table 4.1). In each case the specific physical parameter of

---

<sup>2</sup> The directional spreading of the parametric spectrum is controlled by the directional width of the directional distribution. In this study the directional width is expressed by means of the standard deviation ( $\sigma_\theta$ ) of the directional distribution, see for example, [Holthuijsen \(2007\)](#).

interest is varied during four simulations, of which each simulation (A/B/C/D) corresponds to a different value (Table 4.1).

An example: the first case considers the variation of the bottom slope for a range of 1:10-1:200 (simulation A-D). The wave conditions during the four simulations represent unidirectional waves, perpendicular to the shore, with an incident significant wave height of 1m and an incident peak period of 10s.

Table 4.1: Sensitivity, fixed parameters for each case.

Case	$\beta$ (m:m)	$H_{m0,0}$ (m)	$T_{p,0}$ (s)	$\sigma_\theta$ (°)	$\theta_0$ (°)
1, $\beta$	A/B/C/D	1	10	0	0
2, $H_{m0,0}$	1:40	A/B/C/D	10	0	0
3, $T_{p,0}$	1:40	1	A/B/C/D	0	0
4, $\sigma_\theta$	1:40	1	10	A/B/C/D	0
5, $\theta_0$	1:40	1	10	10	A/B/C/D

Table 4.2: Sensitivity, varying parameters for each simulation (A/B/C/D) per case (1-5).

Simulation	1, $\beta$ (m:m)	2, $H_{m0,0}$ (m)	3, $T_{p,0}$ (s)	4, $\sigma_\theta$ (°)	5, $\theta_0$ (°)
A	1:10	0.5	12	0	0
B	1:40	1	10	10	5
C	1:100	2	8	20	10
D	1:200	3	6	40	20

#### 4.1.2 Classification

The various wave conditions and bottom slopes are classified using a dimensionless parameter, the normalized bed slope (2.2). This dimensionless parameter gives an indication of the depth variation over the wave length and it was found that this parameter controls both the growth rate of the incoming bound IG-wave and the shoreline reflection of the incoming IG-waves, see Chapter 2.5.

In the calculation of the normalized bed slope a representative IG-wave frequency and representative depth is required. The first is based on the IG-frequencies found in the field (0.005Hz – 0.05Hz), and the representative IG-wave frequency is chosen at 0.0025Hz as it represents an IG-wave of 'intermediate' length. The representative depth is defined as the depth at the location of initial wave breaking, similar to *van Dongeren et al. (2007)*.

## 4.2 Model setup

The wave conditions forced at the offshore boundary are prescribed by a parametric shape (JONSWAP), significant wave height, peak period, directional spreading and mean incident angle.

### 4.2.1 IDSB

A grid spacing of 1m is chosen, which provides sufficient resolution for IG-waves with a frequency of 0.05Hz (corresponding to the relative short IG-wave lengths) at a depth of 0.1m ( $\sim 20$ m length). The wave breaking parameter  $\gamma$  is obtained using (3.32) (*Battjes and Stive, 1985*) and varies between 0.50 and 0.59. The friction coefficient is set at 0.005, which is of similar order of magnitude as the friction coefficient used in a previous study (*Reniers et al., 2002*). The remaining IDSB parameters are set at the value used in the same previous study (Table 4.3).

Table 4.3: IDSB parameters

$\beta$	$\alpha$	ndis	$e_{\text{trsh}}$
0.05	1	5	0.03

### 4.2.2 SWASH

The cases are simulated with one vertical layer and the application of a turbulence model, the Prandtl Mixing Length hypothesis, to account for dissipation due to wave breaking. Simulations treating unidirectional incident waves are modelled in 1D (in analogy with a flume) and simulations that consider oblique incident waves are modelled in 2D. The grid size is 1m in cross-shore and 2m in alongshore direction (for 2D cases) and the domain width used in the 2D simulations is shown in Table 4.4.

Table 4.4: Domain width (m) for the 2D simulations corresponding to the simulation (A/B/C/D) for a varying directional spreading (case 4, 2<sup>nd</sup> row) and for a varying mean incident angle (case 5, 3<sup>rd</sup> row).

	A	B	C	D
4, $\sigma_\theta$	1D	500	1000	1000
5, $\theta_0$	500	400	600	800

The total simulation time equals  $1^{1/2}$  hr which is long enough to get a good estimation of the spectral densities. To obtain stable simulations the time step is set at 0.02s and the maximum Courant number at 0.8. The mixing length is chosen equal to the incident significant wave height and the Manning coefficient is set at a realistic physical value of 0.01. For additional information regarding the number of vertical layers, grid size, domain width and the spin-up time, see Appendix D.

## 4.3 Results

Each of the five cases will be considered separately and for each case the influence of a varying physical parameter on the predicted significant IG-wave height is assessed. Note that the aim is to assess the influence of a physical parameter on the predicted IG-wave height and therefore no model comparisons are made.

The significant IG-wave height  $H_{m0,lo}$  is obtained by integrating the energy density spectra  $E(f)$  over the IG-wave frequency range (4.1), whereby the IG-wave frequency range is chosen similar to the range which is typically found in the field:

$$H_{m0,lo} = 4 \int_{0.005}^{0.05} E(f)df \quad (4.1)$$

### 4.3.1 Bottom slope

The bottom slope affects both the generation and dissipation of the IG-waves. The normalized bottom slope (2.2) appears to be a controlling parameter in this respect (see Chapter 2.5) whereby a mild slope regime is associated with significant growth of the incoming bound IG-waves and small shoreline reflection of the incoming IG-waves (i.e. significant IG-wave dissipation inside the surf zone) and vice versa for steep slopes. Table 4.5 shows a classification of the various bottom slopes in slope regimes that follow from the normalized bed slope  $\beta_n$  (2.2). The results indicate that all bottom slopes, except for the 1:10 slope, represent a mild slope regime.

Table 4.5: Overview of the non-dimensional parameters for the simulations of case 1 (varying bottom slope)

$\beta$	1:10	1:40	1:100	1:200
$\beta_n$	1.3	0.3	0.1	0.1
Slope regime	steep	mild	mild	mild

The results for IDSB show that, considering a mild slope regime, the overall IG-wave height increases for decreasing bottom slopes (Figure 4.2, left panel). For a steep slope regime (1:10 slope) IDSB predicts larger IG-wave heights compared with mild slope regimes. A possible explanation follows from the slope regime: for steep slope regimes the growth rate of the incoming bound IG-waves is expected to be small and the time-varying breakpoint mechanism may be the dominant generation mechanism. As the latter is not included in IDSB, the IDSB model is not valid for the prediction of IG-wave heights for steep slope regimes. Furthermore it is observed that inside the surf zone ( $x > 3/4 L$ ) the predicted IG-wave height increases for decreasing bottom slopes, which is in contrast with an increasing importance of IG-wave dissipation for mild slope regimes.

For SWASH the overall IG-wave height increases for decreasing bottom slope (Figure 4.2, right panel). The overall trend of the IG-wave height is similar for mild slope regimes while for a steep slope regime a distinctive different pattern is found with a discontinuity at roughly  $3/4 L$ . This distinctive different pattern for a 1:10 slope is linked to the time-varying breakpoint mechanism as this is expected to be the dominant generation mechanism. The results further indicate that the SWASH predicted IG-wave height decreases in the surf zone ( $x > 3/4 L$ ) and near the offshore boundary ( $x < 1/4 L$ ) for decreasing bottom slopes. The decrease of the IG-wave height inside the surf zone is associated with an increase of the IG-wave dissipation (which becomes of increasing importance for decreasing bottom slopes). As greater IG-wave dissipation results in a smaller magnitude of the reflected IG-wave, this in addition could explain the smaller IG-wave heights in the offshore region  $x < 1/4 L$  as the reflected IG-wave is of smaller magnitude.

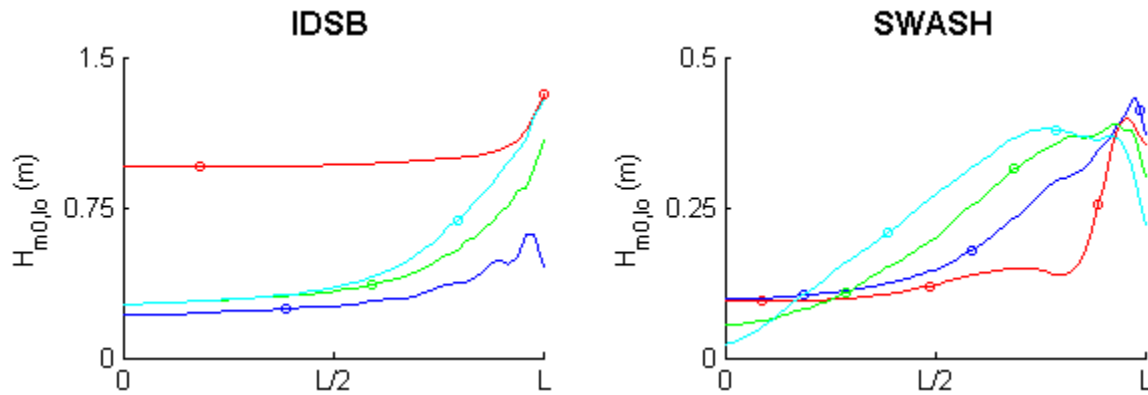


Figure 4.2: Significant IG-wave height ( $H_{m0,10}$ ) predicted by IDSB (left panel) and SWASH (right panel) for a varying bottom slope  $\beta$ . The colours represent the results for the various bottom slopes: red (1:10); blue (1:40); green (1:100) and cyan (1:200)

### 4.3.2 Incident significant wave height and peak period

Classification of the four simulations for case 2 (varying incident significant wave height) and case 3 (varying incident peak period) shows that all simulations of these two cases correspond to mild slope regimes (Table 4.5). As the generation and reflection of the IG-waves is similar for similar slope regimes the influence of the physical parameters of interest can be inspected carefully.

Table 4.6: Classification of the simulations for case 2 (varying incident significant wave height) and case 3 (varying incident peak period)

	Case 2: $H_{m0,0}$	Case 3: $T_{p,0}$
$\beta_n$	0.2-0.4	0.3
Slope regime	mild	mild

For increasing energetic conditions the magnitude of the IG-wave height, predicted by IDSB and SWASH, increases (Figure 4.3). This behaviour is similar to what is stated by theory (*Longuet-Higgins and Stewart, 1962*) and observed in field measurements, for example, *Herbers et al. (1995b)*.

The results for a variation of the peak period show that for decreasing peak periods the overall IG-wave height decreases (Figure 4.4). A decreasing peak period corresponds to a transition from regular swell waves to more irregular swell/wind waves. Both theory and field measurements showed a stronger IG-wave response to regular swell waves than to irregular wind waves, which is in accordance with the model predictions by IDSB and SWASH.

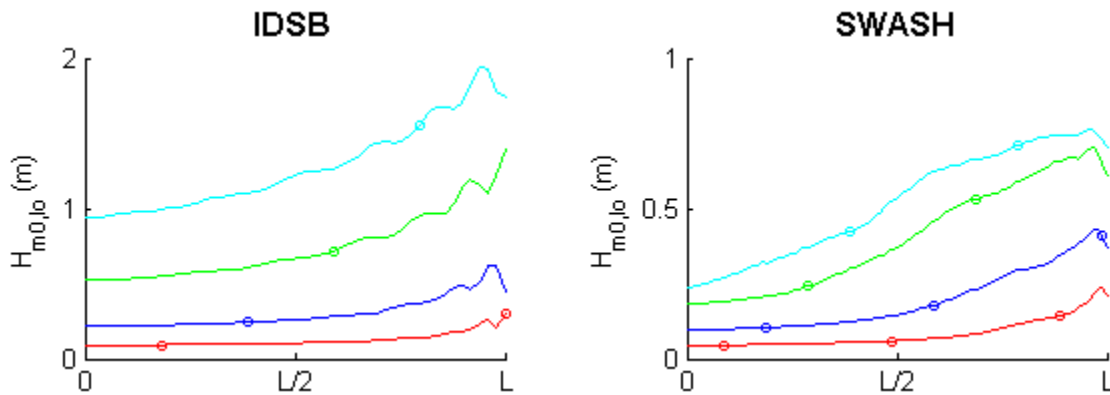


Figure 4.3: Significant IG-wave height ( $H_{m0,lo}$ ) predicted by IDSB (left panel) and SWASH (right panel) for a varying significant wave height  $H_{m0,0}$ . The colours represent the results for the various  $H_{m0,0}$ : red (0.5m); blue (1m); green (2m) and cyan (3m)

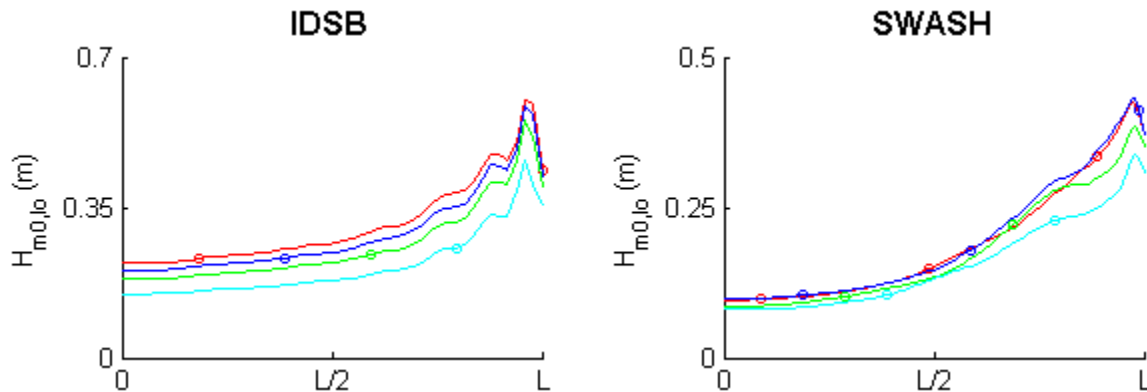


Figure 4.4: Significant IG-wave height ( $H_{m0,lo}$ ) predicted by IDSB (left panel) and SWASH (right panel) for a varying peak period  $T_{p,0}$ . The colours represent the results for the various  $T_{p,0}$ : red (12s); blue (10s); green (8s) and cyan (6s)

### 4.3.3 Directional width and mean incident angle

Where the previous cases considered unidirectional waves perpendicular to the shore, the following two cases treat oblique waves incident on a plane beach, thereby including the possible excitation of edge waves. Considering the slope regime, the simulations of both cases can be considered to represent mild slope regimes (Table 4.7).

Table 4.7: Classification of the simulations for case 2 (varying incident directional width) and case 3 (varying mean incident angle)

	Case 4: $\sigma_\theta$	Case 5: $\theta_0$
$\beta_n$	0.3	0.3
Slope regime	mild	mild

Overall the IG-wave height, predicted by IDSB and SWASH, decreases for an increasing directionally spread sea state (Figure 4.5). This dependence of the IG-wave height on the directional width is in accordance with theory (Longuet-Higgins and Stewart, 1962), which states a smaller IG-wave response for an increasing directional spreading.

Different behaviour is observed in the IDSB results for smaller directional widths: the predicted IG-wave height for unidirectional waves ( $0^\circ$  directional width) is smaller than for directional widths of  $10^\circ$  and  $20^\circ$ , which is in contrast with the theory.

For a varying mean incident angle the IG-wave height, predicted by IDSB and SWASH, is of similar order of magnitude (Figure 4.6). The influence of a varying mean incident angle on the IG-wave height appears to be negligible.

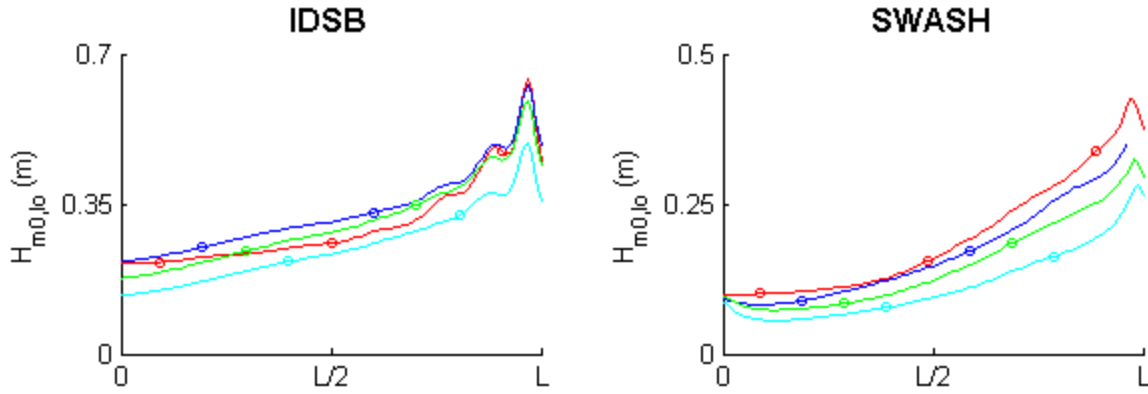


Figure 4.5: Significant IG-wave height ( $H_{m0,10}$ ) predicted by IDSB (left panel) and SWASH (right panel) for a varying directional width  $\sigma_\theta$ . The colours represent the results for the various  $\sigma_\theta$ : red ( $0^\circ$ ); blue ( $10^\circ$ ); green ( $20^\circ$ ) and cyan ( $40^\circ$ )

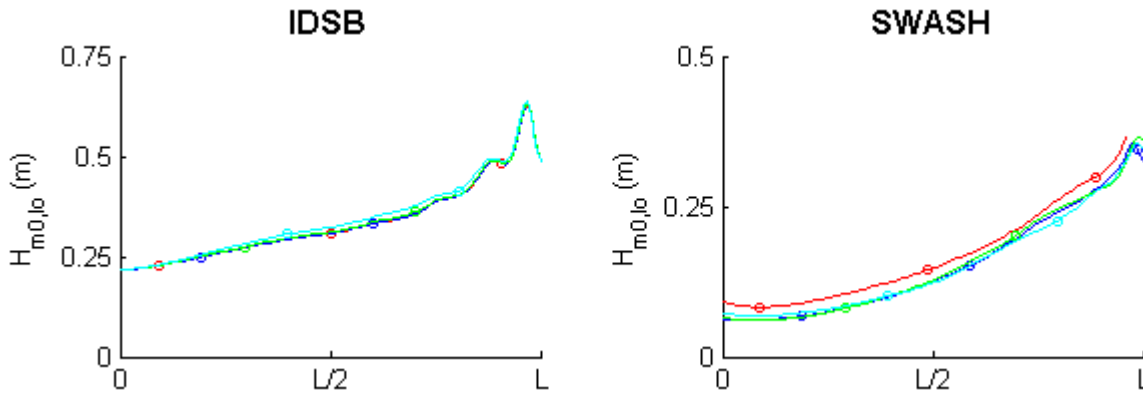


Figure 4.6: Significant IG-wave height ( $H_{m0,10}$ ) predicted by IDSB (left panel) and SWASH (right panel) for a varying mean incident angle  $\theta_0$ . The colours represent the results for the various  $\theta_0$ : red ( $0^\circ$ ); blue ( $5^\circ$ ); green ( $10^\circ$ ) and cyan ( $20^\circ$ )

### Wave number frequency spectra

The results for oblique incident waves are further analyzed by inspection of wave number frequency spectra. These show how the wave energies are distributed over the frequencies and alongshore wave numbers ( $k_y$ ) and thereby give insight in the structure of the IG-wave field and the possible existence of edge waves. In addition these spectra show the predominant alongshore direction of the IG-waves: energies at positive wave numbers are associated with waves travelling in positive alongshore direction and vice versa.

These wave number frequency spectra can therefore be applied to analyze the influence of the directional width and the mean incidence angle on the structure of the IG-wave field. In the following the wave number frequency spectra are only shown for the IDSB computations, as these spectra were not obtained for the SWASH computations.

In the wave number frequency spectra the free wave, deep water, dispersion curve and the edge wave dispersion curves are included. The deep water dispersion curve (4.2) gives insight in the existence of leaky and edge waves. Waves with greater alongshore wave numbers than the alongshore wave number according to (4.2) cannot exist in deep water and must be confined to the nearshore. Energies that fall within the region confined by the deep water dispersion curves are therefore associated with leaky waves while energies outside this region are associated with edge waves.

$$\omega = \sqrt{gk} \quad (4.2)$$

Furthermore, the edge wave dispersion curves give insight in the occurrence of distinct edge wave modes. The edge wave dispersion relationship for an alongshore uniform plane beach (4.3) is given by, for example, *Oltman-Shay and Guza (1987); Schäffer and Jonsson (1992)*.

$$\omega^2 = gk \sin(2n_e + 1)\beta, \text{ for } n = 0, 1, \dots \quad (4.3)$$

in which  $\omega$  is the radial frequency,  $n_e$  represents the edge wave mode number and  $\beta$  the bottom slope.

Figure 4.7 shows the wave number frequency spectra at a depth of 4m for the directional width case. The results show that for unidirectional waves all energies are located within the region confined by the deep water dispersion curve and this indicates the absence of edge waves. For oblique incident waves, energies are located at the edge wave dispersion curves and for increasing directional widths an increasing amount of energy is located at these dispersion curves and less energy is associated with leaky waves. This indicates that for an increasing short-wave directional spreading an increasing number of IG-waves is trapped in the nearshore. Furthermore the results show that the energies are evenly distributed over the positive and negative alongshore wave number which indicates that there is no predominant alongshore IG-wave direction.

The results for a varying mean incident angle show that a significant amount of the IG-wave energies is located at the edge wave dispersion curves (Figure 4.8). As the mean incident angle increases energies are predominantly located at positive alongshore wave numbers, associated with a predominant alongshore direction.

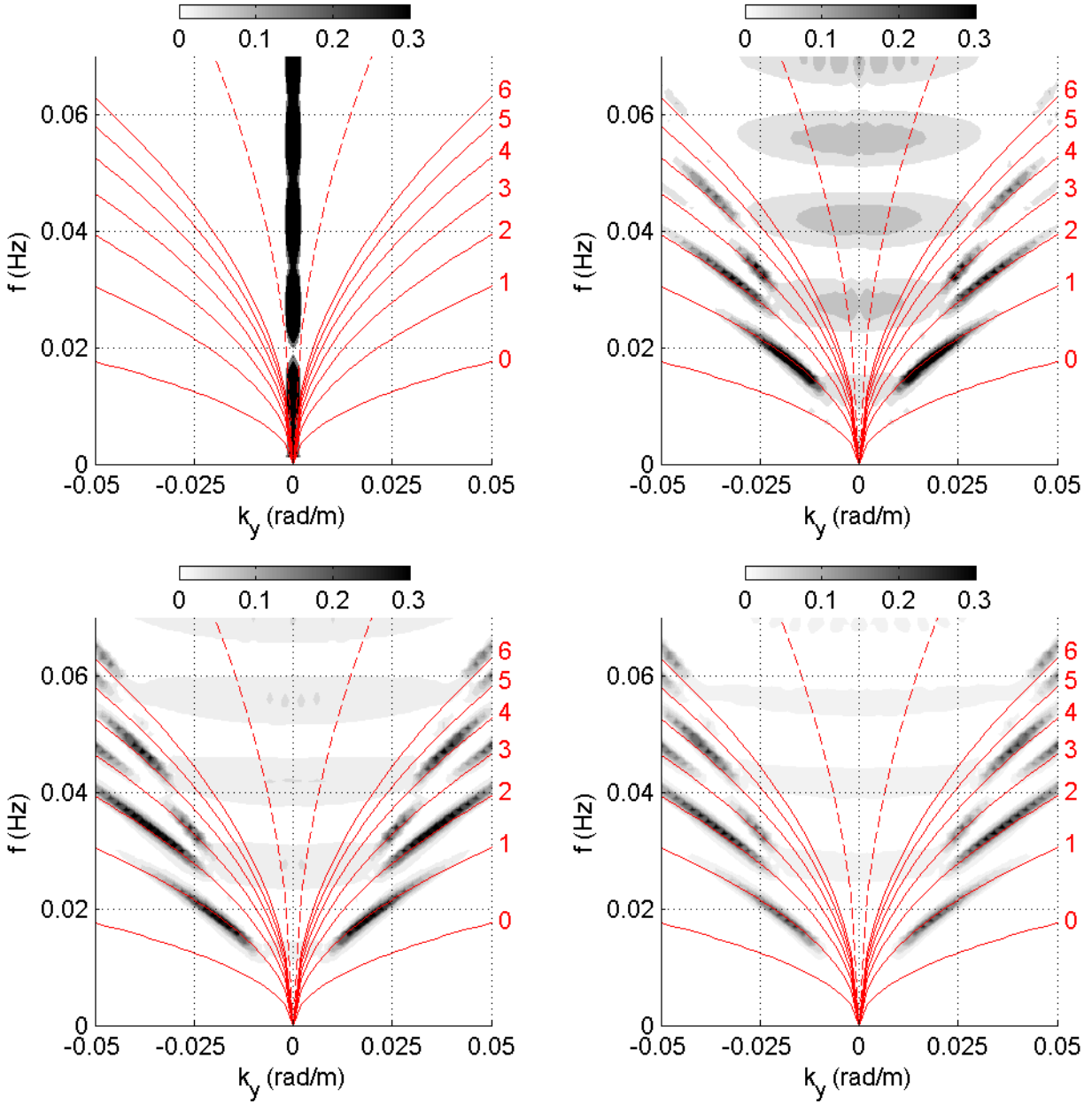


Figure 4.7: Wave-number spectra at 4m depth for a varying directional spreading including the dispersion relationship (dashed red line) and the edge wave dispersion curves (thick red lines). IDSB results for a directional spreading of:  $0^\circ$  (upper left panel);  $10^\circ$  (upper right panel);  $20^\circ$  (lower left panel) and  $40^\circ$  (lower right panel).

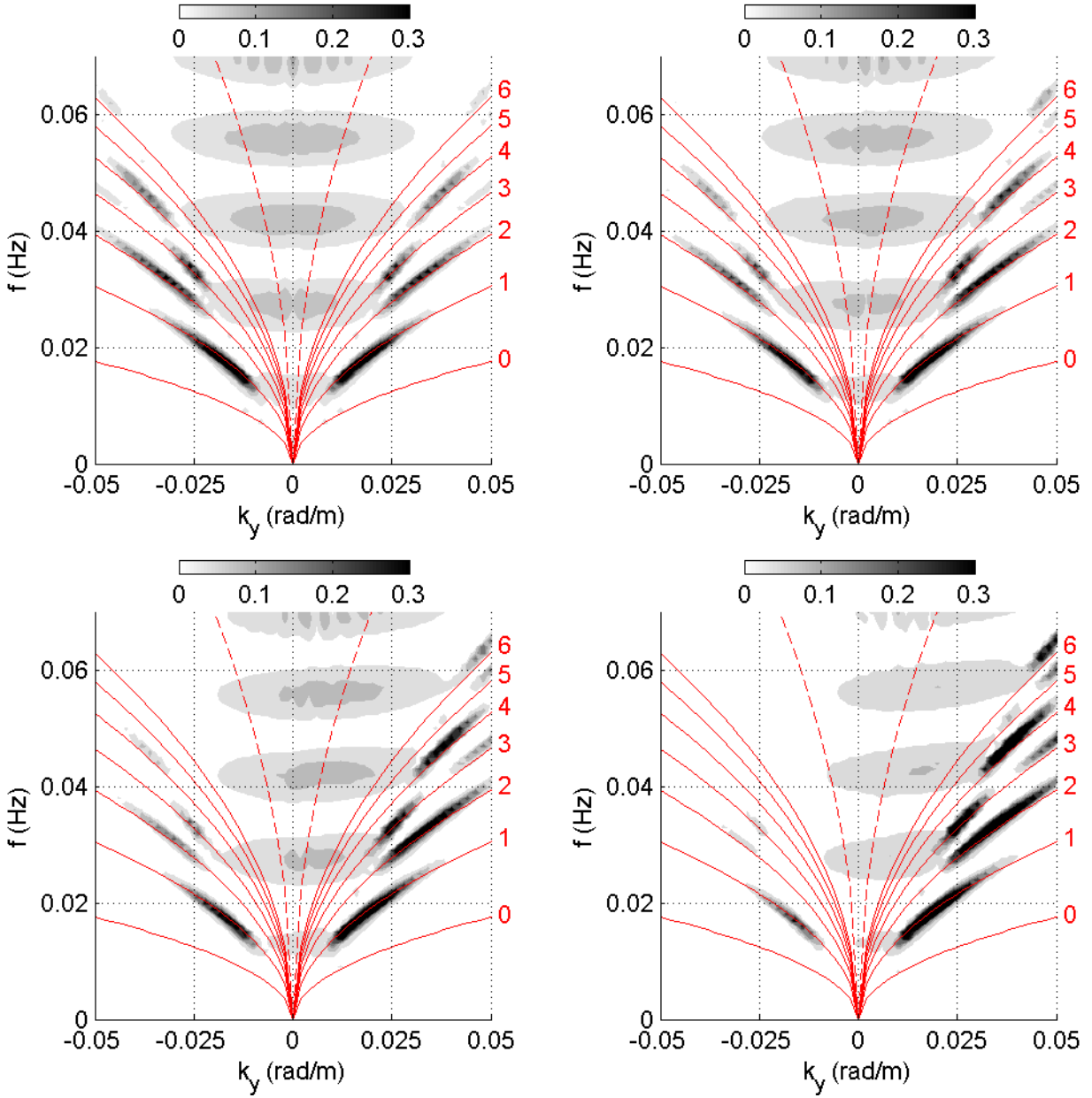


Figure 4.8: Wave-number spectra at 4m depth for a varying mean incident angle including the dispersion relationship for deep water (dashed red line) and the edge wave dispersion curves (thick red lines). IDSB results for  $\theta_0$ :  $0^\circ$  (upper left panel);  $5^\circ$  (upper right panel);  $10^\circ$  (lower left panel) and  $20^\circ$  (lower right panel).



## 5 Flume case, Boers

---

### 5.1 Introduction

In this Chapter the results of IDSB and SWASH are extensively analyzed to investigate whether they are capable of correctly simulating the near-shore generation and propagation of IG-waves. For this purpose the models will be used to reproduce a flume experiment. Flume experiments, in general, present an extensive data set that allows for a detailed analysis of the phenomena of interest. In this study the flume experiment by *Boers (1996)* is used, since he considered irregular waves propagating over a barred beach and these conditions are associated with the generation and propagation of IG-waves

### 5.2 Flume setup

*Boers (1996)* carried out experiments in the long research flume of the Fluid Mechanics Laboratory of the Department of Civil Engineering and Geosciences at Delft University of Technology. The bottom profile represents a surf zone with a barred beach, which is build up with sand with a smoothed concrete layer on top. Waves are forced using a piston-type wave board that allows for a translatory motion and the wave board control is equipped with a reflection compensation system to prevent reflection of outgoing waves at the wave board (re-reflection). To accurately reproduce reality in laboratory studies, the wave board control should incorporate a correct generation of bound IG-waves. Wave board forcing based on linear theory results in an incorrect forcing and the generation of spurious free waves at the same frequencies as the bound harmonics. To suppress the generation of these spurious free waves, the wave board control is accurate to second order (*Klopman and Van Leeuwen, 1990*). The flume experiment considered three different wave conditions. For each wave condition, multiple simulations with identical wave forcing were performed. In this manner a limited number of wave gauges is used to acquire measurements with high spatial resolution and for each wave condition this results in measurements of the surface elevation at 70 locations. The bottom profile and the gauge locations are shown in Figure 5.1.

The significant wave height and the peak period measured at  $x = 0m$  are shown in Table 5.1. The major difference between the wave conditions is the wave steepness; for wave condition 1A and 1B the wave steepness is such that wave breaking occurs throughout the whole flume. To accurately study the generation and the nearshore behaviour of the IG-waves, short-wave breaking should occur close to the shore and not throughout the whole flume. During wave condition 1B significant wave breaking is observed throughout the flume. For wave condition 1A the wave breaking is relatively mild in the offshore region and it is expected that the IG-wave phenomena can still be accurately examined. The generation and nearshore transformation of IG-waves is most evident for the mildest condition, condition 1C, where wave breaking is only observed shoreward of the bar. The numerical models are therefore used to reproduce wave condition 1A and 1C.

The domain is divided in two regions (I and II) based on the conditions that differ significantly for both regions (Figure 5.1). For both wave conditions (1A and 1C), region II ( $20\text{m} < x < 32\text{m}$ ) is dominated by wave-breaking. Region I ( $0\text{m} < x < 20\text{m}$ ) is associated with shoaling of incoming short waves and no significant breaking occurs, note that some wave-breaking is observed for wave condition 1A though this is not as significant as in region II.

Table 5.1: Wave height and peak period for the Boers wave conditions

Wave condition	$H_{m0}$ (m)	$T_p$ (s)
1A	0.157	2.05
1B	0.206	2.03
1C	0.103	3.33

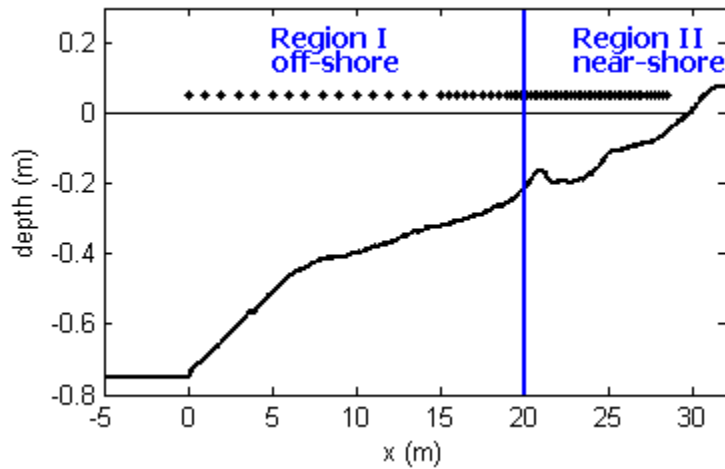


Figure 5.1: Bottom profile (thick line), mean water level (thin line) and gauge locations (dots)

### 5.3 Model setup

To accurately reproduce the wave forcing in the numerical models, the incoming waves should be correctly forced at the offshore boundary. The offshore boundary of the numerical models is set at the most offshore located wave gauge ( $x = 0m$ ) and the measured surface elevation at this location forms the basis of the wave forcing. The measured wave conditions at  $x = 0m$  are a combination of incoming short waves (assuming full short-wave dissipation at the beach), incoming bound IG-waves and reflected free IG-waves. For correct forcing of the wave conditions only the incoming wave contributions should be incorporated in the forcing of the numerical models.

In IDSB includes the incoming bound IG-waves, which are computed using the forced short-wave spectrum. Therefore only the incoming short-wave spectrum is required in IDSB. Bound IG-waves are, however, not incorporated in SWASH. In SWASH the waves, e.g. a time series of the surface elevation, are forced as incoming free waves. Including the incoming IG-waves in the wave forcing would result in incorrectly forcing the IG-waves and therefore only the short waves are considered in the SWASH wave forcing. In SWASH, the bound IG-waves have to develop inside the domain.

Figure 5.2 shows the spectral densities measured at  $x = 0m$  and the spectral densities forced in IDSB and SWASH. At the higher frequencies the forced spectral densities are an exact copy of the measured spectral densities while at lower frequencies (associated with IG-waves) the energies are not included in the forcing.

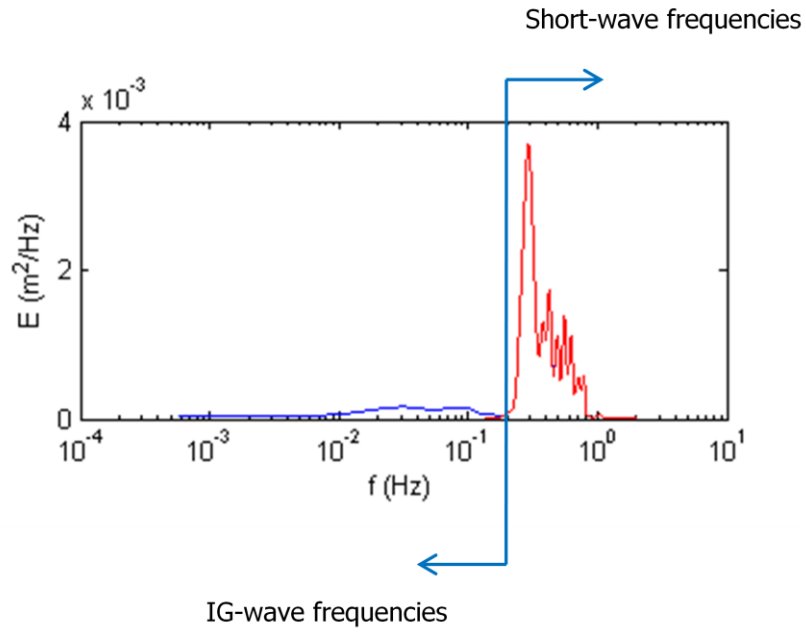


Figure 5.2: Spectral densities ( $\text{m}^2/\text{Hz}$ ) per frequency (Hz) corresponding to the short-wave forcing (red) and the measurements at  $x = 0\text{m}$  (blue) for wave condition 1C.

### 5.3.1 IDSB

The performance of IDSB is investigated by varying the wave breaking parameter  $\gamma$  and the friction coefficient  $c_f$ . The setup of the simulations for wave condition 1C, for a varying wave breaking parameter  $\gamma$  and friction coefficient  $c_f$  are shown in Table 5.2. The initial wave breaking parameter equals 0.5, which is the same order of magnitude as the wave breaking parameter resulting from equation (3.32) (Battjes and Stive, 1985). A variation of  $\pm 0.2$  is chosen and it is expected that such a range has a significant influence on the results. The friction coefficient is varied from 0.01-0.05 as several simulations showed a significant influence on the model results for such a range of friction coefficients.

The grid size is based on the limitation of 20 grid points per wave length. The smallest occurring wave length is approximated with the dispersion relationship considering the highest IG-frequency (0.2Hz) at the smallest depth of the domain (0.1m), which results in a wave length of 5m. Consequently, the grid size is set at 0.1m. The values of the other IDSB parameters are chosen equal to the values used in a previous study (Reniers et al., 2002) (Table 5.3) and the energy threshold is 3% to include most spectral pairs in the computations.

Table 5.2: IDSB setup for a varying wave breaking parameter (left panel) and a varying friction coefficient (right panel), wave condition 1C

	$\gamma$	$c_f$		$\gamma$	$c_f$
Run 1	0.3	0.03	Run 4	0.5	0.01
Run 2	0.5	0.03	Run 2	0.5	0.03
Run 3	0.7	0.03	Run 5	0.5	0.05

Table 5.3: Additional IDSB parameters

$\beta$	$\alpha$	ndis	$e_{trsh}$
0.05	1	5	0.03

### 5.3.2 SWASH

The performance of SWASH is investigated for two methods that account for the dissipation of wave energy due to short-wave breaking: (i) the application of the Prandtl mixing length hypothesis (turbulence model) and (ii) no turbulence model.

For both methods the performance of SWASH is investigated for a varying Manning coefficient, which controls the bottom friction. The Manning coefficients are set to vary between 0.01-0.05, representing a range of physical relevant values. For the first method (application of the turbulence model) the performance of SWASH is investigated for a varying mixing length. The initial mixing length is chosen at 0.13m, which is in accordance with Zijlema et al. (2011), and the sensitivity is investigated by varying it with  $\pm 0(0.03m)$ . For the case without the application of the turbulence model the number of vertical layers is varied between two and five vertical layers. Table 5.4 and Table 5.5 show the parameters for

the simulations of wave condition 1C for the case with the application of the turbulence model and the case without the turbulence model, respectively.

The grid size is chosen based on the same consideration as for the IDSB grid size. The minimal wave length is approximately 0.5m (max frequency of 1.5Hz at a depth of 0.1m) and the grid size is therefore set at 0.02m, which provides sufficient resolution.

The time step and the maximum Courant number are chosen in such manner that the simulations were stable. For the case with the turbulence model the time step is set at 0.001s with a maximum Courant number of 0.5, which is in accordance with *Zijlema et al. (2011)*. For the simulations without a turbulence model the time step is smaller for an increasing number of vertical layers. The maximum courant number is set at 0.5. The vertical layer distribution is chosen such that a higher resolution is obtained near the free surface, where the greatest gradients occur (e.g. velocity gradients due to breaking waves).

*Table 5.4: Setup 1C, turbulence model*

	# vertical layers (-)	$n_m$ (-)	$I_m$ (m)	Time step (s)
Run 1	1	0.01	0.13	0.001
Run 2	1	0.03	0.13	0.001
Run 3	1	0.05	0.13	0.001
Run 4	1	0.03	0.10	0.001
Run 5	1	0.03	0.15	0.001

*Table 5.5: Setup 1C, no turbulence model. The layer thickness is from top to bottom.*

Simulation	# vertical layers (-)	$n_m$ (-)	$I_m$ (m)	Layer distribution (% per layer)	Time step (s)
2V	2	0.03	-	50 50	0.00025
3V	3	0.03	-	15 30 55	0.00025
5V	5	0.03	-	15 15 15 15 40	0.0001

At the start of the simulations the initial conditions (velocities, surface elevation) are zero throughout the domain. From the start time onwards the wave conditions are forced resulting in shoreward propagating waves in the offshore domain while the nearshore domain is still undisturbed. Some spin-up time is required to allow the forcing to influence the whole domain and for the initial discontinuities to disappear. The spin-up time is defined as the time required for the model results to reach stationary conditions. For this flume experiment an initial estimation of the spin-up time follows from the time required for an IG-wave to propagate towards the shore, reflect at the shoreline, and to reach the offshore boundary. Results indicated that the integral wave parameters are not significantly influenced by the spin-up time (not shown).

## 5.4 Results

The model results are compared for the significant short-wave height  $H_{m0}$  and significant IG-wave height  $H_{m0,lo}$ . The significant wave height is obtained from the zeroth-order moment, which results from the integration of the energy density spectra over a frequency range. The energy density spectra are obtained with the Fourier transform with the application of smoothing in the frequency domain.

The frequency range of the IG-waves and short waves is based on the energy density spectra at the offshore boundary (Figure 5.2). The cut-off frequency defining the lower frequency limit of the short waves and the upper frequency limit of the IG-waves is set at 0.2Hz. This results in a short-wave frequency range of  $0.2Hz < f < 1.5Hz$ , in which the higher limit is set to include all energies at the higher frequencies, and a frequency range of the IG-waves of  $0.001Hz < f < 0.2Hz$ , in which the lower limit is set at a value  $f > 0$  to disregard the mean surface elevation.

### 5.4.1 IDSB

In the following, the results of IDSB will be primarily discussed for wave condition 1C, as this provides the most evident generation and propagation of IG-waves. First a baseline prediction is defined (the simulation corresponding to the best results) and the results of this baseline prediction are treated in detail. For IDSB the best results were obtained with a friction coefficient  $c_f$  of 0.03 and a wave breaking parameter  $\gamma$  of 0.5. Estimating the wave breaking parameter using (3.32) (*Battjes and Stive, 1985*) results in a similar value of  $\gamma$  as the baseline prediction.

#### Baseline prediction

Figure 5.3 and Figure 5.4 show the measured and computed energy densities at four locations in the domain (indicated by the black dots in the top panel of Figure 5.5) for all frequencies and the low frequencies, respectively. Note: the IDSB predicted energy densities correspond to the IG-waves only. An overview of the measured and the IDSB predicted energy density spectra throughout the domain is shown in Figure 5.6. The measured spectra show a decay of energy in shoreward direction at the short-wave frequencies and an increase of energy at the IG-frequencies. This is associated with short-wave breaking and the generation of IG-waves, respectively. In the nearshore (region II) the measured spectra show a clear nodal structure at the IG-frequencies, which is associated with the existence of standing IG-waves.

The IDSB computed spectra have an irregular form with distinctive peaks at certain frequencies. In shoreward direction the energies at the lower frequencies increases and a nodal structure appears, again associated with standing IG-waves. The computed and measured spectra compare poorly in the IG-frequencies as the location and magnitude of the peaks of the nodal structure is not reproduced well by IDSB.

The trend of the computed short wave height is in agreement with the measurements, Figure 5.5. The variation of the wave height in region I and the location of short-wave breaking (sharp decay in short-wave heights) is similar to the measurements. Although the spectra at the IG-frequencies compare poorly, the integrated IG-wave height has a similar magnitude and gradient in region I while IDSB over predicts the IG-wave height in region II. This over prediction might be due to several reasons: (i) under prediction of dissipation; (ii) an over prediction of IG-wave generation in region II and (iii) over prediction of the reflection.

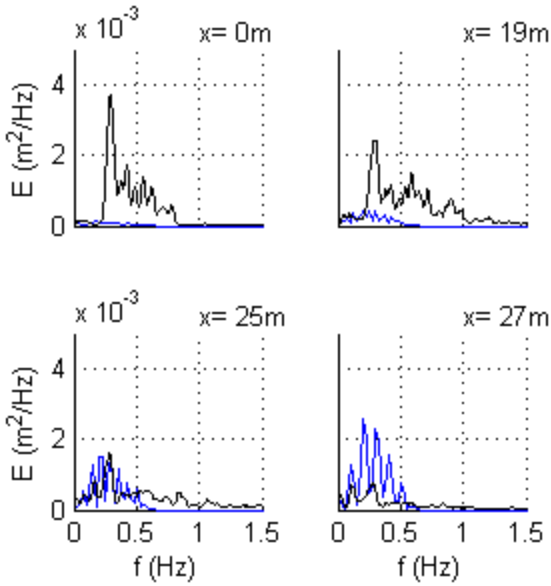


Figure 5.3: Energy density spectra ( $\text{m}^2/\text{Hz}$ ) at four locations for all frequencies, upper left panel  $x=0\text{m}$ , upper right panel  $x=19\text{m}$ , lower left panel  $x=25\text{m}$  and lower right panel  $x=27\text{m}$ . Measurements (black) and IDSB results for a friction coefficient of 0.03 and a wave breaking parameter of 0.5 (blue).

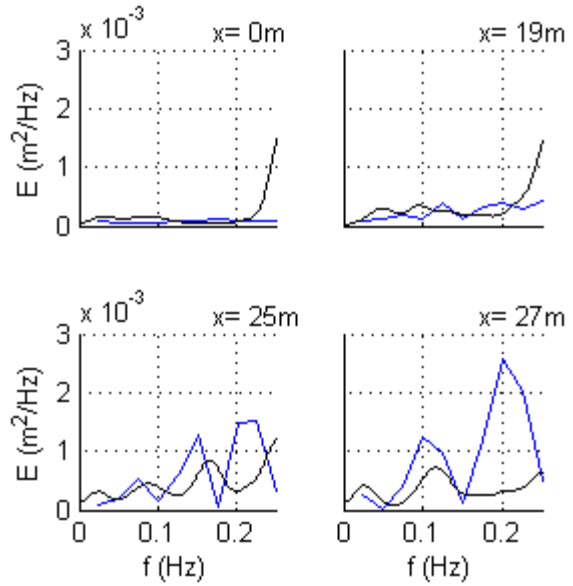


Figure 5.4: Energy density spectra ( $\text{m}^2/\text{Hz}$ ) at four locations for the IG-frequencies, upper left panel  $x=0\text{m}$ , upper right panel  $x=19\text{m}$ , lower left panel  $x=25\text{m}$  and lower right panel  $x=27\text{m}$ . Measurements (black) and IDSB results for a friction coefficient  $c_f$  of 0.03 and a wave breaking parameter  $\gamma$  of 0.5 (blue).

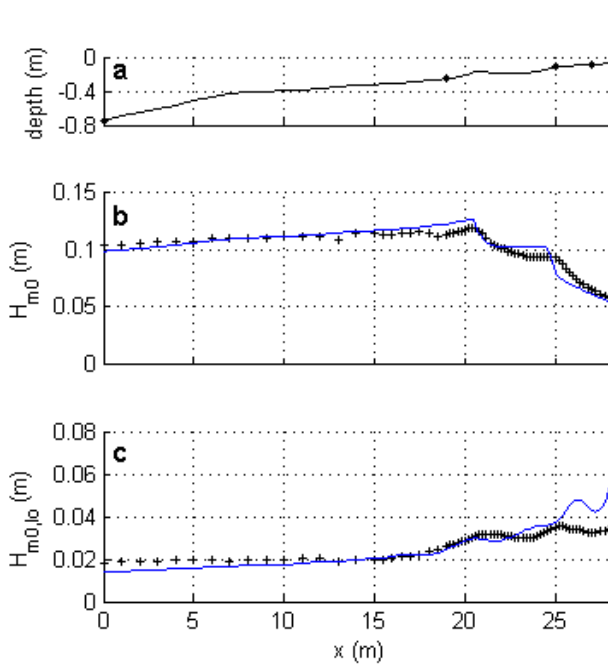


Figure 5.5: Cross-shore variation of  $H_{m0}$  and  $H_{m0,lo}$  for wave condition 1C. Measurements (black markers) and IDSB results (blue line) for a friction coefficient  $c_f$  of 0.03 and a wave breaking parameter  $\gamma$  of 0.5. (a) Bottom profile; (b)  $H_{m0}$  and (c)  $H_{m0,lo}$ . The black dots in (a) indicate the location of the spectral output.

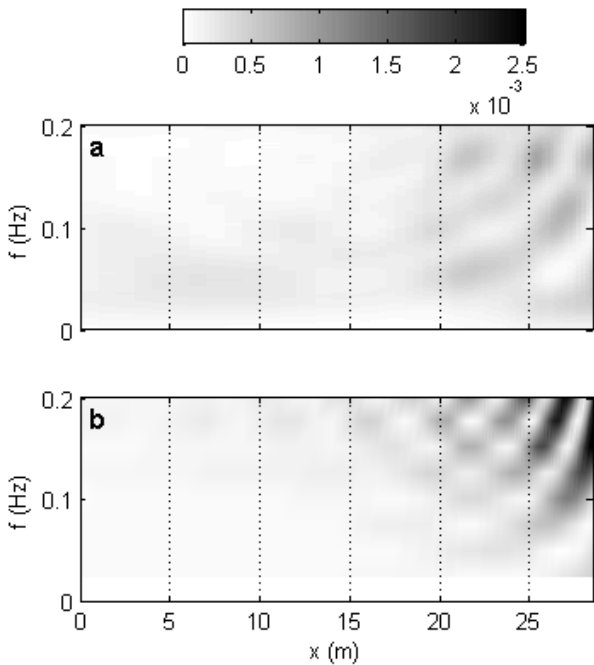


Figure 5.6: Overview of the energy densities ( $\text{m}^2/\text{Hz}$ ) at the IG-frequencies throughout the flume. (a) Measured and (b) IDSB results for a friction coefficient  $c_f$  of 0.03 and a wave breaking parameter  $\gamma$  of 0.5.

### Sensitivity to varying model parameters

A varying wave breaking parameter shows to significantly influence the short wave heights throughout the domain (Figure 5.7). The wave breaking parameter influences the location of wave breaking: for low values the waves break further offshore while for high values wave breaking occurs closer to the shoreline. The IG-wave height is influenced by the wave breaking parameter due to the magnitude of the short-wave heights: the short-wave height influences both the generation and the dissipation of the IG-waves. The results show that for wave breaking parameters of 0.5 and 0.7 the magnitude of the IG-wave height is similar in the surf zone ( $x > 25m$ ), while the magnitude of the IG-wave height is similar in the offshore region ( $x < 20m$ ) for a  $\gamma$  of 0.3 and 0.5. The actual influence of the short-wave height on the IG-wave height is not trivial, the short wave heights influences both the generation and the dissipation of the IG-waves.

A varying friction coefficient has no influence on the short-wave heights, while it significantly influences the IG-wave heights (Figure 5.8). The results show that the friction coefficient controls the magnitude of the IG-waves throughout the whole domain, while the overall trend remains similar.

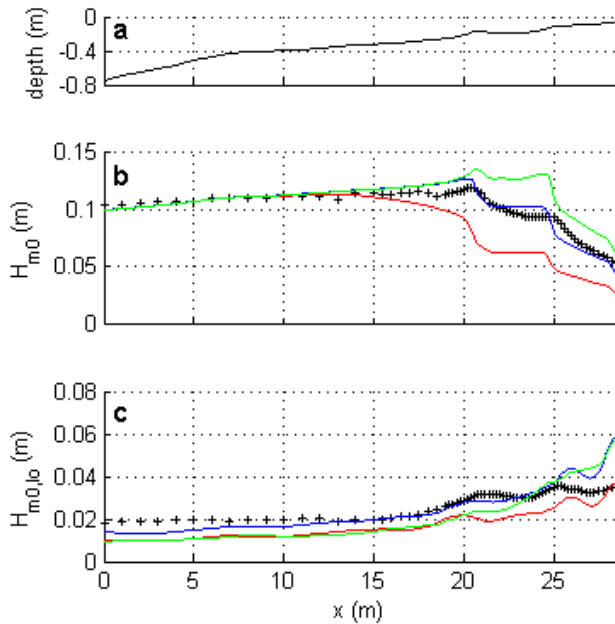


Figure 5.7: Influence of the wave breaking parameter for wave condition 1C. Measurements (black markers) and IDSB results for a wave breaking parameter  $\gamma$  of 0.3 (red), 0.5 (blue) and 0.7 (green) respectively. (a) bottom profile (b)  $H_{m0}$  (c)  $H_{m0,lo}$ .

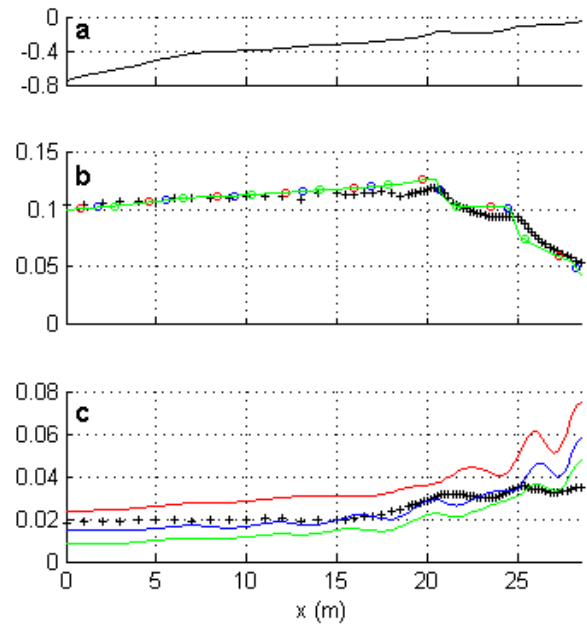


Figure 5.8: Influence of the friction coefficient for wave condition 1C. Measurements (black markers) and IDSB results for a friction coefficient  $c_f$  of 0.01 (red), 0.03 (blue) and 0.05 (green) respectively. (a) bottom profile (b)  $H_{m0}$  (c)  $H_{m0,lo}$ .

### Wave condition 1A

Although the phenomena of interest, the IG-waves, are less evident for wave condition 1A due to wave breaking in the offshore region (region I), the results give an indication of the model performance for a more severe wave condition whereby wave breaking occurs close to the offshore boundary.

Figure 5.9 show the results for the baseline prediction, in which the model set up is the same as for the baseline prediction for wave condition 1C (a friction coefficient of 0.03 and a wave breaking parameter of 0.5).

The short-wave heights predicted by IDSB are of similar order of magnitude in region II ( $x > 20$ ) while in region I the short-wave height is over predicted. As mentioned before, wave breaking was observed in region I for wave condition 1A, indicating that the deviation is due to an under prediction of the wave breaking in IDSB. This is confirmed by SWAN simulations for the same wave conditions that showed that wave breaking is the dominant dissipation mechanism<sup>3</sup>. The computed IG-wave height in Region I shows a good match with the measurements while in region II the IG-wave height is over predicted by IDSB.

Similar to wave condition 1C, the approximation of the wave breaking parameter by equation (3.32) (*Battjes and Stive, 1985*) results in a  $\gamma$  of 0.5 that corresponds to the value of the baseline prediction.

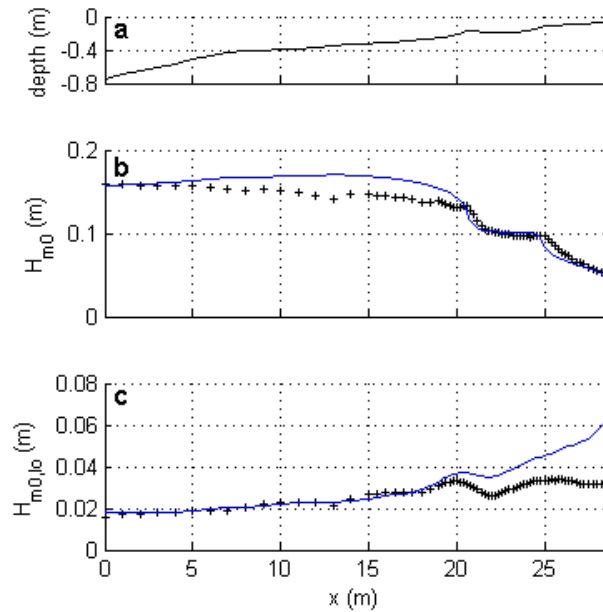


Figure 5.9: Cross-shore variation of  $H_{m0}$  and  $H_{m0,lo}$  for wave condition 1A. Measurements (black markers) and IDSB results (blue line) for a friction coefficient  $c_f$  of 0.03 and a wave breaking parameter  $\gamma$  of 0.5. (a) Bottom profile; (b)  $H_{m0}$  and (c)  $H_{m0,lo}$

<sup>3</sup> Personal communication, James Salmon (2011)

## 5.4.2 SWASH

### **Baseline prediction**

Similar to the results of IDSB, first the baseline prediction is discussed by considering the energy density spectra and the significant wave heights. The baseline prediction corresponds to the simulation with the application of the turbulence model and a mixing length of 0.13m and a Manning coefficient of 0.03.

Figure 5.10 and Figure 5.11 show the measured and SWASH computed energy densities at several locations for all frequencies and low frequencies, respectively. A cross-shore overview of the measured and SWASH computed spectral densities is given in Figure 5.13. The SWASH computed spectral densities are in good agreement with the measurements, including the energy decay at the short-wave frequencies and the increase of energy in IG-frequencies in shoreward direction. The energies in the IG-frequencies are, however, under predicted by SWASH compared the measurements. This under prediction is greatest at the offshore boundary and decreases towards the shore.

The short wave heights confirm the spectral observations, the SWASH computed short-wave heights agree well with the measurements (Figure 5.12). The location of the wave breaking and the magnitude of the decay are in good agreement. The IG-wave heights are under predicted in region I, as observed in the spectral results. In shoreward direction the gradient of the SWASH predicted IG-wave height is greater than the gradient of the measured IG-wave height and a smaller difference between the measured and SWASH predicted IG-wave heights is observed in region II.

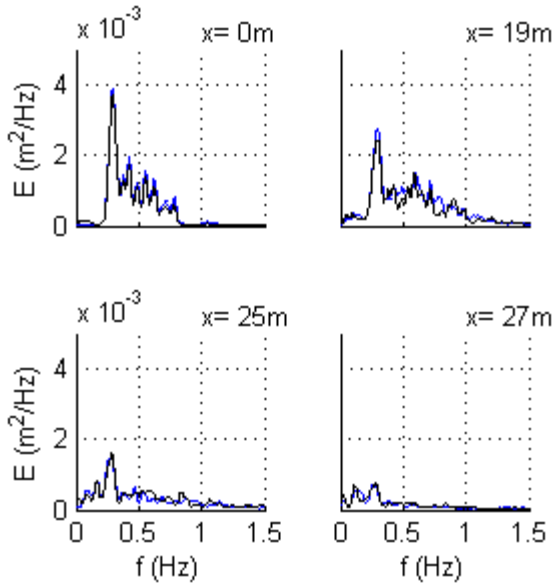


Figure 5.10: Energy density spectra ( $\text{m}^2/\text{Hz}$ ) at four locations for all frequencies, upper left panel  $x=0\text{m}$ , upper right panel  $x=19\text{m}$ , lower left panel  $x=25\text{m}$  and lower right panel  $x=27\text{m}$ . Measurements (black) and SWASH results for a mixing length  $l_m$  of  $0.13\text{m}$  and a Manning coefficient  $n_m$  of  $0.03$  (blue)

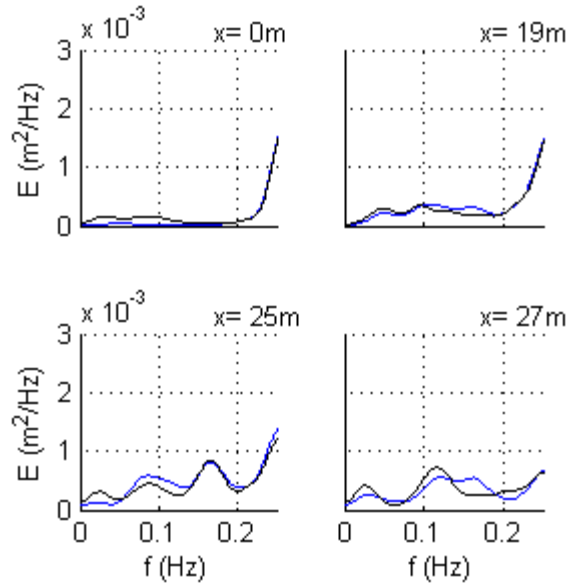


Figure 5.11: Energy density spectra ( $\text{m}^2/\text{Hz}$ ) at four locations for low frequencies, upper left panel  $x=0\text{m}$ , upper right panel  $x=19\text{m}$ , lower left panel  $x=25\text{m}$  and lower right panel  $x=27\text{m}$ . Measurements (black) and SWASH results for a mixing length  $l_m$  of  $0.13\text{m}$  and a Manning coefficient  $n_m$  of  $0.03$  (blue)

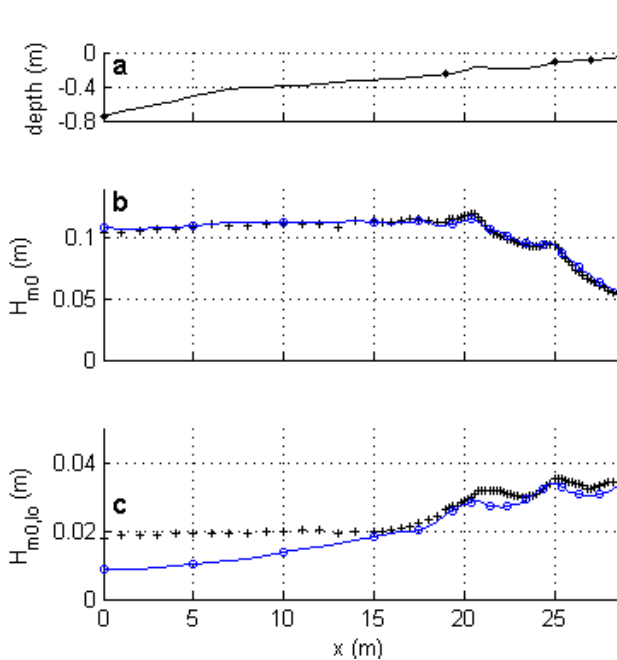


Figure 5.12: Cross-shore variation of  $H_{m0}$  and  $H_{m0,lo}$  for wave condition 1C.. Measurements (black markers) and SWASH results (blue) for one vertical layer, a Manning coefficient  $n_m$  of  $0.03$  and a mixing length  $l_m$  of  $0.13\text{m}$ . (a) Bottom profile (b) significant short-wave height (c) significant IG-wave height.

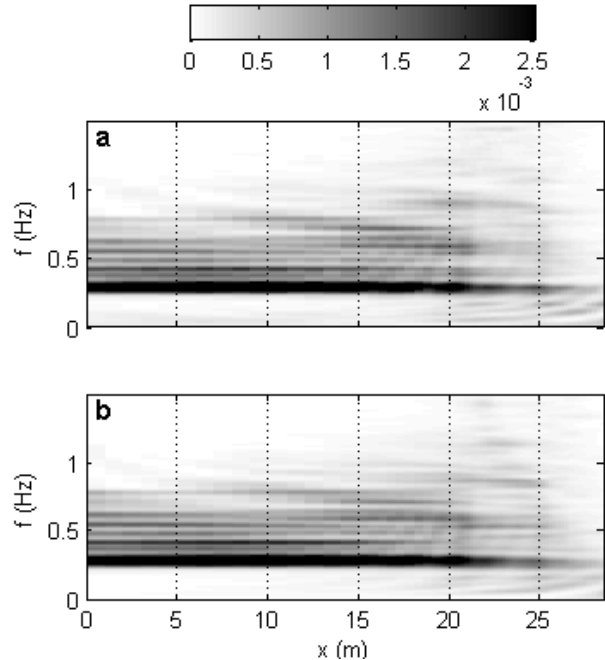


Figure 5.13: Overview of the energy densities ( $\text{m}^2/\text{Hz}$ ) throughout the flume. (a) Measured and (b) SWASH results for a mixing length  $l_m$  of  $0.13\text{m}$  and a Manning coefficient  $n_m$  of  $0.03$  (blue)

### Sensitivity to varying model parameters

Figure 5.14 and Figure 5.15 show the sensitivity of the model results to a varying mixing length and manning friction coefficient, respectively.

The mixing length controls the dissipation due to the turbulence term: a greater (smaller) mixing length results in more (less) dissipation. This is directly visible in the results as greater mixing lengths results in smaller short-wave heights while a smaller mixing length results in greater short-wave heights. The results show that a mixing varying with  $\sim 15\%$  has a small influence on the short-wave heights and a negligible influence on the IG-wave heights.

The Manning coefficient controls the dissipation due to bottom friction and the results show that larger (smaller) manning frictions results in smaller (larger) integral wave heights throughout the domain. The influence of the manning coefficient is most apparent for the IG-wave heights. The magnitude of the IG-wave heights is influenced by the manning coefficient, while the overall trend remains similar.

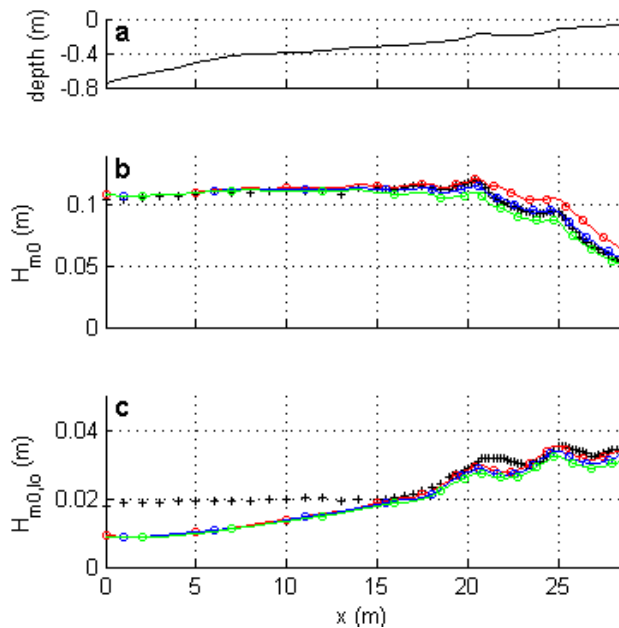


Figure 5.14: Influence of the mixing length, wave condition 1C. Measurements (black markers) and SWASH results for Manning coefficient  $n_m$  of 0.03 and a mixing length  $I_m$  of 0.10m (red), 0.13m (blue) and 0.16m (green) respectively. (a) Bottom profile (b)  $H_{m0}$  and (c)  $H_{m0,lo}$

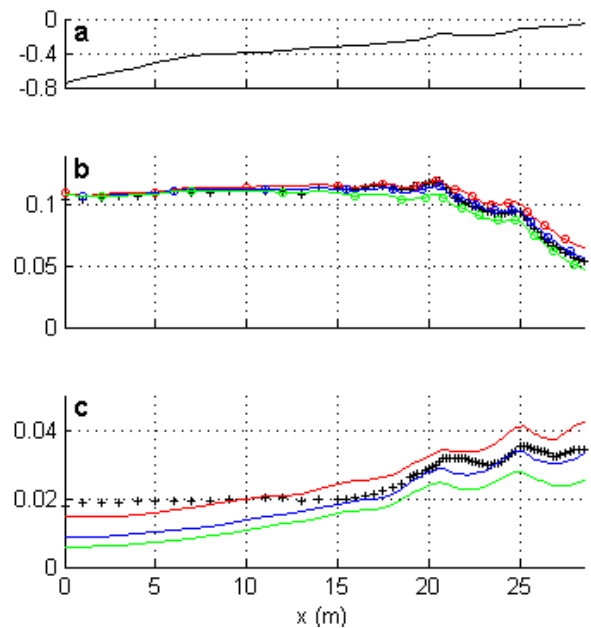


Figure 5.15: Influence of the manning coefficient, wave condition 1C. Measurements (black markers) and SWASH results for a mixing length  $I_m$  of 0.13m a Manning coefficient  $n_m$  of 0.01 (red), 0.03 (blue) and 0.05 (green) respectively. (a) Bottom profile (b)  $H_{m0}$  and (c)  $H_{m0,lo}$

### Influence number of vertical layers

Figure 5.16 shows the sensitivity of the number of vertical layers if no turbulence model is used. The short wave heights in region I are not influenced by a varying number of vertical layers. In region II the number of vertical layers has a significant influence on the computed short wave heights: for an increasing number of layers the decrease of the short-wave height is modelled more accurately.

The influence of the number of vertical layers on the IG-wave heights is small compared to the influence on the short wave heights. The influence on the IG-wave heights for a varying number of vertical layers is most apparent inside the surf zone.

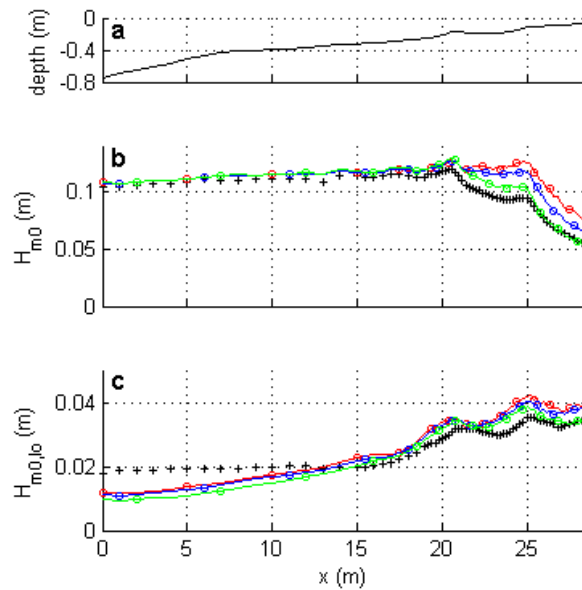


Figure 5.16: Influence of the number of vertical layers, no turbulence model, wave condition 1C. Measurements (black markers) and SWASH results for 2 (red), 3 (blue) and 5 (green) vertical layers with a Manning coefficient of  $0.03 n_m$ . (a) Bottom profile (b)  $H_{m0}$  and (c)  $H_{m0,lo}$

### Influence return current

A strong current may influence the shoaling and the wave breaking. To investigate if the SWASH results are influenced by a current the vertical structure of the mean current is investigated for the simulations with 3 and 5 vertical layers (Figure 5.17). Overall, the results show that a return current develops in region II. For three vertical layers a difference is observed at station B and C: the current profile does not show the presence of a return current. For five vertical layers this is only observed at station B. If the turbulence model is applied, the magnitude of the current decreases, associated with a damping of the current due to the turbulent stresses.

Currents can influence wave breaking and shoaling when its magnitude is strong compared to the phase velocity. At location C and D the phase velocity  $\sqrt{gd}$  equals 1.4 m/s and 1.0m/s respectively. It can be readily seen that for all results the magnitude of the mean current is at least a factor 5 lower. The physical relevance of the predicted current profiles is unclear, the results do however indicate that the current is not expected to significantly influence the nearshore behaviour of the waves.

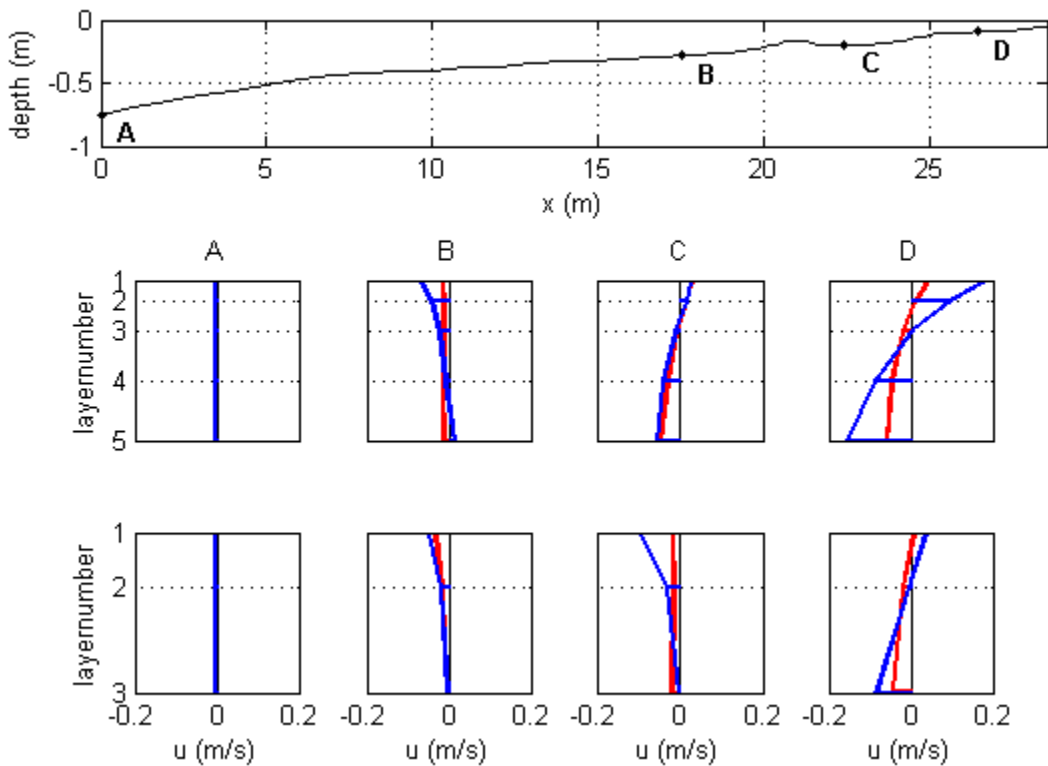


Figure 5.17: Vertical structure of the SWASH computed mean current for wave condition 1C, for simulations with (red) and without the turbulence model (blue). Time averaged velocity per layer (plotted relative to the depth at the centre of the layer) at four locations (A/B/C/D) for 5 (middle panel) and 3 (lower panel) vertical layers respectively.

### Wave condition 1A

Similar to the results for wave condition 1C, the baseline prediction is shown here (corresponding to a mixing length of 0.13m and a Manning coefficient of 0.03). For wave condition 1A, SWASH accurately predicts the short wave heights throughout the domain. The IG-wave heights are under estimated in region I while a better match is obtained in region II. In contrary to the observations for wave condition 1C, the IG-wave heights are over predicted by SWASH close to the shore ( $x > 20m$ ).

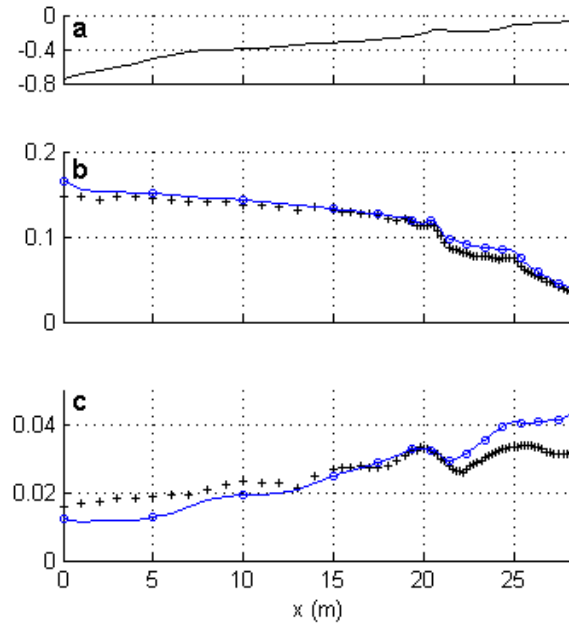


Figure 5.18: Cross-shore variation of  $H_{m0}$  and  $H_{m0,lo}$  for wave condition 1A. Measurements (black markers) and SWASH results (blue line) for mixing length  $I_m$  of 0.13 and a Manning coefficient  $m_n$  of 0.03. (a) Bottom profile; (b)  $H_{m0}$  and (c)  $H_{m0,lo}$

## 5.5 Further analysis

The results from the previous section show that SWASH (IDSB) under predicts (over predicts) IG-energies in region I (region II). To gain more insight in these deviations, the results are more extensively analyzed by focussing on the nearshore behaviour of the IG-waves (propagation and reflection) and on the magnitude of the incoming and reflected IG-waves. For this purpose two techniques are applied to analyze the measurements, IDSB results and SWASH results in further detail: the cross-correlation function and a signal decomposition technique. The cross-correlation technique and a signal decomposition technique were previously applied by *Janssen et al. (2003)* and *Battjes et al (2004)*, respectively, in the analysis of the *Boers (1996)* flume experiment.

The cross-correlation function is used to visualize the propagation and reflection of the IG-waves and therefore gives insight in the propagation properties of the incoming and reflected IG-waves.

The signal decomposition technique quantifies the magnitude of the incoming and reflected IG-wave, in this manner insight is gained in the growth of the incoming IG-waves, the dissipation in the surf-zone, the reflection at the shoreline and the magnitude of the outgoing IG-wave.

### 5.5.1 Cross-Correlation

#### Introduction

The cross-correlation function of two wave signals gives an indication how both signals compare and the wave signals are compared for a range of time shifts. The resulting cross-correlation  $R_{xy}(\tau)$  has a magnitude between -1 and 1, indicating how well both signals compare for a time shift  $\tau$ . For two identical signals the cross-correlation attains a value of 1 while for two identical signals that are out of phase a value of -1 is found. For a detailed description of the cross-correlation function, see Appendix B.

The cross-correlation function is applied to several combinations of wave signals. The following two signals are investigated: (i) the squared wave envelope  $A^2$  and (ii) the IG-surface elevation  $\zeta_{IG}$  ( $0.001 < f < 0.2\text{Hz}$ ).

The wave envelope (Appendix C) describes the amplitude variation on wave group scale ( $0 < f < 0.2\text{Hz}$ ) and is obtained using the short-wave surface elevation ( $0.2 < f < 1.5\text{H}$ ). The cross-correlation function is applicable to a random stationary process with a zero mean. The cross-correlation function is thereby not directly applicable to both wave signals, of which the mean is not equal to zero. To obtain a signal which fulfils this requirement, the mean trend of the signal is removed.

The following notation is used to make a distinction between the various cross-correlations:  $R_{xy}(\tau, x_i; x_j)$  denotes the cross-correlation between signal  $X(t)$  at location  $x_i$  and  $Y(t)$  at location  $x_j$ . The cross-correlation function is applied throughout the whole domain (all gauge locations).

In the following the subscript  $A_d$  denotes the detrended squared wave envelope and  $\zeta_d$  the detrended IG-surface elevation. For example:  $R_{A_d\zeta_d}(\tau, x_i; x_R)$  denotes the cross correlation between the  $A_d$  throughout the domain ( $x_i$ ) and  $\zeta_d$  at reference location  $x_R$ .

The cross correlation is investigated for the measurements, the SWASH results (baseline prediction: mixing length of 0.13m and a Manning coefficient of 0.03) and the IDSB results (baseline prediction: friction coefficient  $c_f$  of 0.03 and a wave breaking parameter  $\gamma$  of 0.5).

## Results

First, the cross-correlation function is applied to the wave envelope to get insight in the cross-shore behaviour of the wave groups. Since no short-wave surface elevation time series available for IDSB, the wave envelope cannot be determined. The cross-correlation of the wave envelope is therefore only investigated for the measurements and the SWASH results. Figure 5.19 shows the cross-correlation of the wave envelope throughout the domain and the wave envelope at the offshore boundary.

The results of the measurements and SWASH show similar results. A bar of strong correlation, with an increasing time shift in shoreward direction, is found that visualizes the wave groups propagating into the domain. The time shifts calculated for the group velocity corresponding to the peak frequency show to match with the pattern of strong correlation, indicating that the wave groups propagate with the group velocity. In region II the short waves start to break and the correlation decays, indicating a decay of the group structure of the incident waves. Close to the shore the correlation becomes negative. This indicates that the largest wave before breaking becomes the smallest wave after breaking, resulting in an inversion of the wave group signal.

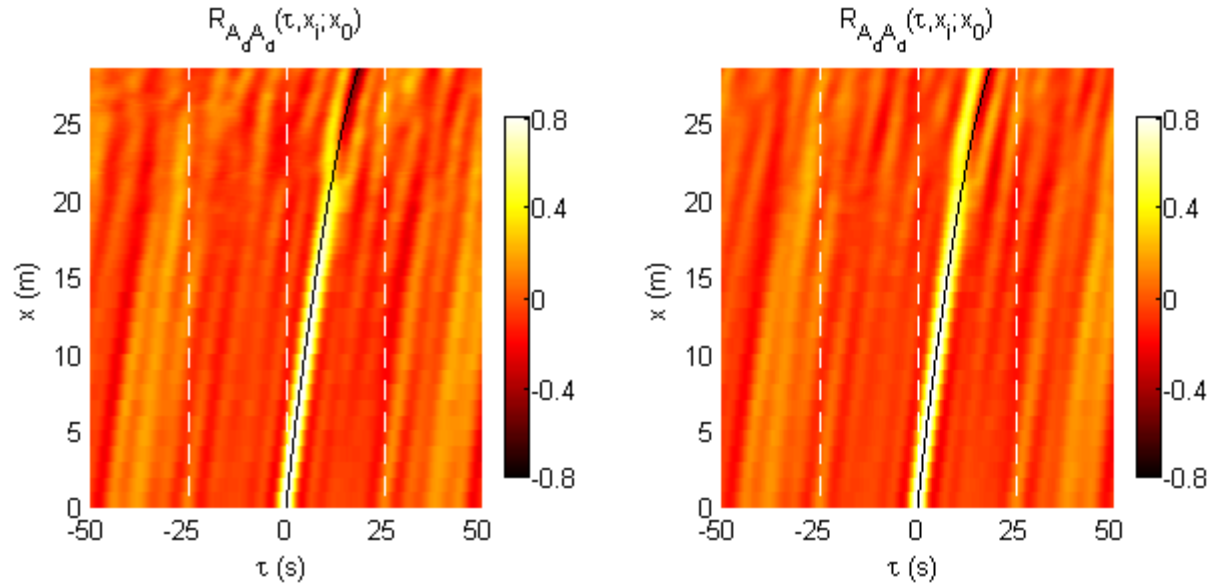


Figure 5.19: Cross-correlation function of the detrended squared wave envelope  $A_d$  throughout the domain  $x_i$  and at the offshore boundary  $x_r=0$ . The black line represents the time shift due to the group velocity according to the peak frequency. Left panel: Measurements; Right panel: SWASH.

The cross-correlation of the IG-signal throughout the domain and at the offshore boundary gives insight in the behaviour of the IG-waves throughout the domain and this is investigated for the measurements, the SWASH results and the IDSB results (Figure 5.20).

The results for the measurements show a V like pattern at positive and negative time shifts, previously observed by *Janssen et al. (2003)*. It is important to understand this pattern to be able to interpret the results. Here a short summary is given that explains the pattern, a detailed description of this pattern is given in Appendix B. The bars of positive correlation at positive time shifts (indicated by I and III) correspond to a correlation between the incoming signal throughout the domain ( $x_i$ ) and the incoming signal at the offshore boundary ( $x_r$ ). The bar indicated by III originates from the cross-correlation between the outgoing signal at  $x_i$  and the incoming signal at  $x_r$ . The bar indicated by I visualizes an incoming IG-wave propagating towards the shoreline and the bar indicated by III corresponds to a seaward propagating IG-wave. The bars of correlation at negative time shifts correspond to the same IG-components: II visualizes an incoming IG-wave while IV visualizes an outgoing IG-wave. The source of this correlation is however different, bar II is due to a correlation between the incoming signal at  $x_i$  and the reflected signal at  $x_r$  while bar IV corresponds to a correlation between the reflected signal at  $x_i$  and the reflected signal at  $x_r$ . Summarizing: the bars at positive time shifts originate from a correlation of the signal (incoming and outgoing) at  $x_i$  with the incoming signal at  $x_r$  and the bars at negative time shifts originate from a correlation of the signal (incoming and outgoing) at  $x_i$  with the outgoing signal at  $x_r$ .

The overall pattern visualizes an incoming IG-wave propagating in shoreward direction that is reflected at the shoreline and after reflection propagates in seaward direction. Comparing the pattern of the incoming and outgoing IG-wave with the time shifts for the group and phase velocity gives insight in the velocities of the IG-waves. The variation of the time shift of pattern I in shoreward direction is slightly smaller than the time shifts corresponding to the group velocity: the incoming IG-wave propagates with a velocity that is slightly smaller than the group velocity. The time shifts of the pattern associated with the reflected IG-wave (III) matches well with the phase velocity, indicating an outgoing IG-wave propagating with  $\sqrt{gh}$ .

The cross-correlation function for IDSB and SWASH show a band of strong positive correlation for a negative time shift, similar to results of the measurements. The SWASH results show no band of significant correlation for a positive time shift and for IDSB a pattern is visible, although this pattern is insignificant compared to the pattern at negative time shifts. The absence of a significant pattern at positive time shifts indicates that the incoming IG-wave at the offshore boundary is not correlated to the incoming IG-wave inside the domain. For SWASH this confirms the absence of an incoming bound IG-wave. IDSB does incorporate an incoming bound IG-wave and the absence of significant correlation between this incoming bound IG-wave and the incoming IG-wave inside the domain is surprising.

The pattern at negative time shifts, as reasoned before, originates from the correlation between the reflected signal at the offshore boundary and the signal (incoming and outgoing) throughout the domain. The pattern, for IDSB and SWASH, associated with the incoming IG-wave shows a growth of positive correlation in shoreward direction that becomes significant shoreward from  $x = 10m$ . The results of IDSB and SWASH further indicate that the IG-waves undergo similar behaviour as the measurements: an incoming IG-wave with a velocity slightly smaller than the group velocity and an outgoing IG-wave propagating with  $\sqrt{gh}$ .

A closer look at the IDSB results highlights an additional difference for the incoming IG-wave, the incoming IG-wave shows to have the greatest correlation at  $\tau \sim -25s$  while for the measurements and SWASH the greatest correlation is observed at a slightly smaller time shift ( $\tau \sim -24s$ ). A possible explanation for this difference is the reflection of the incoming IG-wave at the shoreline. The distance between the maximum correlation of the incoming and the reflected IG-wave at the most shoreward position ( $x = 28.5m$ ) is greater for IDSB than for SWASH and the measurements. This could be related to the difference of the numerical implementation of the reflection in IDSB and SWASH and how this implementation relates to reality.

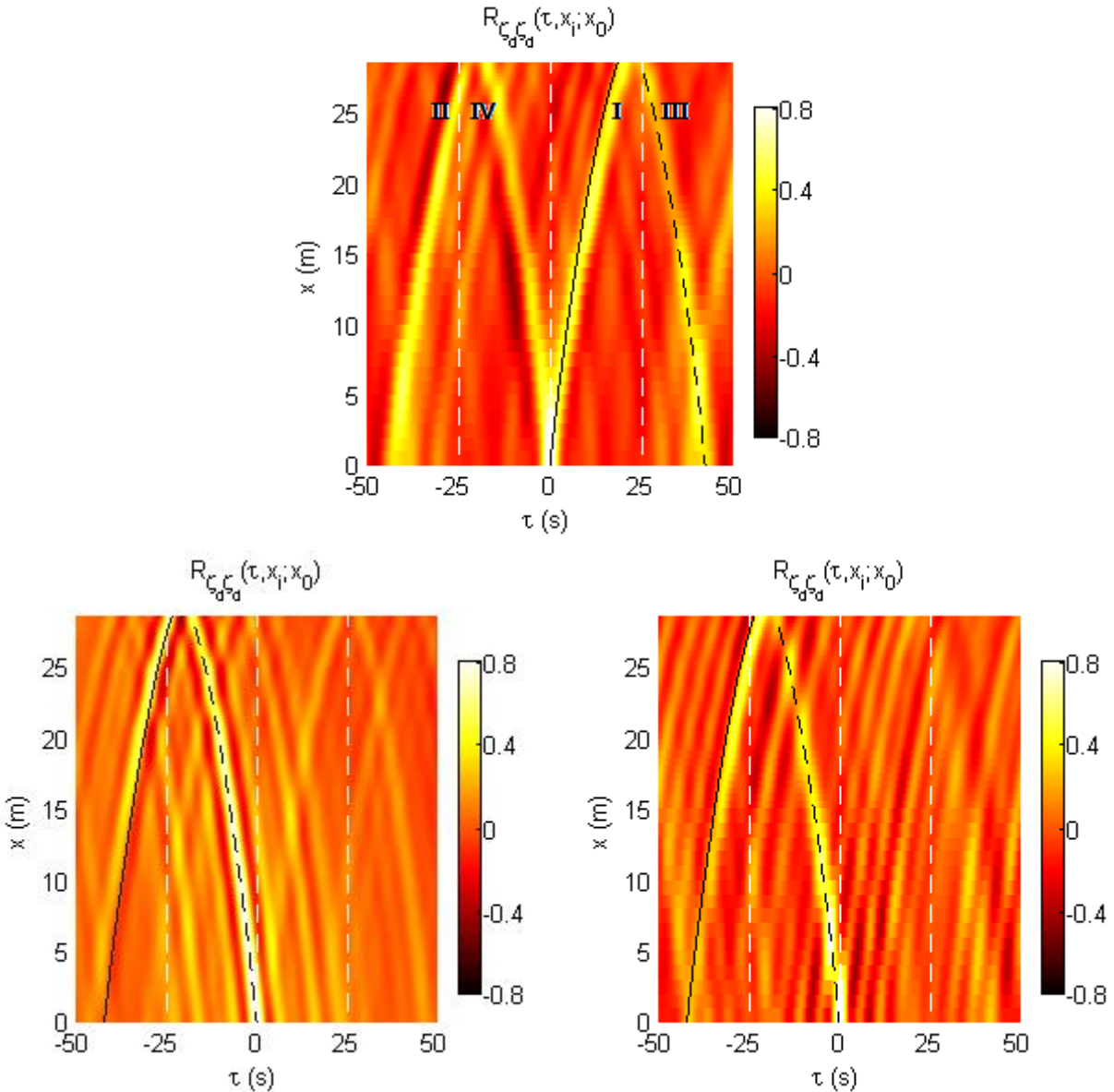


Figure 5.20: Cross-correlation function of the detrended IG-surface elevation  $\zeta_d$  throughout the domain  $x_i$  and at the offshore boundary  $x_i=0$ . The black line represents the time shift due to the group velocity according to the peak frequency, the dashed black line is the time shift for  $\sqrt{gh}$ . Upper panel: Measurements; Lower left panel: IDSB; Lower right panel: SWASH.

Cross-correlating the IG-surface elevation with the wave envelope (only applicable for the measurements and SWASH) gives more insight in the relation between the IG-waves and the forcing mechanism (Figure 5.21)

For the measurements a strong negative correlation is found between the IG-surface elevation and the wave envelope, in agreement with theory (Longuet-Higgins and Stewart, 1962). The results indicate that the IG-waves are generated due to the non-linear interactions of the short waves, in addition the patterns confirm the previous observed cross-shore behaviour of the IG-waves. From these results it can

be concluded that the incident IG-wave is in anti-phase with the forcing, similar to a bound IG-wave. This bound IG-wave is reflected at the shoreline and propagates in seaward direction with the phase velocity, indicating that reflected IG-wave propagates as a free IG-wave.

The SWASH results show an increasing band of negative correlation in cross-shore direction that becomes significant at  $x > 10m$ , similar to the observations in Figure 5.20, and this indicates that the incoming IG-wave is out of phase with the wave groups. For the reflected IG-wave, no clear band of negative correlation is found. Close inspection does show the presence of patches of negative correlation around the time shifts corresponding to the phase velocity (dashed white line), strengthening the believe that reflected IG-waves are present. Apart from the bands of negative correlation the SWASH results show a band of positive correlation at slightly smaller time shifts than the bands of negative correlation. The source of this band of positive correlation is unclear.

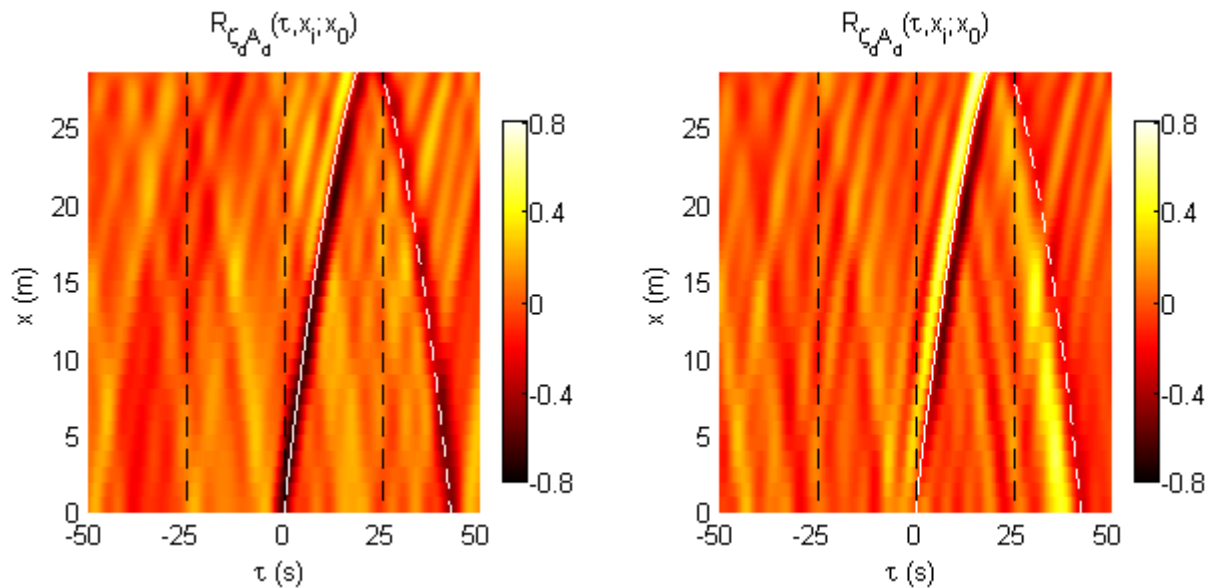


Figure 5.21: Cross-correlation function of the detrended IG-surface elevation  $\zeta_a$  throughout the domain  $x_i$  and the detrended squared wave envelope  $A_a$  at the offshore boundary  $x_r=0$ . The full white line starting at  $x = 0m, \tau = 0s$  represents the time shift due to the group velocity according to the peak frequency and the full white line starting at  $x = 28.5m, \tau = 25s$  represents the time shift due to the phase velocity. Left panel: Measurements; Right panel: SWASH.

## 5.5.2 Signal decomposition

### Introduction

In addition to the qualitative comparison by applying the cross-correlation function, a quantitative comparison between the measurements and the model results is made by separating the IG-wave signal in an incoming and outgoing component. The signal is decomposed using two methods, the 'array-method' and the 'collocated-method'. A detailed description of both techniques is given in Appendix A.

The array method decomposes the IG-signal in the frequency domain using the IG-surface elevation signal. With the collocated method the decomposition is carried out in the time domain, using the IG-surface elevation and IG-velocity signal at the same location (collocated sensor). In both methods the propagation velocities of the incoming and outgoing IG-waves must be defined. The velocity of the incoming IG-wave is chosen as the group velocity corresponding to the peak frequency and the velocity of the outgoing IG-wave is chosen as the phase velocity. The results of the cross-correlation technique showed an incoming IG-wave propagating with a velocity slightly smaller than the group velocity. It is assumed that errors due to this incorrect representation of the incoming IG-wave velocity are relatively small.

Both decomposition methods assume that an incoming bound IG-wave and a reflected free IG-wave contribute to the surface elevation signal. For the measurements and IDSB this seems to be a reasonable assumption as the boundary condition includes second order wave forcing. For SWASH, however, spurious free IG-waves might be generated as the wave forcing at the boundary is incomplete. The results of the cross-correlation showed no reason to believe that incoming free IG-waves are present and it is assumed that neglecting an incoming free IG-wave is allowable.

Comparing the results of both techniques for the SWASH results shows that both techniques results in similar magnitudes of the incoming and outgoing IG-wave height (Appendix E). Furthermore the cross-correlation technique is applied to the results of the collocated method and the results further strengthen the confidence in this decomposition technique. The collocated method is, however, only applicable to SWASH and in the following only the results obtained using the array method are discussed.

### Results

The results for IDSB (baseline prediction:  $c_f = 0.03$  and  $\gamma = 0.5$ ), SWASH (baseline prediction:  $l_m = 0.13m$  and  $m_n = 0.03$ ) and the measurements, using the array method, are shown in Figure 5.22.

The results of the measurements show an incoming and outgoing IG-wave height of  $\sim 0.01m$  at the offshore boundary. The incoming IG-wave height increases in shoreward direction, associated with shoaling and an energy transfer from the short waves towards the IG-waves. In region II the growth rate decreases and close to the shore the gradient becomes negative (a decay of IG-wave height). This is

associated with a decrease of the IG-forcing and an increased dominance of dissipation. In region II the pattern of the outgoing IG-wave is irregular, the same pattern is observed for the SWASH. This indicates that this pattern can be associated with noise in the decomposition method. Shoreward of region I the outgoing IG-wave height decreases in seaward direction. The gradient of the outgoing IG-wave height is smaller than the gradient observed for the incoming IG-wave height, this is associated with the absence of non-linear interactions between the short waves and the outgoing IG-wave: the outgoing IG-wave de-shoals in seaward direction.

The overall pattern of the incoming and outgoing IG-wave is captured in the SWASH results. The incoming IG-wave height increases in shoreward direction in region I, while the growth rate of the wave-height decays in region II. The incoming IG-wave height, however, is smaller near the offshore boundary. In shoreward direction the growth rate of the incoming IG-wave is greater than that observed in the results of the measurements. Both the difference in magnitude near the offshore boundary and the growth rate of the incoming IG-wave are associated with the absence of IG-waves forcing at the offshore boundary in SWASH. The incoming IG-wave, which is in equilibrium with the forcing and absent at the offshore boundary, is reasoned to be generated in the domain. This results in a greater gradient of the incoming IG-wave height observed in the SWASH results. The pattern of the reflected IG-wave is similar as the pattern observed for the measurements. The magnitude of the reflected IG-wave predicted by SWASH is, however, smaller. This is associated with an under prediction of the reflection or an over prediction of the dissipation in the surf zone.

At the offshore boundary, the IDSB predicted incoming IG-wave height is smaller than observed for the measurements. The growth rate of the incoming IG-wave is similar in region I, while in region II the growth rate is much greater than observed for the measurements. This deviation in region II is reasoned to originate from two possible sources: over prediction of the IG-wave forcing in the surf zone and an under prediction of the dissipation. Note: the dissipation mechanism incorporated in IDSB does not resemble a physical mechanism.

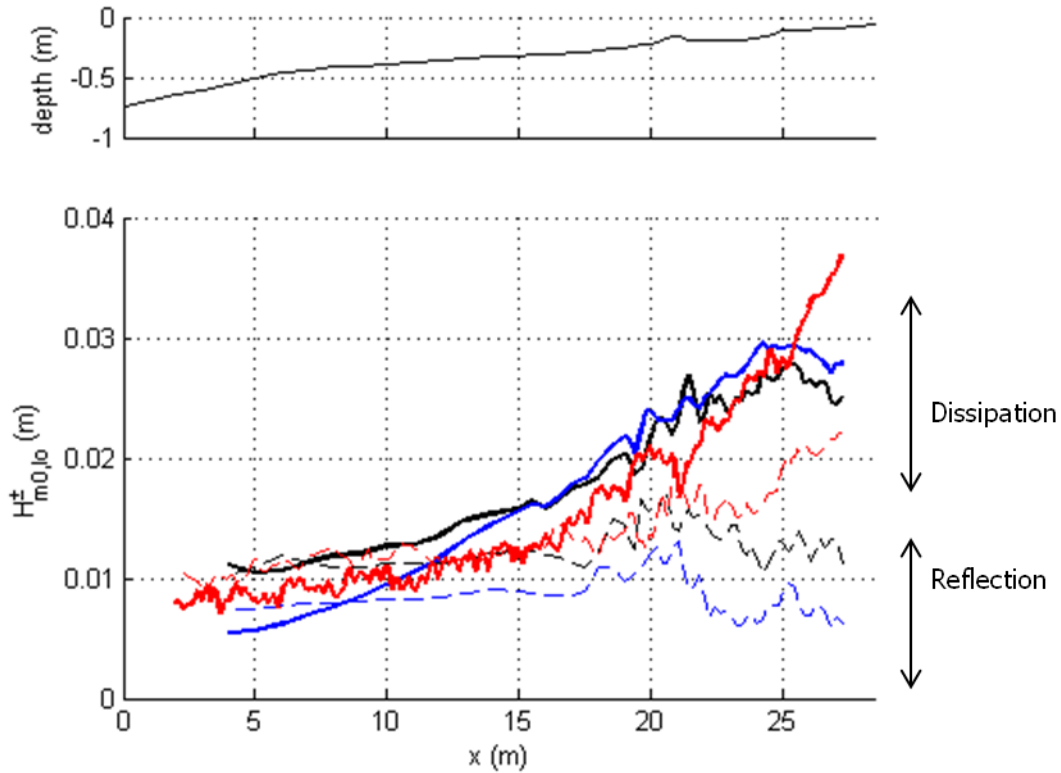


Figure 5.22: Signal decomposition with the array method for the measurements (black), IDSB (red) and SWASH (blue). Thick solid line: significant incoming IG-wave height, dashed line: significant outgoing IG-wave height.

The incoming and outgoing IG-wave height are separated into various frequency bands to make a distinction between relative short and long IG-waves (Figure 5.23 and Figure 5.24). The results for the frequencies bands at lower frequencies ( $0.04\text{Hz} < f < 0.06\text{Hz}$ ,  $0.06\text{Hz} < f < 0.08\text{Hz}$  and  $0.08\text{Hz} < f < 0.10\text{Hz}$ ) are irregular for both the incoming and outgoing IG-wave heights. The irregular pattern for the lower frequency bands makes it hard to interpret the results. For the higher frequencies the results, however, do give an indication of the behaviour and magnitude of the IG-wave heights.

For the measurements the results show that the growth rate of the incoming IG-wave is greater for higher frequencies, while the magnitude of the reflected IG-wave is greater for lower frequencies. This frequency dependent growth rate and reflection was previously observed by *Battjes et al. (2004)*.

The incoming and outgoing IG-wave height predicted by SWASH is very similar to the measured IG-wave heights (Figure 5.23). The results show that the frequency dependency is present in SWASH. Furthermore the results give insight in the differences between the model results and the measurements as observed in Figure 5.22: An incoming IG-wave is absent for all frequency bands and the magnitude of the outgoing IG-wave is under predicted for all frequency bands.

For IDSB the results show that the incoming IG-wave height is similar to the measurements at the higher frequencies, while for the lower frequencies a different pattern is observed (Figure 5.24). Furthermore, the results show that the reflected IG-wave height is over predicted throughout the domain at the higher frequency. This over prediction of the reflected IG-wave height confirms previous observations (*Reniers et al., 2010*) and it was reasoned that this over prediction is due to an incorrect modelling of the dissipation term: in IDSB the dissipation due to IG-wave breaking (*Van Dongeren et al., 2007*) and an energy transfer from the IG-waves to the short waves (*Thomson et al., 2006, Henderson et al., 2006*) is absent.

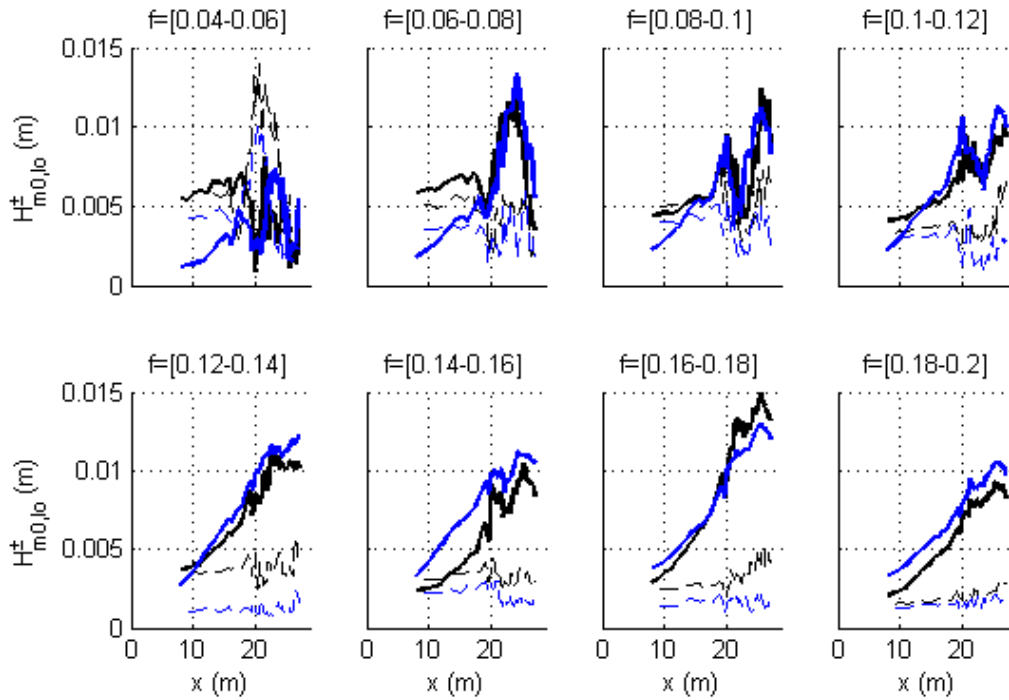


Figure 5.23: Incoming (thick solid line) and outgoing (dashed line) IG-component obtained with the array method for various frequency bands. Measurements (black) and SWASH, baseline prediction with a mixing length of 0.13m and a Manning coefficient of 0.03 (blue).

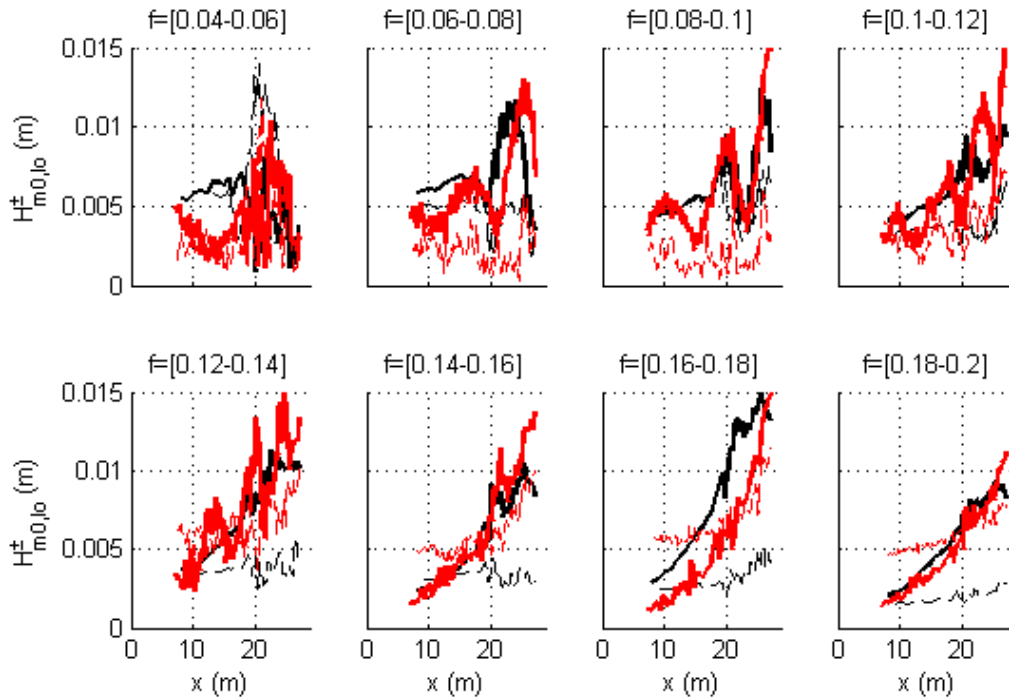


Figure 5.24: Incoming (thick solid line) and outgoing (dashed line) IG-component obtained with the array method for various frequency bands. Measurements (black) and IDSB results, baseline prediction with a friction coefficient  $c_f$  of 0.03 and a wave breaking parameter  $\gamma$  of 0.5 (red).

### 5.5.3 Extended domain

In the previous analysis it appeared that the absence of IG-wave forcing is one of the contributing factors to the under prediction by SWASH in the offshore region (region I). In this section several new simulations are carried out with an extended profile. The extended profile allows SWASH to generate the incoming IG-wave in the extended domain, thereby mimicking the incoming bound IG-waves generated by the second order wave forcing in the flume experiment.

#### Model setup

The domain is extended with two profiles; a gradual slope (Table 5.6) and a constant depth (Table 5.7). The simulations are run with one vertical layer and the application of a turbulence model (Prandtl mixing length hypothesis). The mixing length and Manning coefficient are chosen similar to the values used in the baseline prediction.

*Table 5.6: Extended simulations with a gradual slope.*

Simulation ID	# vertical layers (-)	$n_m$ (-)	$I_m$ (m)	Max depth (m)	Extended length (m)
1V_e1	1	0.03	0.13	1.5	15
1V_e2	1	0.03	0.13	3	45

*Table 5.7: Extended simulations with a constant depth.*

Simulation ID	# vertical layers (-)	$n_m$ (-)	$I_m$ (m)	Extended length (m)
1V_L1	1	0.03	0.13	15
1V_L2	1	0.03	0.13	30
1V_L3	1	0.03	0.13	60

Extending the domain with a gradual slope introduces an error as the wave forcing, initially forced at 0.75m depth, is applied at greater depths. The significant short-wave height is not significantly changed (not shown) but the spectral shape is distorted: the spectral peak increases in magnitude for greater maximum depths while less energy is present at the higher frequencies (Figure 5.25). For a domain extension with uniform depth this is not observed and the overall spectral shape remains similar (Figure 5.26), the energy of the short waves is, however, lower for an increasing domain width, associated with additional damping in the extended domain by the turbulence model.

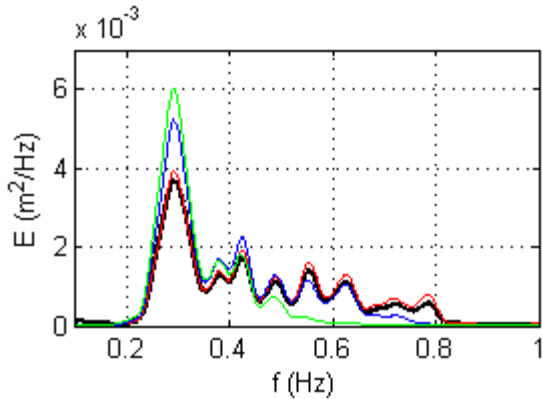


Figure 5.25: Spectral density at  $x=0m$  for the extended domain simulations with a gradual slope. Measurements (black), SWASH results for a maximum depth of  $0.75m$  (red)  $1.5m$  (blue) and  $3m$  (green).

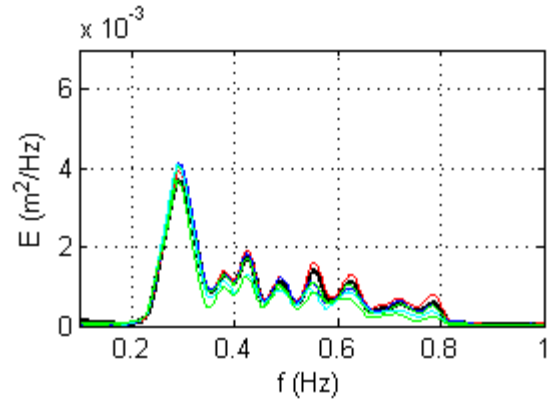


Figure 5.26: Spectral density at  $x=0m$  for the extended domain with a uniform depth. Measurements (black), SWASH results for an extension of  $0m$  (red),  $15m$  (blue),  $30m$  (green), and  $60m$  (cyan) respectively

## Results

The results are investigated for the incoming and outgoing IG-wave respectively, obtained with the collocated method.

The domain extension with a gradual slope shows that for an increasing maximum depth the magnitude of the incoming IG-wave height increases while the magnitude of the outgoing IG-wave is not affected (Figure 5.27). The gradient of the IG-wave height between  $-40m < x < -20m$  (for the simulation with a maximum depth of  $3m$ ) is approximately constant, indicating that no IG-waves of significant magnitude are forced at depths greater than  $\sim 2m$ .

The results for a domain extension with a horizontal bottom profile are shown in Figure 5.28. For increasing domain lengths the incoming IG-wave height increases. However, this increase of the incoming IG-wave height is not converging for increasing domain lengths. This non-convergent behaviour is in contradiction with the notion of an equilibrium bound wave: for a constant wave forcing over a horizontal bed a bound IG-wave will develop that is in equilibrium with the wave forcing (provided the domain is sufficiently long for the equilibrium to develop). At the shoreward edge of region I ( $x \approx 20m$ ) the incoming IG-wave height is, however, of similar magnitude, independent of the extended length. Apparently an equilibrium is reached at  $x \approx 20m$ . It remains unclear how and to what extent an equilibrium incoming IG-wave is formed inside the domain.

The reflected IG-wave, similar to the observations for a domain extension with a gradual slope, is not significantly affected in the original domain ( $x \geq 0m$ ).

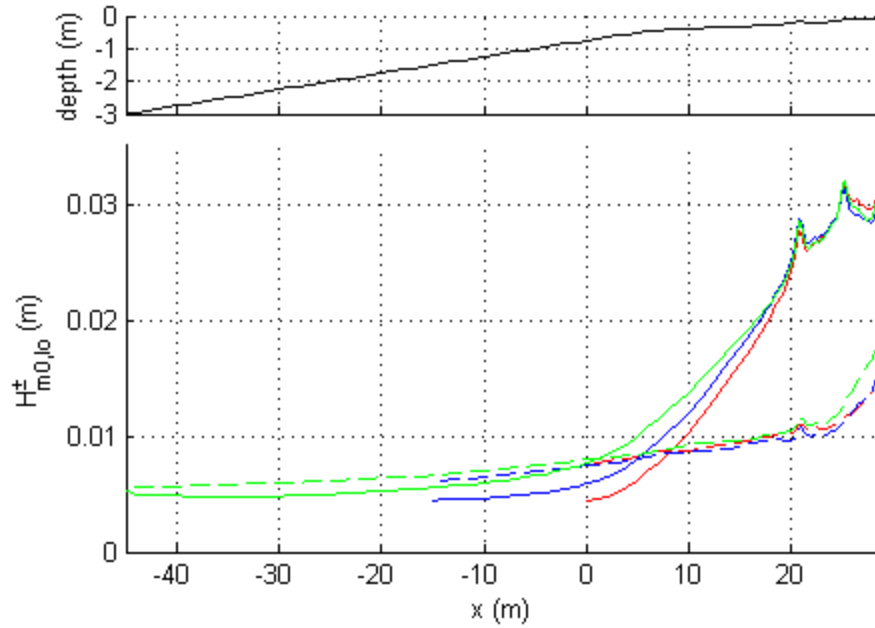


Figure 5.27: IG-Wave transformation for wave condition 1C, extended domain results for a gradual slope. IG-components obtained with the collocated method for the SWASH results: baseline prediction (red); a maximum depth of 1.5m (blue) and of 3m (green). (a) Bottom profile (b) in- (solid) and outgoing (dashed) significant IG-wave height.

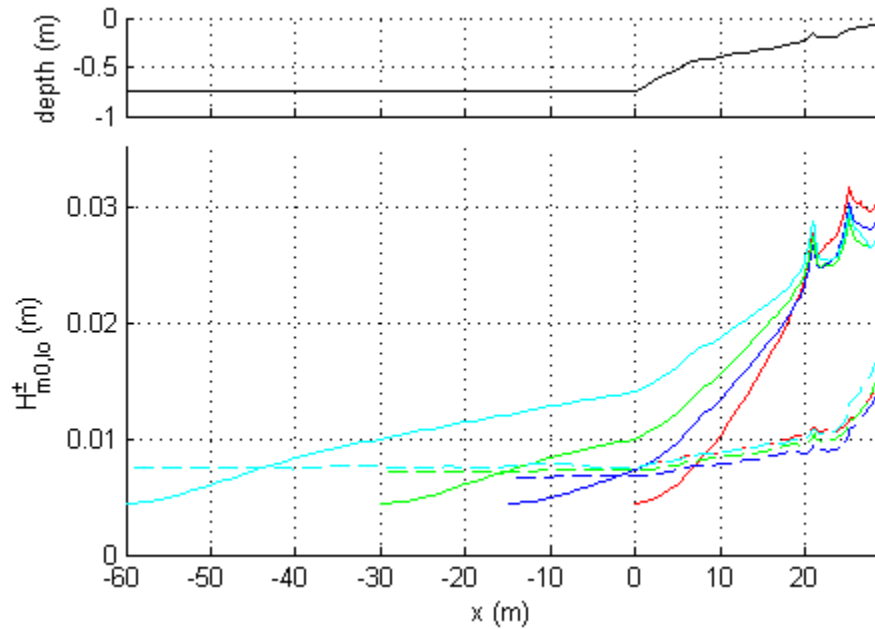


Figure 5.28: IG-Wave transformation for wave condition 1C, extended domain results for a uniform depth. IG-components obtained with the collocated method for the SWASH results: for the baseline prediction (red); a domain extension of 15m (blue); 30m (green); and 60m (cyan). (a) Bottom profile (b) In- (solid) and outgoing (dashed) significant IG-wave height.

## 6 Field case, FRF

---

### 6.1 Introduction

The aim of this chapter is to investigate the capabilities of the numerical models in predicting the IG-wave heights at a specific site in a nearshore region. To gain insight in the accuracy of the model predictions the predicted IG-wave height is compared with field measurements. Due to time constraints no assessment of SWASH is made.

The data used in this Chapter is obtained at the Field Research Facility (FRF) of the US Army Corps of Engineers. The FRF facility is located on the east coast of the United States of America in the city of Duck, North Carolina (Figure 6.1). The coast in this area is characterized by broad sandy beaches with a mild slope and a barred surf zone. The beach is subject to a semi diurnal tide with a range of 1m. The wave climate is characterised by locally generated wind waves and swell waves originating from the Atlantic Ocean.

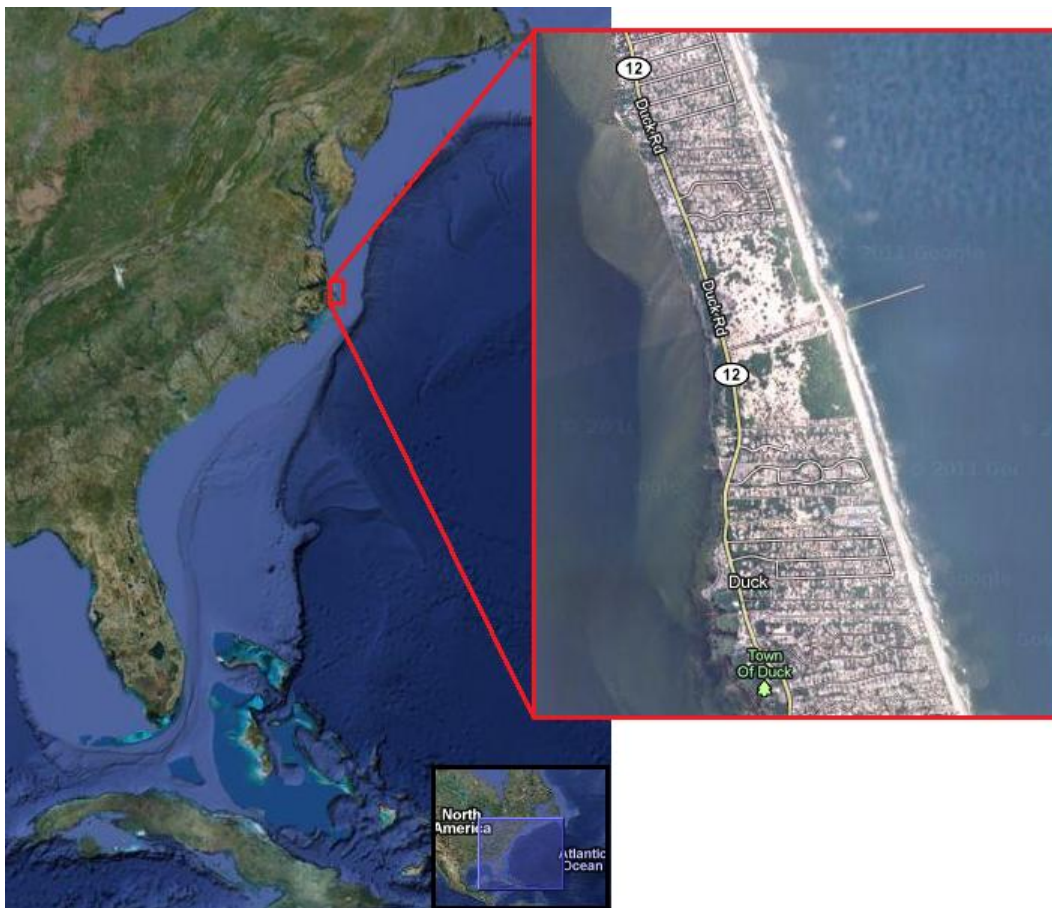


Figure 6.1: Location of the town of Duck (source: google maps)

## 6.2 Data description

Figure 6.2 shows a plan view and a cross-section of the beach profile at the FRF facility (including the location of the measurement devices), which is obtained during a survey conducted at 28-07-2010. The nearshore bathymetry is characterized by a fairly uniform alongshore profile, an average slope of approximately 1:100 and a barred surf zone. In general an outer bar is present at roughly 4.5m water depth and an inner bar at water depths ranging between 1m and 2m.

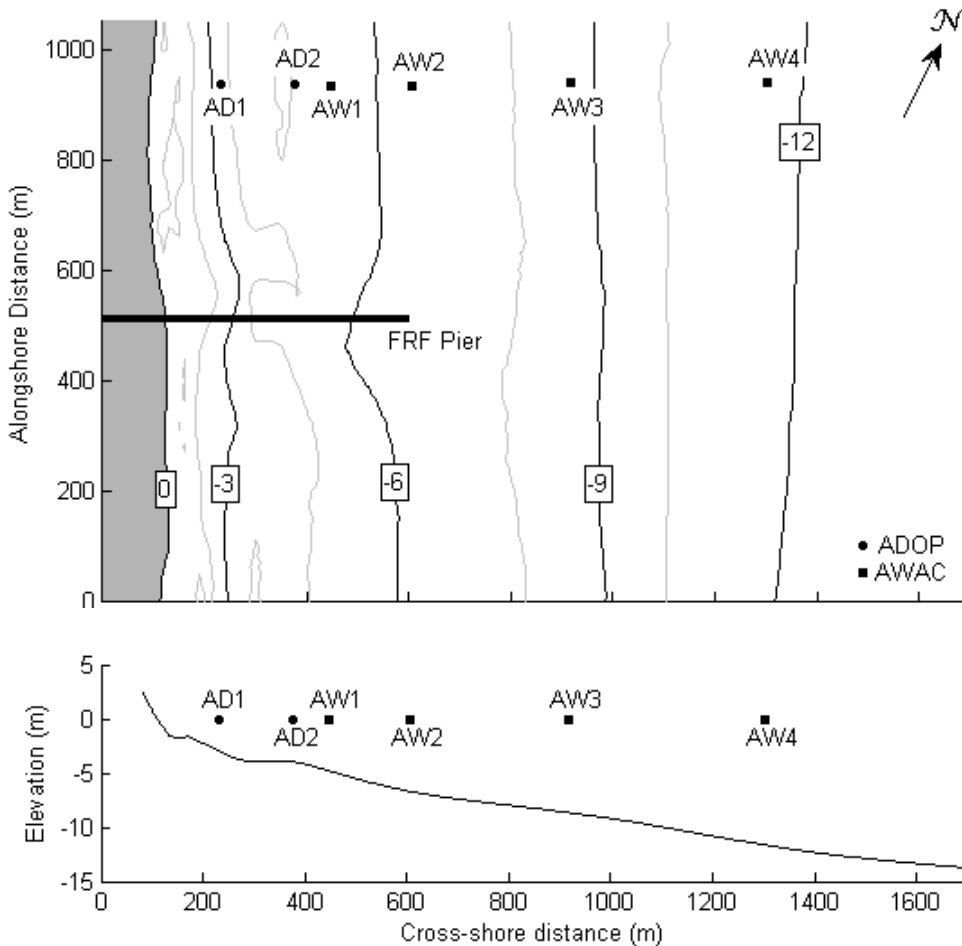


Figure 6.2: Duck bathymetry. Upper panel: Plan view of bathymetry and measurement gauges. Bottom panel: cross-shore profile obtained at the cross-shore transect of the measurement gauges. The depths are relative to NAVD.

### Instrumentation

In the nearshore region two types of measurement devices are deployed (Figure 6.2) Aquadopp (ADOP) and AWAC, which are capable of measuring the wave conditions. These devices measure the local velocities and pressures during a period of 34min with a sampling rate of 2Hz. The resulting velocity and pressure records consist of 4096 samples and are translated into frequency-directional spectra using

linear wave theory and 13 half overlapping Hanning windows. The calculated frequency-directional spectra have a frequency resolution of 0.01Hz and a directional resolution of 2°.

This sample length of the velocity and pressure records (2048s) is considered sufficient to accurately estimate the short-wave conditions. Due to the long periods of the IG-waves (typical periods of 20s – 200s), a sample length of 2048s seems to be relatively short to accurately estimate the IG-wave height. To obtain insight in the accuracy of the IG-wave height measurements, the influence of the sample length on the spectral densities is investigated by analyzing a record with a total length of 2h16min (Appendix F). The results show that the sample length influences the spectral densities, however, a sample length of 35min allows for an estimation of the energy densities at the IG-frequencies and the significant IG-wave heights.

In addition to the wave data, tidal elevations are obtained from the tide gauge (operated by NOAA) located at the end of the FRF pier (Figure 6.2).

### **Wave measurements**

In this study three data sets are considered. Each of the three set contains 2 days of wave measurements whereby the measurements started at 22-08-2009, 26-03-2009 and 29-08-2010. Each data set is considered as a separate case and in the following the cases are identified by E2, E6 and E8 (in the same order as the start dates).

Figure 6.3-Figure 6.5 shows the measured wave conditions and tidal elevations for each case at the most offshore located wave gauge (AW4). Note that the wave directions are relative to the shore normal, whereby the positive axis is taken in southern direction and the negative axis in northern direction.

Case E2<sup>4</sup> and case E6 show the arrival of energetic swell waves with a maximum significant wave height of roughly 3.6m. The main difference between both cases is the direction of the short waves. For case E2 the incident wave direction is fairly constant in time with an average incident peak angle of 30° and an average mean incident angle of 45°. For case E6, the mean direction is fairly constant at 35° while the peak period varies significantly around a mean value of 7°. In contrast with these energetic wave conditions, case E8 represents mild swell conditions whereby the significant wave height (~1.8m), mean direction (~46°) and peak direction (~27°) are fairly constant in time.

Note: measurements at the ADOP gauges are only available for case E8.

---

<sup>4</sup> Case E2 corresponds to the arrival of waves generated by Hurricane Bill in the Atlantic Ocean.

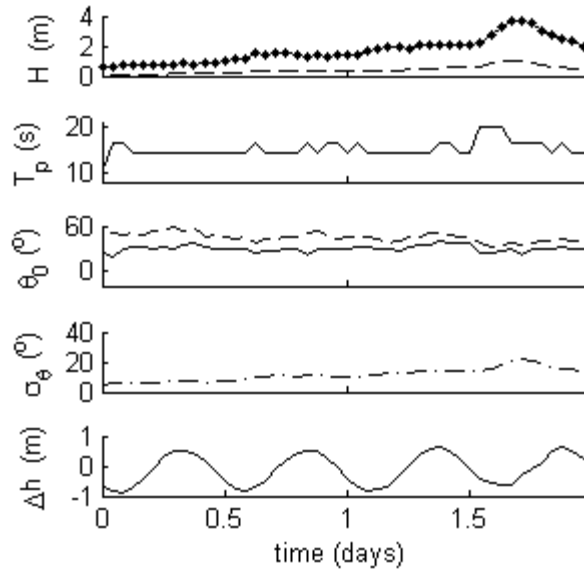


Figure 6.3: Wave conditions for case E2. From top to bottom: significant short-wave height (solid line) and IG-wave height (dashed line); peak period; peak- (solid line) and mean- (dashed line) direction; directional width; tidal elevation.

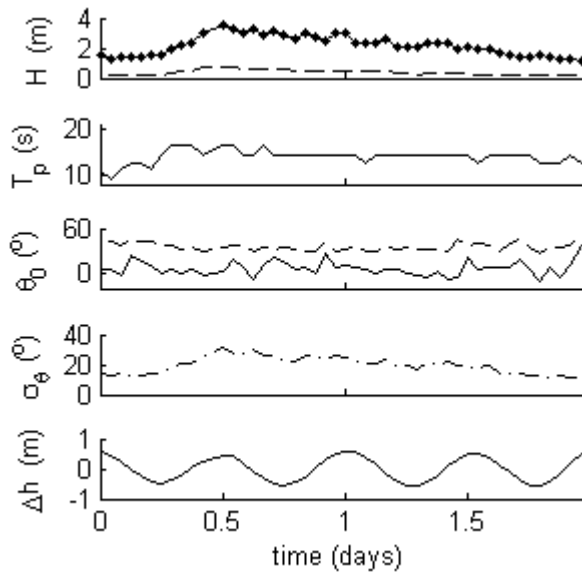


Figure 6.4: Wave conditions for case E6. From top to bottom: significant short- (solid line) and IG-wave height (dashed line); peak period; peak- (solid line) and mean- (dashed line) direction; directional width; tidal elevation.

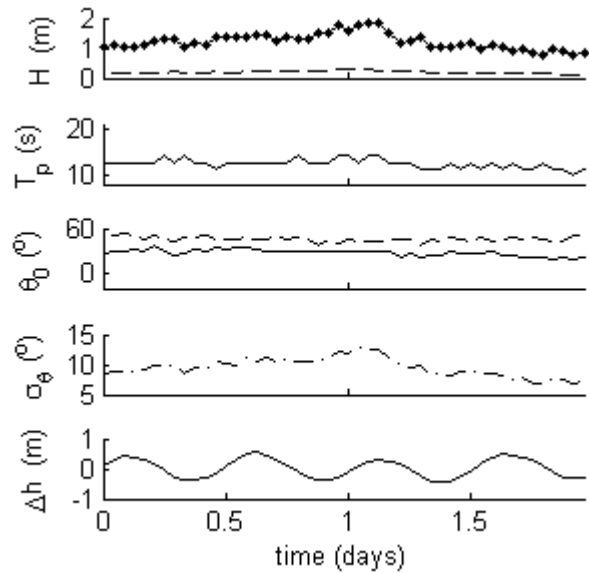


Figure 6.5: Wave conditions for case E8. From top to bottom: significant short- (solid line) and IG-wave height (dashed line); peak period; peak- (solid line) and mean- (dashed line) direction; directional width; tidal elevation.

### 6.3 Model setup

IDSB is applied to estimate the IG-wave height at the various gauge locations, based on the frequency-directional spectra measured at the most offshore located wave gauge (AW4). As frequency-directional spectra are available every hour this results in a total of 48 simulations per case whereby each simulation corresponds to 34 min of wave conditions.

IDSB is setup in such manner that the model only requires tuning for the friction coefficient. The wave breaking parameter is calculated using equation (3.32) (*Battjes and Stive, 1985*), in which the deep water wave steepness is estimated using the measurements at the gauge AW4 (significant short-wave height and peak period). The mean and the standard deviation of the resulting wave breaking parameter are shown in Table 6.1 for each case. The additional IDSB parameters are set at similar values as in previous studies (Table 6.2).

*Table 6.1: Wave breaking parameter for the Duck cases*

Case	E2	E6	E8
Mean $\gamma$ (-)	0.49	0.52	0.47
Standard deviation $\gamma$ (-)	0.04	0.03	0.01

*Table 6.2: Additional IDSB parameters*

$\beta$	$\alpha$	ndis	$e_{trsh}$
0.05	1	5	0.03

The friction coefficient is tuned separately for each case: a representative severe and mild condition is chosen and for these two conditions the optimal friction coefficient is determined. The results showed that, for all cases, a friction coefficient of 0.009 is optimal for both the severe and mild condition. The friction coefficient is therefore set at 0.009 for all simulations, which is a slightly greater value than the friction coefficient used in previous studies (*Reniers et al., 2002, Bijl et al., 2009, Reniers et al., 2010*) that employed a friction coefficient of 0.007.

With the above described model setup the IDSB parameters are fixed at the same values during all 48 simulations of each of the three cases.

## 6.4 Results

A comparison between the IDSB results and the measurements is made using the spectral densities and the integral wave heights. The cut-off frequency (defining the higher limit of the IG-frequencies and the lower limit of the short-wave frequencies) is chosen based on the spectral results. The cut-off frequency varies for the cases and is shown per case in Table 6.3. For all cases the upper frequency limit of the short waves is set at 0.5Hz and the lower frequency limit of the IG-waves is set at 0.01Hz to disregard the mean surface elevation.

Table 6.3: Cut-off frequency, short-wave frequencies and IG-wave frequencies for the three cases.

Case	E2	E6	E8
$f_c$ (Hz)	0.04	0.03	0.03

### 6.4.1 Short waves

First the results of the short-wave heights will be discussed in detail as this provides the forcing mechanism of the IG-waves.

Figure 6.6 shows a typical example of the cross-shore variation of the short-wave height during case E8 (corresponding to the wave conditions after 1 day and 3 hours of measurements). This specific simulation corresponds to an incoming significant wave height of 1.7m, a peak period of 14s and a peak direction of  $30^\circ$  (waves incident from the south-east). Going in shoreward direction, the measured short-wave height first decreases and slightly increases shoreward from  $x \sim 700m$ . No significant energy decay is present and this indicates that all gauges are located outside the surf zone. IDSB predicts increasing short-wave heights towards the shore and wave breaking at the inner bar and near the shoreline.

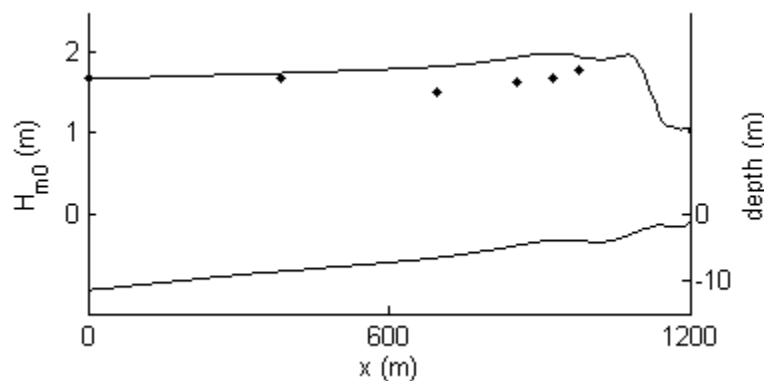


Figure 6.6: Cross-shore variation of the significant short wave height corresponding to a typical example for case E8. Measurements (black markers) and IDSB results (black line).

Plotting the measured short-wave heights versus the predicted short-wave heights per case for all 48 simulations shows that, in general, the results are within the region confined by the 20% error bands

(Figure 6.7-Figure 6.9). For case E2 and E8 the results are scattered around the line of perfect agreement, while for case E6 the results tend to be located above the line of perfect agreement, which suggests that IDSB generally over predict the short-wave height for case E6. Additionally the results show that for all cases IDSB tends to over predict the short-wave heights for more energetic conditions (roughly  $H_{m0,m} > 1.5m$ ).

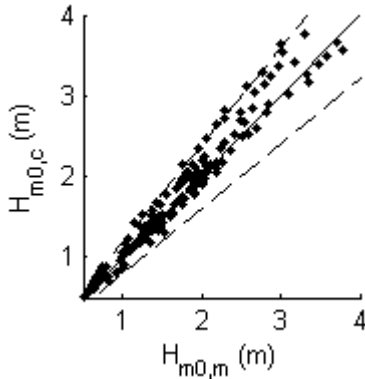


Figure 6.7: Measured versus computed significant wave height for case E2. 20% error bands are indicated by the dashed lines.

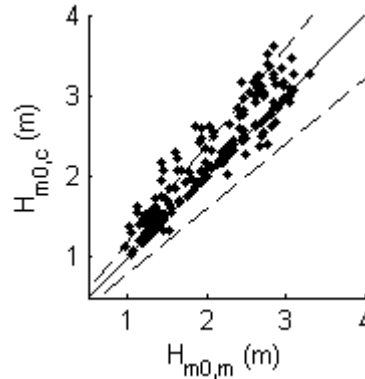


Figure 6.8: Measured versus computed significant wave height for case E6. 20% error bands are indicated by the dashed lines.

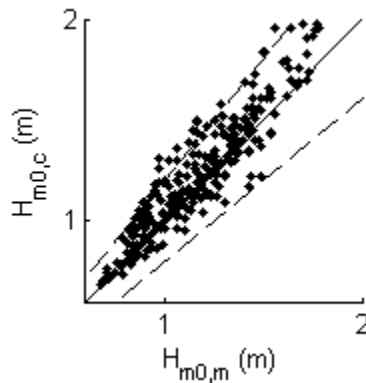


Figure 6.9: Measured versus computed significant wave height for case E8. 20% error bands are indicated by the dashed lines.

#### 6.4.2 IG-waves

First the spectral densities and the cross-shore variation of the integral wave height are investigated in more detail. Figure 6.10 shows the measured and computed energy densities at the IG-frequencies for the same typical example of case E8 as in Figure 6.6. The measured spectra show to be relatively broad at the wave gauges seaward of the outer bar (AW4, AW3, AW2 and AW1) while shoreward of the outer bar (AD2 and AD2) the shape becomes more structured with a distinct peak at 0.02Hz. In shoreward direction, the overall energy level increases and this increase predominantly occurs at lower frequencies ( $0.01Hz < f < 0.03Hz$ ). Overall the predicted spectrum by IDSB (corresponding solely to IG-waves) is

broad at the offshore boundary and shoreward of gauge AW3 a distinct peak at 0.02Hz develops. This peak becomes more pronounced in shoreward directions as the energies at the lower frequencies ( $0.01\text{Hz} < f < 0.03\text{Hz}$ ) increases. The energies in  $0.01\text{Hz} < f < 0.04\text{Hz}$  are consistently over estimated by IDSB and this over estimation can be as much as a factor 2 (e.g. for gauge AW1 at  $f = 0.02$ ).

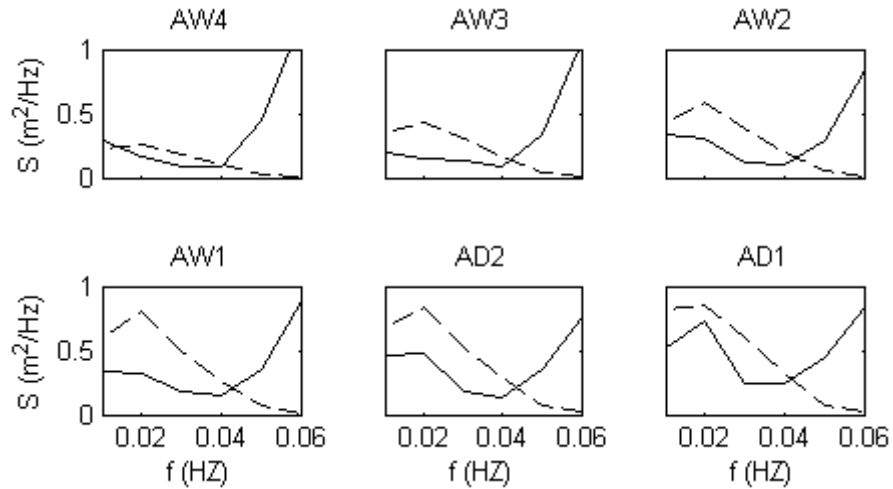


Figure 6.10: Energy density spectra ( $\text{m}^2/\text{Hz}$ ) for the example simulation of case E8. IDSB (dashed line) and measured (solid line)

Integration of the spectral densities over the IG-frequencies results in an estimation of the significant IG-wave height. Figure 6.11 shows the cross-shore variation of the measured and predicted IG-wave height. The measured IG-wave height increases in shoreward direction and this increase is greatest at the most shoreward located gauges (AD2 and AD1). Overall, the model results show a similar pattern although the predicted IG-wave height is generally greater than the measured IG-wave height. Inside the surf zone (where no gauges are available) the predicted IG-wave height increases significantly, similar to the observations in Chapter 4 and 5.

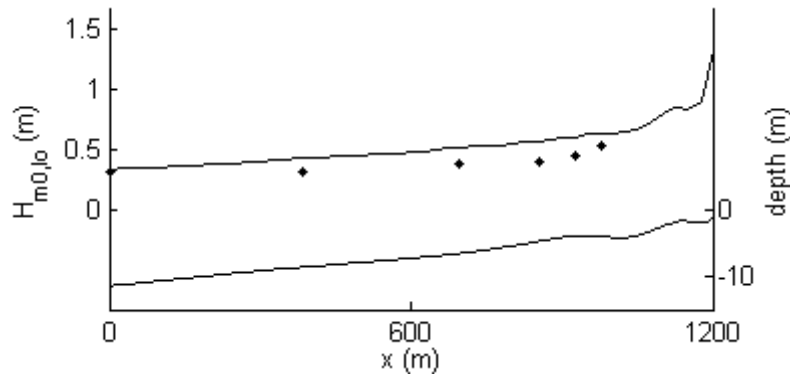


Figure 6.11: Cross-shore variation of the significant IG-wave height corresponding to a typical example for case E8. Measurements (black markers) and IDSB results (black line).

Next the computed and measured spectral densities are compared throughout the two day period of case E8.

At the offshore boundary (AW4) the energy distribution over the frequencies is broad during the whole case (Figure 6.12). The overall energies increase in time as the short-wave conditions become more energetic and subsequently decrease as the short-wave heights decrease after roughly 1.25 days. The predicted energy densities show to have a relative broad form during mild conditions while during more energetic conditions a peak develops at 0.02Hz (as observed in Figure 6.10).

The integral wave heights over the IG-frequencies are shown in the lower panel of Figure 6.12. Overall the predicted and measured IG-wave heights are of similar order of magnitude during the whole case. The predictions show an increase of the IG-wave height during more energetic short-wave conditions and a subsequent decrease as the short-wave conditions become milder.

The predicted bound IG-wave height shows to increase for more energetic conditions and its contribution to the total predicted IG-wave height varies between 8% for mild conditions to 18% during more severe conditions. No estimation of the bound IG-wave height is made for the measurements (which could be obtained by a bispectral analysis of the measurements), however, for similar wave conditions at similar depths, *Reniers et al. (2002)* showed a good correspondence between the computed and measured bound IG-wave. It is therefore expected that the predicted bound IG-wave height gives an accurate estimation of the bound IG-wave height.

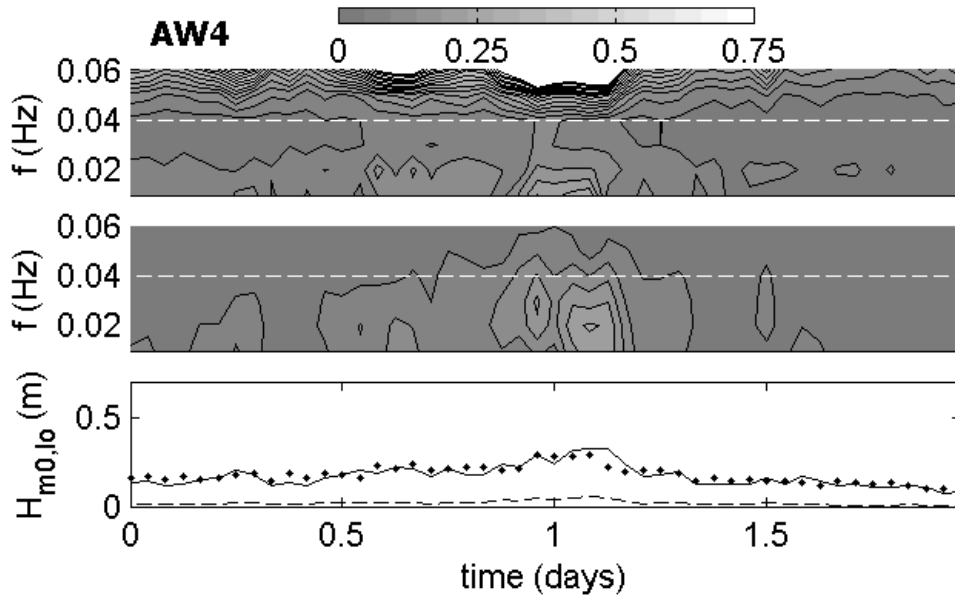


Figure 6.12: Overview of the measured and computed energy densities and significant IG-wave height for case E8 at AW4. Upper panel: measured surface elevation energy densities ( $m^2/Hz$ ), middle panel: computed surface elevation energy densities ( $m^2/Hz$ ), lower panel: predicted significant IG-wave height (solid line); measured significant IG-wave height (markers) and the predicted significant bound IG-wave height (dashed line). The white-dashed line in the spectral densities plots indicates the cut-off frequency.

At gauge AW1 (located at a depth of roughly 5.2m, seaward of the outer bar) the overall measured energy densities have significantly increased compared to AW4 (Figure 6.13). For more energetic conditions the measured spectra have become more structured with a peak at roughly 0.02Hz. Overall this is captured in the IDSB predicted spectra. The integral wave heights, however, show that IDSB generally predicts larger IG-wave heights compared to the measurements, which is most apparent after 1 day and 2 hours of measurements. Furthermore the predicted IG-wave height is greater than the measurements during first hours of the case and the last hours of the case.

At the most shoreward wave gauge (AD1), which is located seaward of the inner bar at a depth of roughly 3.5m, the energies further increase and the structure of the spectra becomes more pronounced (Figure 6.14). The measured spectra show a distinct peak at 0.02Hz during most of the case, in contrast, the predicted spectra do no longer show a distinct peak at 0.02Hz as the energies at 0.01Hz increased significantly.

The predicted IG-wave height shows a similar pattern as observed at AW1: the IG-wave height is over predicted in the first hours of the case; after roughly 1 day and after roughly 1.5 days.

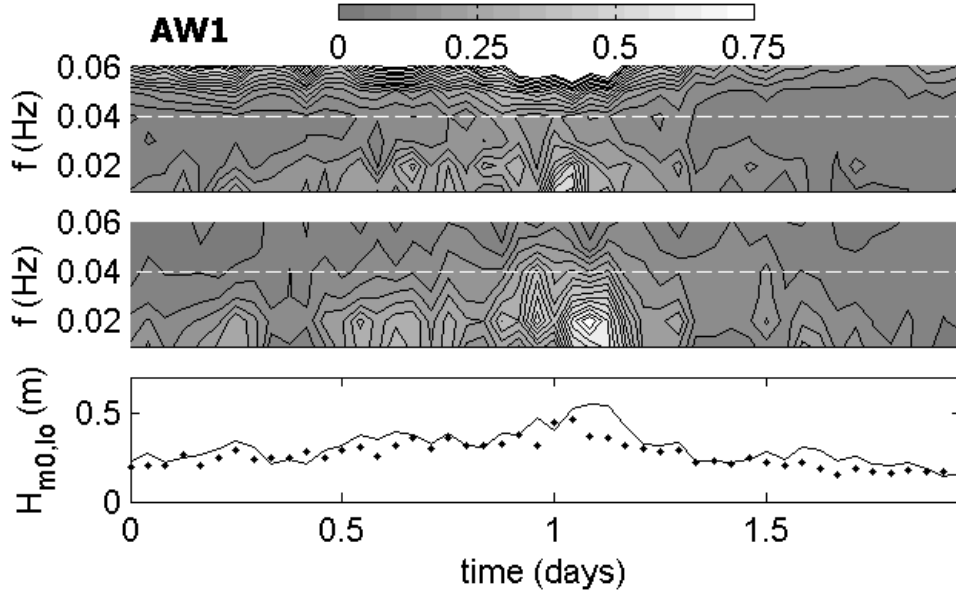


Figure 6.13: Overview of the measured and predicted energy densities and significant IG-wave height for case E8 at AW1. Upper panel: measured surface elevation energy densities ( $m^2/Hz$ ), middle panel: predicted surface elevation energy densities ( $m^2/Hz$ ), lower panel: predicted (solid line) and measured (markers) significant IG-wave height. The white-dashed line in the spectral densities plots indicates the cut-off frequency.

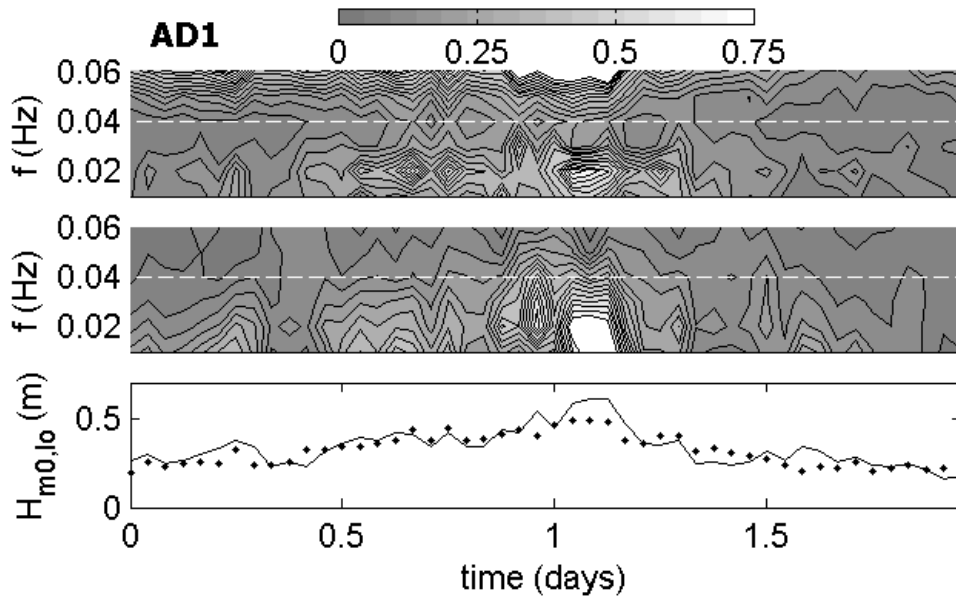


Figure 6.14: Overview of the measured and predicted energy densities and significant IG-wave height for case E8 at AD1. Upper panel: measured surface elevation energy densities ( $m^2/Hz$ ), middle panel: predicted surface elevation energy densities ( $m^2/Hz$ ), lower panel: predicted (solid line) and measured (markers) significant IG-wave height. The white-dashed line in the spectral densities plots indicates the cut-off frequency.

Plotting the measured versus the predicted IG-wave height for all simulations of case E8 gives insight in the magnitude of the difference between the measurements and the predictions (Figure 6.16). It shows that most of the results are located inside the region confined by the 20% error bands and the predictions match the measurements with reasonable accuracy. In general the scatter of the results increases in shoreward direction and the IG-wave height is increasingly over predicted for greater IG-wave heights.

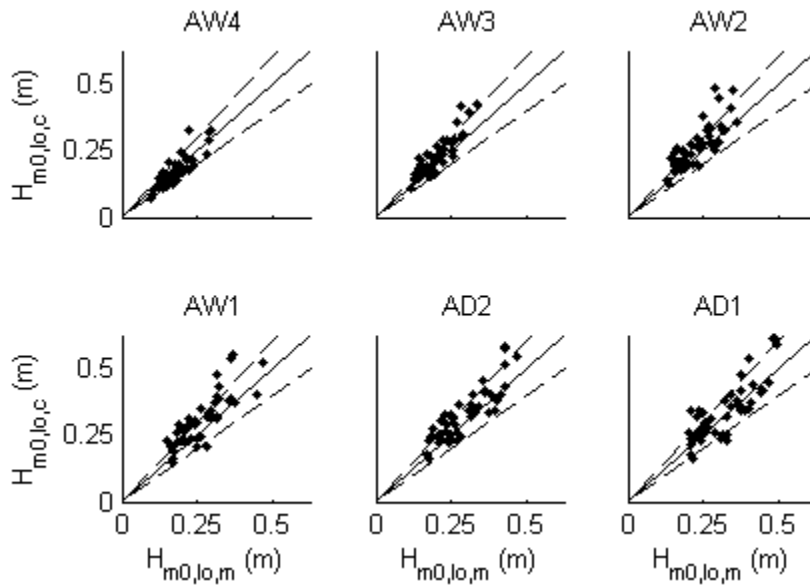


Figure 6.15 Measured  $H_{m0,lo,m}$  versus predicted  $H_{m0,lo,c}$  for case E8, from offshore (upper left) to nearshore (lower right). 20% error bands are indicated by the dashed lines.

For case E2 similar results are obtained (Figure 6.16). At the offshore boundary the predicted and predicted IG-wave height compare reasonable as most results are located in the region confined by the 20% error bands. In shoreward direction the scatter in the results increases and generally the predicted IG-wave height is greater for more energetic conditions.

In contrast with case E2 and E8, the results for case E6 show the tendency of IDSB to under predict the IG-wave height for increasing energetic conditions (Figure 6.17), which is most apparent at gauge AW3 and AW2.

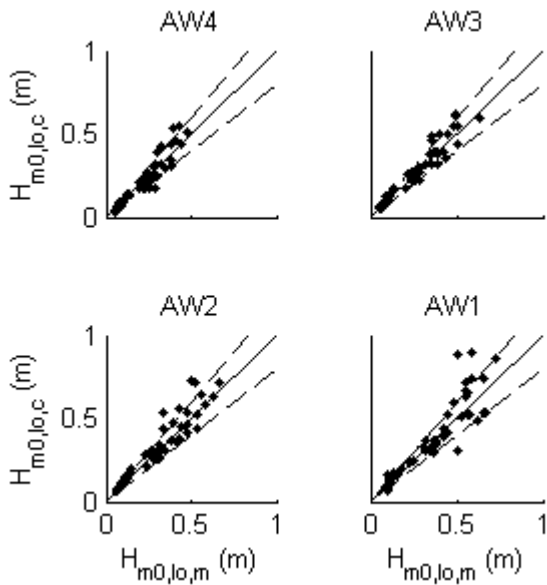


Figure 6.16 Measured  $H_{m0,lo,m}$  versus predicted  $H_{m0,lo,c}$  for case E2, from offshore (upper left) to nearshore (lower right). 20% error bands are indicated by the dashed lines.

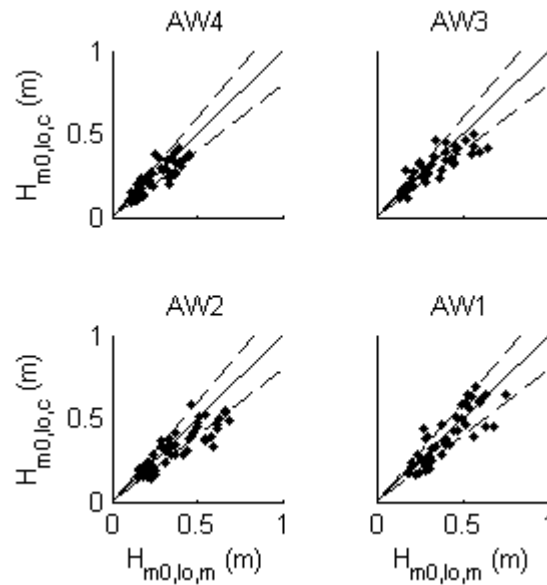


Figure 6.17 Measured  $H_{m0,lo,m}$  versus predicted  $H_{m0,lo,c}$  for case E6, from offshore (upper left) to nearshore (lower right). 20% error bands are indicated by the dashed lines.

### 6.4.3 Predictive skill

In accordance with previous studies (*Reniers et al., 2002, Bijl et al., 2009, Reniers et al., 2010*), the predictive capabilities of the model are assessed with a skill level:

$$\text{skill} = 1 - \frac{\sqrt{\langle (H_{rms,m} - H_{rms,c})^2 \rangle}}{\sqrt{\langle H_{rms,m}^2 \rangle}} \quad (6.1)$$

$H_{rms,m}$  and  $H_{rms,c}$  are the measured and predicted root mean square wave height, respectively, and  $\langle \dots \rangle$  denotes averaging over the 48 simulations. In this manner the skill is determined at every gauge for each of the three cases. The predictive skill gives an indication of the magnitude of the difference between the measurements and the predictions relative to the measured value. For a skill of 1 the difference is zero while for a value of 0 the difference is equal to the measured value.

Table 6.4 shows the skill at every wave gauge and the overall skill for all three cases. The results show that IDSB is capable of predicting the IG-wave conditions at a specific site with an average skill of 0.78. The results further indicate that the skill is of similar order of magnitude at most gauge locations for all three cases. The skill level found in this study is similar to the skill level reported in the previous studies (*Reniers et al., 2002, Bijl et al., 2009, Reniers et al., 2010*).

Table 6.4: Predictive skill for each individual gauge and averaged over all gauges (the overall skill).

	AW4	AW3	AW2	AW1	AD2	AD1	Overall
E2	0.78	0.83	0.78	0.73	-	-	0.78
E6	0.78	0.75	0.74	0.81	-	-	0.77
E8	0.83	0.78	0.74	0.75	0.80	0.81	0.79

## 7 Conclusions & Recommendations

---

IG-waves in coastal regions are a complex phenomenon to model and require an accurate simulation of all relevant nearshore processes. It is therefore important to have insight into the capabilities and limitations of numerical models when predicting such wave conditions. In this study an attempt is made to improve the understanding of the simulated nearshore infragravity wave behaviour. Here, the findings of the study are summarized and discussed, followed by the conclusions. Finally, recommendations for future studies are presented.

First, the influence of wave conditions and bathymetry on the IG-wave height is studied. In a number of cases the influence of the bottom slope, significant wave height, peak period, directional spreading and mean incident angle on the predicted wave height are investigated. The results show that the predictions are qualitatively consistent with both field measurements and theory. An exception is found for a steep slope (1:10), where IDSB predicts unrealistic IG-wave heights. Laboratory studies showed that the time-varying breakpoint mechanism is dominant for steep slopes (*Baldock et al., 2000*). Since IDSB does not incorporate this mechanism it is invalid for steep slopes, which provides an explanation for the observed wave heights.

Next, a detailed analysis is carried out in which a high-resolution flume data set is used to analyse the simulated nearshore IG-wave behaviour. The results for IDSB show that the significant IG-wave height is predicted accurately in the offshore region (seaward of the surf-zone), while inside the surf-zone the IG-wave height is over predicted. In contrast, SWASH under predicts the IG-wave height in the offshore region, while in the surf zone the predictions match the measurements.

The cross-correlation technique is used to visualize the propagation and reflection of the infragravity waves. The results for IDSB and SWASH show that an incoming IG-wave, which propagates with a velocity slightly smaller than the group velocity, is reflected at the shoreline. After reflection, the IG-wave propagates in the seaward direction with the phase velocity. The simulated propagation properties are consistent with both the flume measurements and theory.

A signal decomposition technique is used to quantify the magnitude of the incoming and reflected IG-waves. In the offshore region, the IDSB predicted incoming and the reflected IG-wave heights are of similar order of magnitude to those measured, while IDSB over predicts the incoming and reflected IG-wave height in the surf zone. The SWASH results show that the incoming IG-wave height is under predicted in the offshore region, while inside the surf zone the predictions are of similar order of magnitude to those measured. This under-prediction in the offshore region is associated with the absence of an incoming bound IG-wave at the offshore boundary. It is argued that the absent bound IG-wave is generated inside the domain, which could explain the match of the predicted and measured IG-wave

heights inside the surf zone. The reflected IG-wave height shows a similar pattern compared to the measurements, however, the magnitude is under predicted throughout the domain. This under prediction is associated with an under prediction of the shoreline reflection.

Additionally, a distinction is made between relatively long and relatively short IG-waves. The results for the measurements are similar to observations by *Battjes et al. (2004)*. They reported a frequency dependent shoreline reflection: relatively long IG-waves are fully reflected, while relatively short IG-waves experience strong dissipation. This frequency dependant reflection is not present in IDSB, which shows full reflection of relatively short IG-waves, this confirms observations by *Reniers et al. (2010)*. They further suggested that this is due to the absence of dissipative processes in IDSB, for example, IG-wave breaking (*Van Dongeren et al., 2007*) or an energy transfer from the IG-waves to the short waves by non-linear wave interactions (*Thomson et al., 2006, Henderson et al., 2006*). In contrast to IDSB, the shoreline reflection in SWASH shows good correspondence with the measurements. Since SWASH is capable of simulating wave breaking and nonlinear interactions (*Zijlema et al., 2011*), these observations suggest that SWASH incorporates the dissipative processes.

The accuracy of the IG-wave height predictions by IDSB are assessed using field measurements obtained at the Field Research Facility in Duck, North Carolina (USA). The field data set consists of wave measurements in intermediate water depths seaward of the surf zone (ranging from 3 – 14m water depths). Comparison of the predicted and measured energy density spectra show that the spectral shape predicted by IDSB generally differs from the measured spectra. In contrast, comparison of the predicted and measured significant IG-wave heights at all gauge locations shows an average skill of 0.78. This skill level is in agreement with skill levels observed in previous studies (*Reniers et al., 2002, Bijl et al., 2009, Reniers et al., 2010*).

It can be concluded that, provided that bound IG-waves are dominant and most IG-waves significantly reflect at the shoreline, IDSB provides a suitable method to obtain estimates of the IG-wave heights at an arbitrary location outside the surf zone. This conclusion confirms findings by *Reniers et al. (2010)*. For more detailed insight in the IG-wave field one has to rely on more sophisticated numerical models like SWASH. This study shows that SWASH is capable of correctly simulating the nearshore IG-wave behaviour. However, further development is required since incoming bound IG-waves are currently absent in the SWASH forcing. It is therefore recommended that second order accurate wave forcing is included in SWASH to allow for the correct generation of bound IG-waves at the offshore boundary. The results further indicate that the shoreline reflection is under predicted by SWASH. It is valuable to gain additional insight into this under prediction. Therefore, it is recommended to use additional laboratory experiments for a further investigation into the shoreline reflection.

## Bibliography

---

- BALDOCK, T. E., HUNTLEY, D. A., BIRD, P. A. D., O'HARE, T. & BULLOCK, G. N. 2000. Breakpoint generated surf beat induced by bichromatic wave groups. *Coastal Engineering*, 39, 213-242.
- BATTJES, J. A., BAKKENES, H. J., JANSSEN, T. T. & DONGEREN, A. R. 2004. Shoaling of subharmonic gravity waves. *Journal of Geophysical Research*, 109.
- BATTJES, J. A. & JANSSEN, J. P. F. Year. Energy Loss and Set-Up Due to Breaking of Random Waves. *In: Coastal Engineering*, 1978 Hamburg, Germany. New York, ASCE, 569-587.
- BATTJES, J. A. & STIVE, M. J. F. 1985. Calibration and Verification of a Dissipation Model for Random Breaking Waves. *Journal of Geophysical Research*, 90, 9159-9167.
- BIJL, M., RENIERS, A., EWANS, K., MASTERTON, S. & HUIJSMANS, R. Year. Evaluation of a Model for Estimating Infragravity Waves in Shallow Water: Accuracy and Suitability for Long-Term Climatologies. *In: ASME Conference Proceedings*, 2009 Honolulu. ASME, 757-765.
- BOERS, M. 1996. Simulation of a surf zone with a barred beach, report 1 : wave heights and wave breaking. *Communications on Hydraulic and Geotechnical Engineering*. Delft: TUD Technical University Delft.
- BROMIRSKI, P. D., SERGIENKO, O. V. & MACAYEAL, D. R. 2010. Transoceanic infragravity waves impacting Antarctic ice shelves. *Geophysical Research Letters*, 37, L02502.
- CHEN, G. Y., CHIEN, C. C., SU, C. H. & TSENG, H. M. 2004. Resonance induced by edge waves in Hualien Harbor. *Journal of oceanography*, 60, 1035-1043.
- DUNCAN, J. H. 1981. An Experimental Investigation of Breaking Waves Produced by a Towed Hydrofoil. *Proceedings of the Royal Society of London. A. Mathematical and Physical Sciences*, 377, 331-348.
- ECKART, C. 1951. Surface waves on water of variable depth. *Scripps Inst. of Oceanogr., Univ. of Calif., La Jolla*.
- ELDEBERKY, Y. & BATTJES, J. A. 1996. Spectral modeling of wave breaking: Application to Boussinesq equations. *J. Geophys. Res.*, 101, 1253-1264.
- ELGAR, S., HERBERS, T. H. C., OKIHIRO, M., OLTMAN-SHAY, J. & GUZA, R. T. 1992. Observations of Infragravity Waves. *J. Geophys. Res.*, 97, 15573-15577.
- GALLAGHER, B. 1971. Generation of surf beat by non-linear wave interactions. *Journal of Fluid Mechanics*, 49, 1-20.
- GUZA, R., THORNTON, E. & HOLMAN, R. Year. Swash on steep and shallow beaches. *In: Coastal Engineering*, 1984 Houston. ASCE, 708-723.
- HENDERSON, S. M., GUZA, R. T., ELGAR, S., HERBERS, T. H. C. & BOWEN, A. J. 2006. Nonlinear generation and loss of infragravity wave energy. *J. Geophys. Res.*, 111, C12007.
- HERBERS, T. H. C., ELGAR, S. & GUZA, R. T. 1994. Infragravity-Frequency (0.005-0.05 Hz) Motions on the Shelf. Part I: Forced Waves. *Journal of Physical Oceanography*, 24, 917-927.
- HERBERS, T. H. C., ELGAR, S. & GUZA, R. T. 1995a. Generation and propagation of infragravity waves. *J. Geophys. Res.*, 100, 24863-24872.
- HERBERS, T. H. C., ELGAR, S., GUZA, R. T. & O'REILLY, W. C. 1995b. Infragravity-Frequency (0.005-0.05 Hz) Motions on the Shelf. Part II: Free Waves. *Journal of Physical Oceanography*, 25, 1063-1079.
- HOLTHUIJSEN, L. H. 2007. *Waves in oceanic and coastal waters*, Cambridge University Press.

- JANSSEN, T. T., BATTJES, J. A. & VAN DONGEREN, A. R. 2003. Long waves induced by short-wave groups over a sloping bottom. *J. Geophys. Res.*, 108, 3252.
- KLOPMAN, G. & VAN LEEUWEN, P. J. Year. An efficient method for the reproduction of non-linear random waves. *In: Coastal Engineering*, 1990 Delft, The Netherlands. ASCE, 478-488.
- LONGUET-HIGGINS, M. S. & STEWART, R. W. 1962. Radiation stress and mass transport in gravity waves, with application to 'surf beats'. *Journal of Fluid Mechanics*, 12, 481 - 504.
- MADSEN, P. A., SØRENSEN, O. R. & SCHÄFFER, H. A. 1997. Surf zone dynamics simulated by a Boussinesq type model. Part II: surf beat and swash oscillations for wave groups and irregular waves. *Coastal Engineering*, 32, 289-319.
- NACIRI, M., BUCHNER, B., BUNNIK, T., HUIJSMANS, R. & ANDREWS, J. Year. Low frequency motions of LNG carriers moored in shallow water. *In: Offshore mechanics and Arctic Engineering*, 2004 Vancouver, Canada.
- NAIRN, R. B., ROELVINK, J. A. & SOUTHGATE, H. N. Year. Transition Zone Width and Implications for Modeling Surfzone Hydrodynamics. *In: Coastal Engineering*, 1990 Delft, The Netherlands. ASCE, 68-81.
- OKIHIRO, M., GUZA, R. T. & SEYMOUR, R. J. 1992. Bound Infragravity Waves. *J. Geophys. Res.*, 97, 11453-11469.
- OLTMAN-SHAY, J. & GUZA, R. T. 1987. Infragravity Edge Wave Observations on Two California Beaches. *Journal of Physical Oceanography*, 17, 644-663.
- RENIERS, A. J. H. M. & BATTJES, J. A. 1997. A laboratory study of longshore currents over barred and non-barred beaches. *Coastal Engineering*, 30, 1 - 21.
- RENIERS, A. J. H. M., GROENEWEGEN, M. J., EWANS, K. C., MASTERTON, S., STELLING, G. S. & MEEK, J. 2010. Estimation of infragravity waves at intermediate water depth. *Coastal Engineering*, 57, 52 - 61.
- RENIERS, A. J. H. M., VAN DONGEREN, A. R., BATTJES, J. A. & THORNTON, E. B. 2002. Linear modeling of infragravity waves during Delilah. *Journal of Geophysical Research*, 107.
- ROELVINK, D., RENIERS, A., VAN DONGEREN, A., VAN THIEL DE VRIES, J., MCCALL, R. & LESCINSKI, J. 2009. Modelling storm impacts on beaches, dunes and barrier islands. *Coastal Engineering*, 56, 1133-1152.
- RUESSINK, B. G. 1998. Bound and free infragravity waves in the nearshore zone under breaking and nonbreaking conditions. *J. Geophys. Res.*, 103, 12795-12805.
- SCHÄFFER, H. A. & JONSSON, I. G. 1992. Edge waves revisited. *Coastal Engineering*, 16, 349-368.
- SCHÄFFER, H. M. 1993. Infragravity waves induced by short-wave groups. *Journal of Fluid Mechanics*, 247, 551-588.
- SHEREMET, A., GUZA, R. T., ELGAR, S. & HERBERS, T. H. C. 2002. Observations of nearshore infragravity waves: Seaward and shoreward propagating components. *J. Geophys. Res.*, 107, 3095.
- STEENBERGEN, G. 2005. *Directional Decomposition of Subharmonic Surfbeat Waves*. MSc Thesis, Delft University of Technology.
- STELLING, G. & ZIJLEMA, M. 2003. An accurate and efficient finite-difference algorithm for non-hydrostatic free-surface flow with application to wave propagation. *International Journal for Numerical Methods in Fluids*, 43, 1-23.
- STIVE, M. J. F. & DE VRIEND, H. J. Year. Shear stresses and mean flows in shoaling and breaking waves. *In: Coastal Engineering*, 1994 New York, USA. ASCE, 598-605.
- SVENDSEN, I. A. 1984. Wave heights and set-up in a surf zone. *Coastal Engineering*, 8, 303 - 329.

- SVENDSEN, I. A. 2006. *Introduction To Nearshore Dynamics*, World Scientific Publishing Co. Pte. Ltd.
- SYMONDS, G., HUNTLEY, D. A. & BOWEN, A. J. 1982. Two-Dimensional Surf Beat: Long Wave Generation by a Time-Varying Breakpoint. *J. Geophys. Res.*, 87, 492-498.
- THOMSON, J., ELGAR, S., RAUBENHEIMER, B., HERBERS, T. H. C. & GUZA, R. T. 2006. Tidal modulation of infragravity waves via nonlinear energy losses in the surfzone. *Geophys. Res. Lett.*, 33, L05601.
- VAN DER MOLEN, W., MONARDEZ, P. & VAN DONGEREN, A. 2006. Numerical simulation of long-period waves and ship motions in Tomakomai Port, Japan. *Coastal Engineering Journal*, 48, 59-79.
- VAN DONGEREN, A., BATTJES, J., JANSSEN, T., VAN NOORLOOS, J., STEENHAUER, K., STEENBERGEN, G. & RENIERS, A. 2007. Shoaling and shoreline dissipation of low-frequency waves. *J. Geophys. Res.*, 112, C02011.
- VAN THIEL DE VRIES, J. S. M., VAN GENT, M. R. A., WALSTRA, D. J. R. & RENIERS, A. J. H. M. 2008. Analysis of dune erosion processes in large-scale flume experiments. *Coastal Engineering*, 55, 1028-1040.
- WEBB, S. C., ZHANG, X. & CRAWFORD, W. 1991. Infragravity Waves in the Deep Ocean. *J. Geophys. Res.*, 96, 2723-2736.
- ZIJLEMA, M., STELLING, G. & SMIT, P. 2011. SWASH: An operational public domain code for simulating wave fields and rapidly varied flows in coastal waters. *Coastal Engineering*, 58, 992-1012.
- ZIJLEMA, M. & STELLING, G. S. 2005. Further experiences with computing non-hydrostatic free-surface flows involving water waves. *International Journal for Numerical Methods in Fluids*, 48, 169-197.
- ZIJLEMA, M. & STELLING, G. S. 2008. Efficient computation of surf zone waves using the nonlinear shallow water equations with non-hydrostatic pressure. *Coastal Engineering*, 55, 780 - 790.

## List of main symbols

---

### *Roman symbols*

A	Wave envelope	m
E	Energy	$\text{J m}^{-2}$
$H_0$	Deep water wave height	m
$H_{\max}$	Maximum wave height	m
$H_{m0}$	Significant wave height	m
$H_{m0,lo}$	Significant infragravity wave height	m
$H_{\text{rms}}$	Root mean square wave height	m
L	Wave length	m
$L_0$	Deep water wave length	m
S	Radiation stress	$\text{N m}^{-1}$
T	Wave period	s
$T_p$	Peak period	s
U	Mean cross-shore velocity	$\text{m s}^{-1}$
$U_{\text{rms}}$	Root mean square short-wave near-bed velocity	$\text{m s}^{-1}$
V	Alongshore current velocity	$\text{m s}^{-1}$
c	Phase speed	$\text{m s}^{-1}$
$c_f$	Friction coefficient	-
$c_g$	Group velocity	$\text{m s}^{-1}$
d	Still water depth	m
g	Gravitational acceleration	$\text{m s}^{-2}$
h	Total water depth	m
k	Wave number	$\text{rad m}^{-1}$
$l_m$	Mixing length	m
n	Ratio between the group velocity and the phase velocity (c)	-
$n_e$	Edge wave mode	-
$n_m$	Manning coefficient	-
q	Non-hydrostatic pressure term	$\text{N m}^{-2}$
u	Velocity in cross-shore direction	$\text{m s}^{-1}$
v	Velocity in alongshore direction	$\text{m s}^{-1}$

### *Greek symbols*

$\alpha$	IDSB parameter	-
$\beta$	Bottom slope	-
$\beta_n$	Normalized bottom slope	-
$\beta_r$	Wave front angle	rad
$\gamma$	Wave breaking parameter	-
$\theta$	Wave angle	°
$\zeta$	Surface elevation	m
$\zeta_{IG}$	Infragravity surface elevation	m
$\rho$	Density	kg m <sup>-3</sup>
$\sigma_\theta$	Directional width	°
$\tau$	Turbulent stress	N m <sup>2</sup>

### *Subscripts*

$x,y$	Indices corresponding to the cross-shore and alongshore direction
-------	---

# Appendices

---

## A. Signal decomposition

Two techniques are described in the literature to estimate the incident and outgoing IG-wave using the total IG-wave signal. The 'array method' decomposes the total signal in the frequency domain based on the surface elevation measured at several cross-shore locations (*Battjes et al., 2004, Steenbergen, 2005, Van Dongeren et al., 2007*). The 'collocated method' decomposes the signal in the time domain based on both the sea surface elevation and velocity time signal of the IG-waves (*Guza et al., 1984*).

### Array method

The array method decomposes the total surface elevation signal in the Fourier domain using measured surface elevations at different locations, the so called local array. The local array is a set of consecutive measurement gauges  $p = 1, 2, \dots, P$  centered on a reference gauge  $p = R$ . The array method decomposes the signal using the measurements at the local array to estimate the incoming and outgoing waves at the reference location.

The Fourier transformation of the surface elevation signal at gauge  $p$  results in a complex amplitude for each harmonic (A.1).  $Z_{m,p}$  is the measured complex amplitude,  $j$  is a time counter,  $N$  is the total number of points in the time series,  $f_m$  is the long-wave frequency and  $m$  the two-sided frequency counter ( $0, \pm 1, \pm 2, \dots, \pm N/2$ )

$$Z_{m,p} = \frac{1}{N} \sum_{j=1}^N \zeta(x_p, t_j) e^{-i2\pi f_m t_j} \quad (\text{A.1})$$

Each measured (complex) wave component at the reference gauge  $R$  is assumed to be a combination of an incoming and outgoing wave component (A.2).  $Q^+$  and  $Q^-$  are complex operators which incorporate the effect of the amplitude (shoaling) and phase variation over the cross-shore under the assumption of linear propagation and energy conservation.

$$Q_{m,p}^+ Z_{m,R}^+ + Q_{m,p}^- Z_{m,R}^- = Z_{m,p} \quad (\text{A.2})$$

The resulting set of equations in matrix form is given by (A.3) and consists of  $P$  equations and two unknowns. For  $P > 2$  the system of equations is over determined and the solution results from the method of least squares.

$$\underbrace{\begin{bmatrix} Q_{m,l}^+ & Q_{m,l}^- \\ Q_{m,R}^+ & Q_{m,R}^- \\ Q_{m,P}^+ & Q_{m,P}^- \end{bmatrix}}_B \begin{bmatrix} Z_{m,R}^+ \\ Z_{m,R}^- \end{bmatrix} = \begin{bmatrix} Z_{m,l} \\ Z_{m,R} \\ Z_{m,P} \end{bmatrix} \quad (\text{A.3})$$

*Battjes et al. (2004)* solved this set of equations with the operators  $Q^\pm$  accounting for the amplitude and phase variation (of the in- and outgoing wave) between the reference location ( $R$ ) and the gauge location ( $p$ ) within the local array. The method described by *Steenbergen (2005)* and *van Dongeren et al. (2007)* uses the same method but uses a multi-step approach to account for the amplitude and phase variations. Both methods assume an incoming bound wave propagating with the group velocity corresponding to the peak of the short-wave spectrum and an outgoing free wave propagating according to the dispersion relationship.

The single step method describes the complex operator as (A.4) in which the ratio between the velocities accounts for the amplitude variation and the exponential operator for the phase variation over the local array. The phase is obtained according linear theory by integrating the wave number from  $x_p$  to  $x_r$ , (A.5)

$$Q_{m,p}^\pm = \sqrt{c_R^\pm / c_p^\pm} e^{i(\psi_{m,p}^\pm - \psi_{m,R}^\pm)} \quad (\text{A.4})$$

$$\psi_{m,p}^\pm = \mp \int_{x=x_p}^{x=x_R} k_{m,p}^\pm = \mp \int_{x=x_p}^{x=x_R} \frac{2\pi f_m}{c_p^\pm} dx \quad (\text{A.5})$$

In the multiple step method (*Steenbergen, 2005, Van Dongeren et al., 2007*) an iterative procedure is used to calculate the estimates of the in- and outgoing IG-wave. In each individual step a correction is applied using the complex operator  $Q$  for either the phase or amplitude variation of the incoming and outgoing wave respectively. Each iteration (A.3) is solved and in the subsequent iteration the complex operator is adapted with a new correction. This method results in five iterations:

1. Initial phase estimation using linear wave theory
2. Phase correction for the incoming wave
3. Amplitude correction for the incoming wave
4. Phase correction for the outgoing wave
5. Amplitude correction for the outgoing wave

The resulting set of equations can be described by (A.6) including the iterative procedure by the iteration number  $n$ .

$$\begin{bmatrix} Q_{m,1,n}^+ & Q_{m,1,n}^- \\ Q_{m,R,n}^+ & Q_{m,R,n}^- \\ Q_{m,P,n}^+ & Q_{m,P,n}^- \end{bmatrix} \begin{bmatrix} Z_{m,R,n}^+ \\ Z_{m,R,n}^- \end{bmatrix} = \begin{bmatrix} Z_{m,1} \\ Z_{m,R} \\ Z_{m,P} \end{bmatrix} \quad (\text{A.6})$$

The initial phase estimates for the first step are obtained using linear wave theory by integrating the corresponding wave number from the first gauge up to the location of interest (A.7).

$$\psi_{m,p}^{\pm} = \mp \int_{x=0}^{x=x_p} \frac{2\pi f_m}{c_p^{\pm}} dx \quad (\text{A.7})$$

In each following step the operator is adapted for the corresponding correction. The operator for step 1-5 is given by (A.8)-(A.13).

$$Q_{m,p,1}^{\pm} = e^{i\psi_{m,p}^{\pm}} \quad (\text{A.8})$$

$$Q_{m,p,2}^+ = \frac{Z_{m,p,1}^+}{Z_{m,R,1}^+} \frac{|Z_{m,R,1}^+|}{|Z_{m,p,1}^+|} Q_{m,p,1}^+ \quad (\text{A.9})$$

$$Q_{m,p,3}^+ = \frac{|Z_{m,p,2}^+|}{|Z_{m,R,2}^+|} Q_{m,p,2}^+ \quad (\text{A.10})$$

$$Q_{m,p,4}^- = \frac{Z_{m,p,3}^-}{Z_{m,R,3}^-} \frac{|Z_{m,R,3}^-|}{|Z_{m,p,3}^-|} Q_{m,p,3}^{\pm} \quad (\text{A.11})$$

$$Q_{m,p,5}^- = \frac{|Z_{m,p,4}^-|}{|Z_{m,R,4}^-|} Q_{m,p,4}^{\pm} \quad (\text{A.12})$$

To get accurate results for the single-step method the phase difference over the local array should be great enough; for small differences matrix B becomes ill-conditioned resulting in high sensitivity to noise in the measurements (*Battjes et al., 2004*). For greater frequencies the wave length decreases and the phase difference over the local array increases. Therefore a longer local array is required for lower- than for higher frequencies. The assumptions for the complex operators require a minimum array length to prevent great errors to occur. These conflicting demands should be taken into account when deciding the

array length. *Steenbergen (2005)* found that the number of gauges in the local array did not significantly affect the results.

Both methods result in the complex amplitude of the incoming and outgoing wave height. The integral wave height of the incident and outgoing IG-wave limited by the frequency limits  $f_l$  and  $f_h$  results from (A.13).

$$H_{m0,f}^{\pm} = 4 \sqrt{\int_{f_l}^{f_h} 0.5 |Z^{\pm}|^2} \quad (\text{A.13})$$

### Collocated method

The time series of the surface and velocity signal of linear waves unidirectional in x-direction can be written as (A.14) and (A.15) respectively, where superscript + and – denote the incoming and outgoing component respectively.

$$\zeta(x, t) = \zeta^+(x, t) + \zeta^-(x, t) \quad (\text{A.14})$$

$$u(x, t) = u^+(x, t) + u^-(x, t) \quad (\text{A.15})$$

Considering very shallow water, the velocity is given by (A.16), with the angular frequency  $\omega$ , wave period  $k$  and IG-wave surface elevation  $\zeta$ . The ratio of the angular frequency and the wave number can be written as the phase speed of an individual wave  $c$ .

$$u = \frac{\omega}{kh} \zeta = \frac{c}{h} \zeta \quad (\text{A.16})$$

Substituting (A.16) for the incoming and outgoing IG-wave in (A.15) results in (A.17), dropping the spatial and time dependency  $(x, t)$ . The minus sign in the RHS results from the velocity of the outgoing wave which is negative due to its direction.

$$u = c^+ \frac{\zeta^+}{h} - c^- \frac{\zeta^-}{h} \quad (\text{A.17})$$

Equation (A.14) and (A.17) form a set of two equations with two unknowns ( $\zeta^+$  and  $\zeta^-$ ). Solving the set of equations for the incoming and outgoing IG-wave surface elevation results in (A.18) and (A.19) respectively.

$$\zeta^+ = \frac{c^- \zeta + uh}{c^+ + c^-} \quad (\text{A.18})$$

$$\zeta^- = \frac{c^+ \zeta - uh}{c^+ + c^-} \quad (\text{A.19})$$

The incoming IG-waves are assumed to be bound and to propagate with the group velocity corresponding to the peak period of the short-wave spectrum  $c_g$ , the outgoing IG-waves are free waves propagating with the phase velocity  $c = \sqrt{gh}$  (assuming very shallow water).

If the in- and outgoing wave are assumed to propagate with the very shallow water phase velocity, the solution according to *Guza et al. (1984)* is recovered:

$$\zeta^+ = \frac{1}{2} \left( \zeta + \sqrt{\frac{h}{g}} \right) \quad (\text{A.20})$$

$$\zeta^+ = \frac{1}{2} \left( \zeta - \sqrt{\frac{h}{g}} \right) \quad (\text{A.21})$$



## B. Cross-correlation

The cross-correlation function of two time signals  $X$  and  $Y$ , for a random stationary process with zero mean, is given by

$$R_{XY}(\tau) = \frac{\langle X(t)Y(t + \tau) \rangle}{\sigma_X \sigma_Y} \quad (\text{B.1})$$

Where  $\langle \dots \rangle$  denotes time averaging,  $\tau$  a time shift and  $\sigma_X$  and  $\sigma_Y$  the standard deviation of  $X(t)$  and  $Y(t)$  respectively. The resulting cross-correlation  $R_{xy}$  is a value between -1 and 1 and indicates how both signals are correlated for a range of time-shifts. For two identical wave signals in phase the cross-correlation is 1 while for two identical signals out of phase the cross-correlation is equal to -1.

Figure B.1 shows the cross-correlation for the two harmonic wave signals. For a time shift equal to 0s the signals are identical and perfectly correlated, resulting in a correlation of 1. For a time shift of 0.5 seconds, the same time signal is observed which is in anti-phase with the original signal, resulting in a correlation of -1. For increasing time shifts the signals are again in phase and in anti-phase which results in a harmonic pattern of the correlation function.

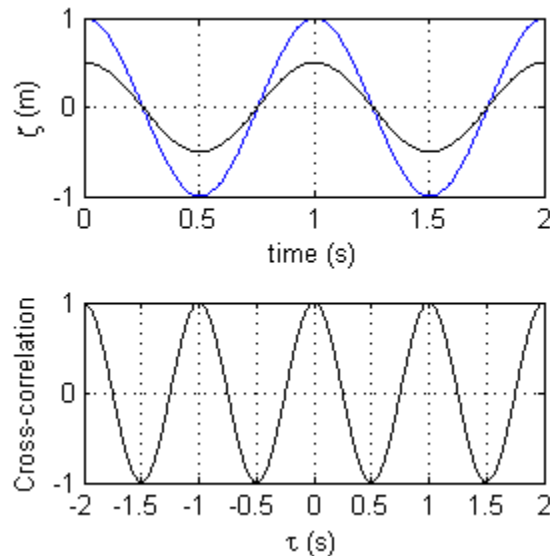


Figure B.1: Autocorrelation of a harmonic wave signal

In this research the cross-correlation function will be applied to a (partial) reflected signal. Figure B.2 shows an example of such a signal with the associated cross-correlation function. In the upper panel a signal is shown for two locations ( $x=0\text{m}$  and  $x=18\text{m}$ ). This signal corresponds to an incoming pulse that propagates in shoreward direction (visible after roughly 10s) and reflects at the shoreline. Subsequently the partial reflected pulse propagates in seaward direction (visible after roughly 120s). The resulting

cross-correlation of these two signals shows four distinctive regions of high correlation. A positive time shift results in two peaks of correlation (indicated by 1 and 3 in the lower panel of Figure B.2). The largest correlation occurs for a time shift  $\tau_1$  and this corresponds to the similarity between the incoming signals at both locations. The correlation peak indicated by 3 results due to the similarity between the incoming pulse at  $x=0\text{m}$  and the reflected pulse at  $x=18\text{m}$ . Correlations for positive time shifts results from the similarity of the incoming signal at  $x=0\text{m}$  and the incident ( $\tau_1$ ) and reflected signal ( $\tau_3$ ) at  $x=18\text{m}$ . Correlations for negative time shifts, in a similar manner, results from the similarity between the reflected signal at  $x=18\text{m}$  and the incident ( $\tau_4$ ) and reflected ( $\tau_2$ ) signal at  $x=0\text{m}$ .

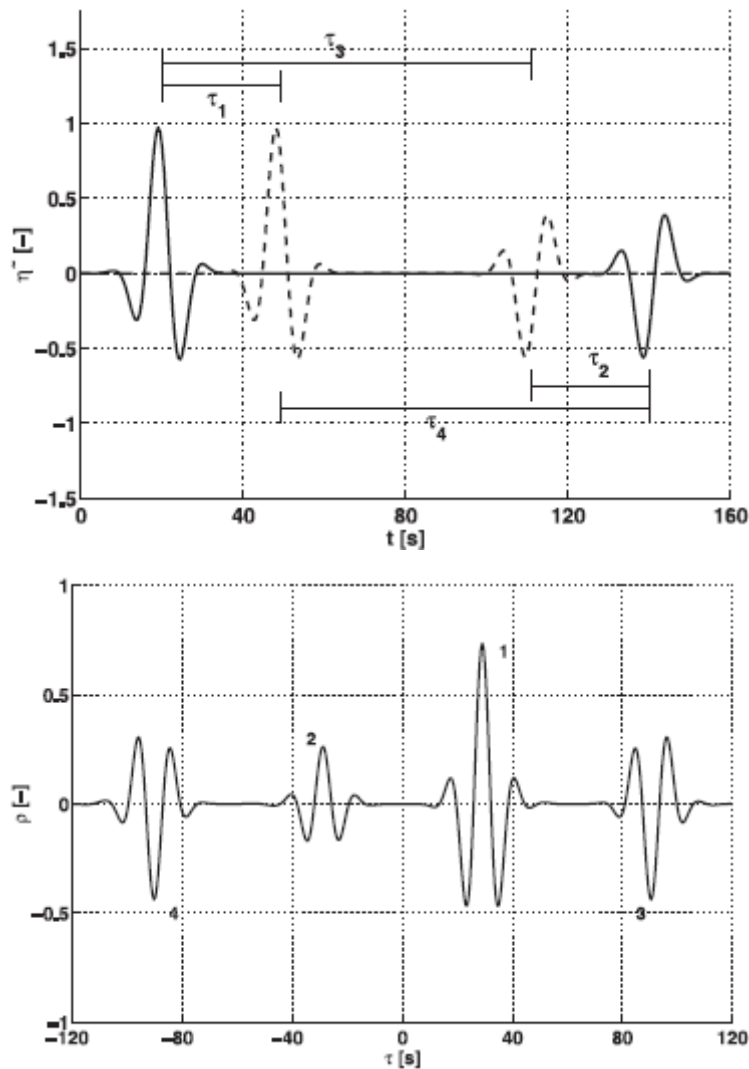


Figure B.2: Example of the cross-correlation of a (partial) reflected signal. (a) Thick line: pulse signal at  $x=0\text{m}$  consisting of an incoming pulse ( $t=20\text{s}$ ) and its partial reflection ( $t=140\text{s}$ ). Dashed line: similar observation at  $x=18\text{m}$ . (b) Cross-correlation function between the two wave signals. After Janssen et al. (2003).

### C. Wave envelope

The forcing of the IG-waves is associated with the variation of the wave amplitude on wave group scale. The wave envelope gives a measure of this amplitude variation. The wave envelope of the short waves is obtained by applying the Hilbert transform on the short-wave surface elevation  $\zeta^{hf}$ , whereby the superscript hf is related to the frequency range of the short waves. Since the wave envelope is used to give a measure of the amplitude variation on wave group scale, the frequency limits of the wave envelope correspond to the frequency limits of the low frequencies (lf). The wave envelope is therefore defined as (Janssen et al., 2003):

$$|A(t)| = \left| \zeta^{hf}(t) + i\Gamma\{\zeta^{hf}(t)\} \right|^{lf} \quad (\text{C.1})$$

Where  $\Gamma\{\dots\}$  denotes the Hilbert transform operator. For a relative narrow band process, the absolute value of the obtained time series  $|A(t)|$  is represents the envelope of the surface elevation signal, see Figure C.1.

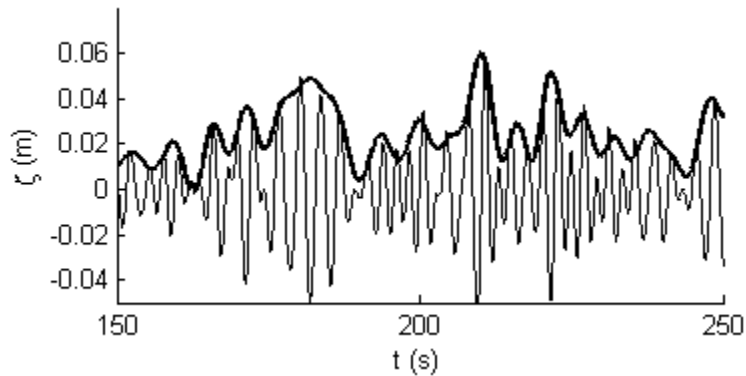


Figure C.1: Wave envelope, determined using the Hilbert transform. High frequency surface elevation signal  $\zeta^{hf}$  (thin line) and short-wave envelope  $|A(t)|$  (thick line).



## D. Sensitivity study – SWASH set up, additional information

The following provides some additional information of the SWASH model setup used in the sensitivity study.

### Grid size

The grid size must provide enough resolution to accurately simulate the waves, e.g. for propagating linear waves approximately 20 grid points are required. If the grid resolution is too coarse, waves are not simulated accurately. For decreasing grid sizes the results will converge as all waves present in the domain are modelled with sufficient resolution. The sensitivity of the results to the grid resolution is investigated to analyze if convergence occurs for decreasing grid sizes.

A grid size of 1m does not fulfil the requirement of 20 grid points per wave length near the shoreward boundary. The sensitivity of the integral wave parameters to the grid resolution is checked for the wave simulation with the greatest incoming significant wave height. The results for case 2, simulation D ( $H_s$  of 3m) converge for a decreasing grid size (Figure D.1). The overall difference between the largest grid size (1m) and the smallest grid size (0.05m) amounts 3% for the short-wave height and 8% for the IG-wave height. The goal of the sensitivity study is to compare both model outcomes in a qualitative manner. Although the magnitude of the deviation is significant, the pattern of the integral wave parameters remains similar. Therefore the model results with a grid size of 1m are assumed sufficiently accurate for the goal of this sensitivity study.

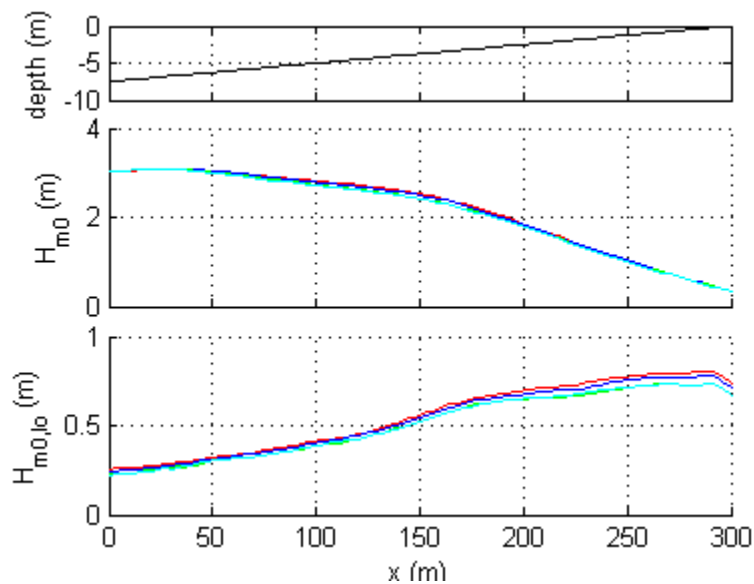


Figure D.1: Influence grid size on the SWASH results for case 2, simulation D (incident significant wave height of 3m). Grid size: 1m (red); 0.5m (blue); 0.1m (green) and 0.05m (cyan).

### Number of vertical layers

The number of vertical layers may also influence the results. The frequency dispersion is solved more accurately for an increasing number of vertical layers. For example, for two vertical layers good linear dispersion is obtained up to normalized depths of  $kh \approx 7$  and  $kh \approx 3$  for standing and propagating waves, respectively, (Zijlema *et al.*, 2011). The influence of the number of vertical layers is investigated for the most critical wave condition, i.e. the simulations with the smallest peak periods and therefore greatest  $kh$  values (case 3, simulation D: a  $T_p$  of 6s). Figure D.2 shows the  $kh$  value at the offshore boundary for varying peak periods. The wave number is determined using the linear dispersion relationship for three frequencies:  $T_p$ ;  $2T_p$  and  $3T_p$ . The frequency dispersion limitation is critical for the waves with the greatest  $kh$  value, i.e. waves with the shortest wave length (greater frequencies).

The results for simulations with a peak period of 6s and an increasing amount of vertical layers (up to three vertical layers) show to converge for an increasing number of vertical layers, Figure D.3. With similar reasoning as for the grid size, the overall accuracy for one vertical layer is assumed to be sufficient for the goal of this study.

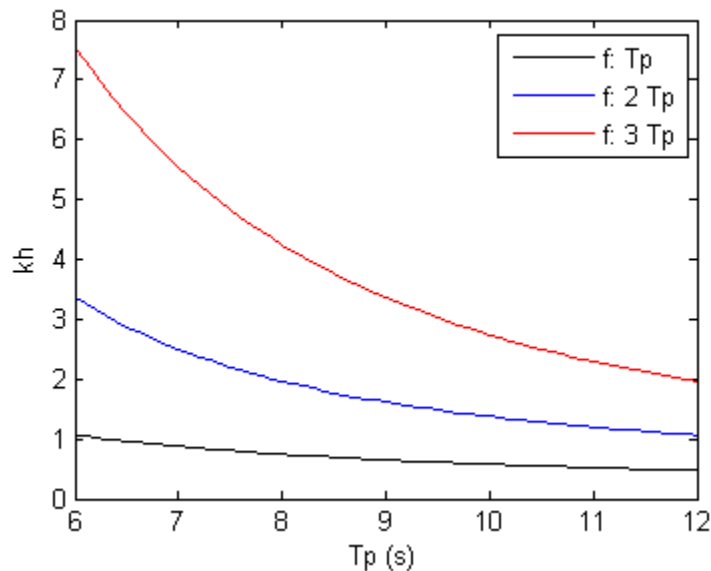


Figure D.2:  $kh$  values at a depth of 7.5m for a varying peak period obtained for the peak period  $T_p$  (black),  $2 T_p$  (blue) and  $3 T_p$  (red).

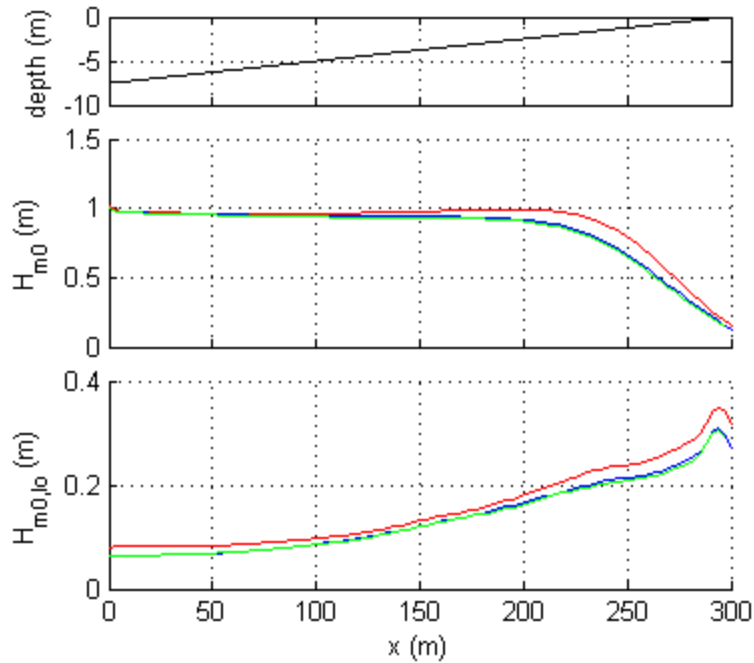


Figure D.3: Influence number of vertical layers on the SWASH computed integral wave parameters. Results for case 3 simulation D ( $T_p$  6s) with 1 layer (red); 2 layers (blue) and 3 layers (green). Upper panel: Bottom profile, middle panel: significant short-wave height and lower panel: significant IG-wave height.

### Domain width

For the simulations with oblique incident waves the domain width is chosen using the minimal domain width (3.39), which provides an approximation of the minimal required width. The minimum domain width for the various incident angles (directional width plus mean incident angle) is shown in Table 7.1.

Table 7.1: Minimal domain width

$\theta_{in} + \sigma_{\theta}$ (°)	10	15	20	30	40
Width (m)	106	161	218	346	503

A number of simulations with a varying domain width and with similar wave conditions is executed to gain insight in the influence of the domain width on the integral wave parameters. Convergent behaviour is expected for widths greater than the minimal widths as the lateral boundaries no longer influence the results in the region of interest (a cross-shore array in the middle of the domain). The influence of the domain width is investigated for the simulation with the greatest minimal domain width: the simulation for a directional width of 40°.

The predictions of the integral wave parameters for a varying domain width are shown in Figure D.4. For a domain width smaller than the minimal width the short-wave height shows some oscillation in the offshore region. For a domain width of 500m and 1000m the results are fairly similar. For increasing domain widths (up to 4000m) the short-wave height decreases throughout the domain. Overall the

results show non-convergent behaviour for increasing domain width, the reason for this non-convergent behaviour is unknown and due to time constraints this deviation is not further investigated.

The results for a domain width of 1000m are assumed to provide reasonable accurate predictions of the short-wave height: the short waves shoal in the offshore region and a strong decrease of the short-wave height occurs in the nearshore (associated with wave breaking). For all the simulations with oblique incident waves, a domain width of approximately twice the minimal domain width is assumed to give sufficient accurate results for the qualitative comparison. The resulting domain widths for the various simulations are chosen at values with an order of magnitude of roughly twice the minimal domain width, see Table D-1.

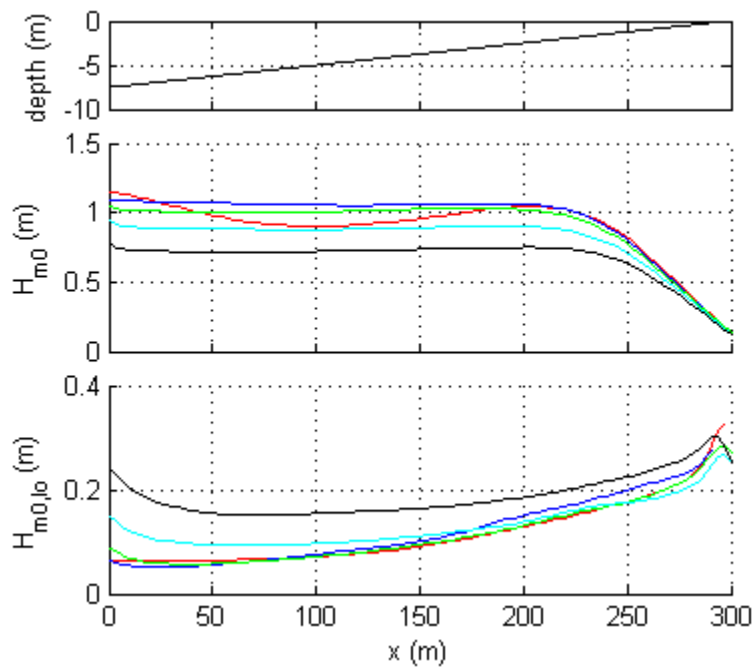


Figure D.4: Influence domain width on SWASH results for case 4, simulation D (directional spreading of  $40^\circ$ ). Domain width: 100m (red); 500m (blue); 1000m (green); 2000m (cyan); 4000m (black).

Table D-1: Domain width (m) for the 2D simulations corresponding to the simulation (A/B/C/D) for a varying directional spreading (case 4, 2<sup>nd</sup> row) and for a varying mean incident angle (case 5, 3<sup>rd</sup> row).

	A	B	C	D
4, $\sigma_\theta$	500	500	1000	1000
5, $\theta_0$	500	400	600	800

### Spin up

The influence of the spin-up time on the SWASH results is investigated by examining the results where the longest spin-up time is expected, which is the case with the greatest directional spreading (case 4, simulation D with a directional width of  $40^\circ$ ). The spin-up time is investigated by introducing a start-time from which point onwards the integral wave parameters are calculated. Results for a varying start time show that the spin-up time has a negligible influence on the short-wave height and IG-wave height (Figure D.5).

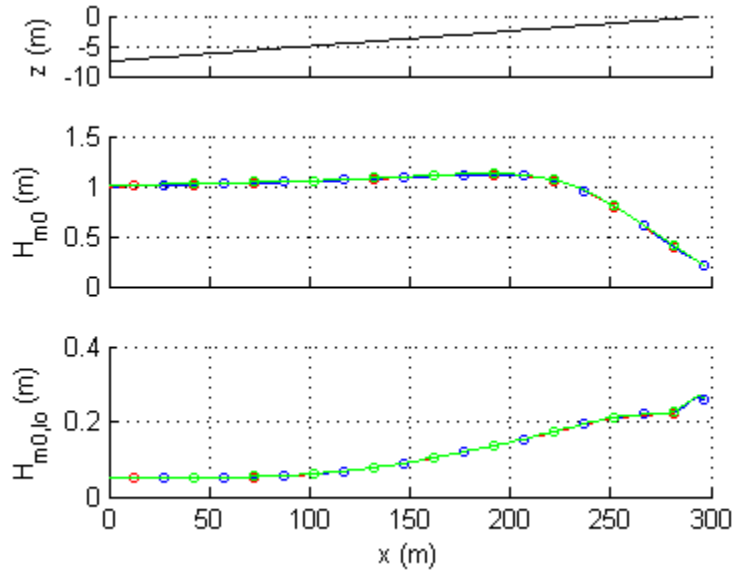


Figure D.5: Sensitivity analysis, influence of spin-up on the integral wave parameters. SWASH results for case 5 simulation D ( $\theta_0 = 40^\circ$ ). Start time: 0s (red); 120s (blue) 600s (green). Upper panel: Cross-shore transect of the bottom profile, middle panel: significant short-wave height and lower panel: significant IG-wave height.



### E. Flume case – Signal decomposition, additional information

Application of the collocated method and the array method to the SWASH results allows for a comparison of both techniques. The overall results of the incoming and outgoing waves compare well for both methods (Figure E.1). A difference between both methods is observed for the outgoing IG-wave height in region II, where the results of the array method are irregular. This irregular pattern is associated with noise due to the decomposition method and not due to noise in the IG surface elevations.

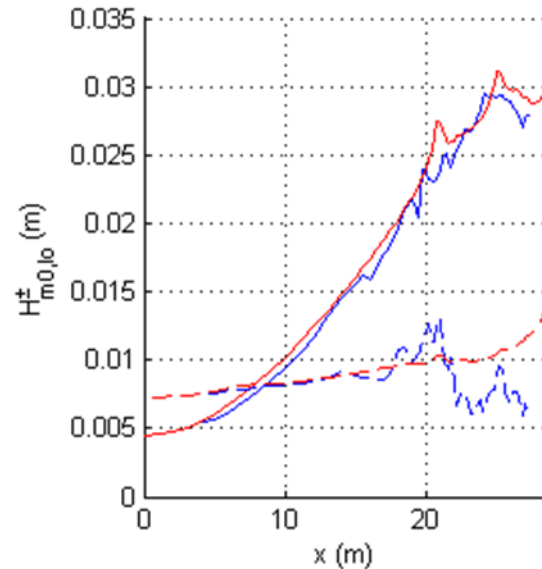


Figure E.1: Signal decomposition for SWASH, collocated method (red) and array method (blue). Solid line: significant incoming IG-wave height, dashed line: significant outgoing IG-wave height.

Applying the cross-correlation technique to the surface elevation signals corresponding to the incoming and reflected IG-wave gives additional insight in the performance of the collocated method. The results for the incoming IG-wave show a pattern associated with an incoming IG-wave whereas no sign of an outgoing IG-wave is identified (Figure E.2). For the outgoing IG-wave a pattern is observed associated with an outgoing IG-wave while no incoming IG-wave is identified. These results therefore strengthen the confidence in the collocated decomposition method.

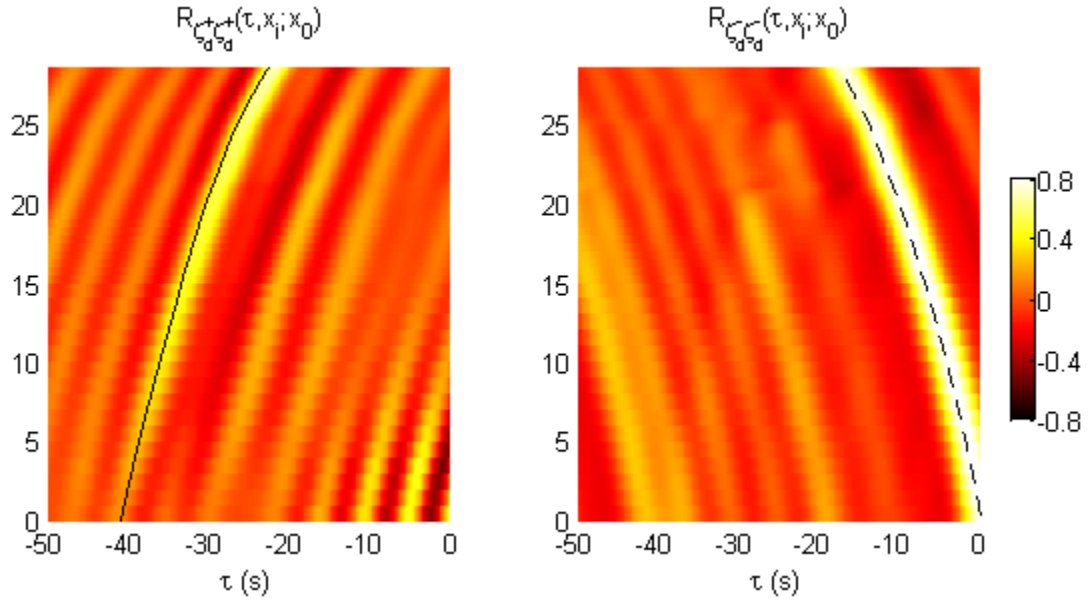


Figure E.2: Cross-correlation function of the detrended IG-surface elevation throughout the domain  $x_i$  and at the offshore boundary  $x_i=0$ . Left panel: Cross-correlation results for the incoming IG-surface elevation, right panel: Cross-correlation results for the reflected IG-surface elevation. The solid black line represents the time shift due to the group velocity according to the peak frequency and the dashed black line represents the time shift according to  $\sqrt{gh}$ .

## F. Field case – influence sample length

Pressure measurements with a sample length of 2h16min are translated into energy density spectra for a range of sample lengths. This gives insight in the influence of the sample length on the calculated energy density spectra.

The overall shape of the energy density spectra at the IG-frequencies remains similar for a decreasing sample length, only for the smallest sample length the shape becomes irregular and different compared to the results for the largest sample length. Similar to the energy densities, the integral wave parameters are not significantly changed by the sample length (Table F-1).

The results indicate that a sample length of 35min is sufficient for an estimation of the spectral densities at the IG-frequencies, the significant short-wave height and the significant IG-wave height.

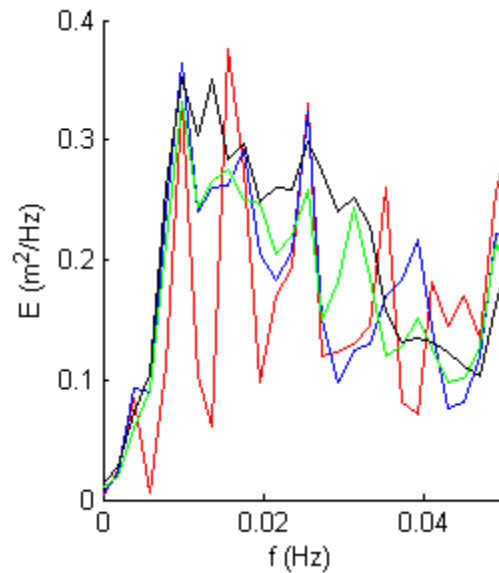


Figure F.1: Influence of the sample length on the energy density spectra at the IG-frequencies (right panel). The colours represent the results for a sample length of 170min (black), 60min (green), 35min (blue) and 17min (red).

Table F-1: Significant short-wave height and significant IG-wave height for the various sample lengths.

Sample length (min)	$H_{m0}$ (m)	$H_{m0,10}$ (m)
170	2.36	0.29
60	2.33	0.27
35	2.26	0.27
17	2.30	0.25